Neutrinos from STORed Muons: the nuSTORM Accelerator Facility

D. Adey,[1] S.K. Agarwalla,[2] C.M. Ankenbrandt,[3, *] R. Asfandiyarov,[4] J.J. Back,[5]
G. Barker,[5] E. Baussan,[6] R. Bayes,[7, †] S. Bhadra,[8] V. Blackmore,[9] A. Blondel,[4]
S.A. Bogacz,[10] C. Booth,[11] S.B. Boyd,[5] S.G. Bramsiepe,[7] A. Bravar,[4] S.J. Brice,[1]
A.D. Bross,[1] F. Cadoux,[4] H. Cease,[1] A. Cervera,[12] J. Cobb,[9] D. Colling,[13] P. Coloma,[14]
L. Coney,[15] A. Dobbs,[13] J. Dobson,[13] A. Donini,[12] P. Dornan,[13] M. Dracos,[6] F. Dufour,[4]
R. Edgecock,[16] M. Geelhoed,[1] M.A. Uchida,[13] T. Ghosh,[12] J.J. Gómez-Cadenas,[12]
A. de Gouvêa,[17] A. Haesler,[4] G. Hanson,[15] P.F. Harrison,[5] M. Hartz,[8, ‡] P. Hernández,[12]
J.A. Hernando Morata,[18] P. Hodgson,[11] P. Huber,[14] A. Izmaylov,[12] Y. Karadzhov,[4]
T. Kobilarcik,[1] J. Kopp,[19] L. Kormos,[20] A. Korzenev,[4] Y. Kuno,[21] A. Kurup,[13]
P. Kyberd,[22] J.B. Lagrange,[23] A. Laing,[12] A. Liu,[1] J.M. Link,[14] K. Long,[13] K. Mahn,[24]
C. Mariani,[14] C. Martin,[4] J. Martin,[25] N. McCauley,[26] K.T. McDonald,[27] O. Mena,[12]
S.R. Mishra,[28] N. Mokhov,[1] J. Morfín,[1] Y. Mori,[23] W. Murray,[16] D. Neuffer,[1]
R. Nichol,[29] E. Noah,[4] M.A. Palmer,[1] S. Parke,[1] S. Pascoli,[30] J. Pasternak,[13]
R. Plunkett,[1] M. Popovic,[1] P. Ratoff,[20] M. Ravonel,[4] M. Rayner,[4] S. Ricciardi,[16]
C. Rogers,[16] P. Rubinov,[1] E. Santos,[13] A. Sato,[21] T. Sen,[1] E. Scantamburlo,[4]
J.K. Sedgbeer,[13] D.R. Smith,[22] P.J. Smith,[11] J.T. Sobczyk,[31] L. Søby,[32] F.J.P. Soler,[7]
M. Sorel,[12] P. Snopok,[33, §] P. Stamoulis,[12] L. Stanco,[34] S. Striganov,[1] H.A. Tanaka,[35]
I.J. Taylor,[5] C. Touramanis,[26] C. D. Tunnell,[9, ¶] Y. Uchida,[13] N. Vassilopoulos,[6]
M.O. Wascko,[13] A. Weber,[9] M.J. Wilking,[24] E. Wildner,[32] and W. Winter[36]
(The nuSTORM Collaboration)

[1]*Fermi National Accelerator Laboratory,
Box 500, Batavia, IL 60510-5011, USA*

[2]*Institute of Physics, Sachivalaya Marg,
Sainik School Post, Bhubaneswar 751005, Orissa, India*

[3]*Muons Inc., 552 N. Batavia Avenue, Batavia, IL 60510, USA*

[4]*University de Geneve, 24, Quai Ernest-Ansermet, 1211 Geneva 4, Switzerland*

[5]*Department of Physics, University of Warwick, Coventry, CV4 7AL, UK*

[6]*IPHC, Université de Strasbourg, CNRS/IN2P3, F-67037 Strasbourg, France*

[7]*School of Physics and Astronomy, Kelvin Building,
University of Glasgow, Glasgow G12 8QQ, Scotland, UK*

[8]*Department of Physics and Astronomy, York University,
4700 Keele Street, Toronto, Ontario, M3J 1P3, Canada*

[9]*Oxford University, Subdepartment of Particle Physics, Oxford, UK*

[10] *Thomas Jefferson National Accelerator Facility, Newport News, VA, USA*

[11] *University of Sheffield, Dept. of Physics and Astronomy, Hicks Bldg., Sheffield S3 7RH, UK*

[12] *Instituto de Física Corpuscular (IFIC),*
Centro Mixto CSIC-UVEG, Edificio Institutos Investigación,
Paterna, Apartado 22085, 46071 Valencia, Spain

[13] *Physics Department, Blackett Laboratory,*
Imperial College London, Exhibition Road, London, SW7 2AZ, UK

[14] *Center for Neutrino Physics, Virginia Polytechnic*
Institute and State University. Blacksburg, VA 24061-0435

[15] *University of California, Riverside, CA, USA*

[16] *STFC Rutherford Appleton Laboratory,*
Chilton, Didcot, Oxfordshire, OX11 0QX, UK

[17] *Northwestern University, Evanston, IL, USA*

[18] *Universidade de Santiago de Compostela (USC),*
Departamento de Fisica de Particulas,
E-15706 Santiago de Compostela, Spain

[19] *Max-Planck-Institut für Kernphysik,*
PO Box 103980, 69029 Heidelberg, Germany

[20] *Physics Department, Lancaster University, Lancaster, LA1 4YB, UK*

[21] *Osaka University, Osaka, Japan*

[22] *Centre for Sensors and Instrumentation, School of Engineering and Design,*
Brunel University, Uxbridge, Middlesex, UB8 3PH, UK

[23] *Kyoto University, Kyoto, Japan*

[24] *TRIUMF, 4004 Wesbrook Mall, Vancouver, B.C., V6T 2A3, Canada*

[25] *Department of Physics, University of Toronto,*
60 St. George Street, Toronto, Ontario, M5S 1A7, Canada

[26] *Department of Physics, Oliver Lodge Laboratory,*
University of Liverpool, Liverpool, L69 7ZE, UK

[27] *Princeton University, Princeton, NJ, 08544, USA*

[28] *Department of Physics and Astronomy,*
University of South Carolina, Columbia SC 29208, USA

[29] *Department of Physics and Astronomy,*
University College London, Gower Street, London, WC1E 6BT, UK

^{30}*Institute for Particle Physics Phenomenology,*
Department of Physics, Durham University, Durham, DH1 3LE, UK

^{31}*Institute of Theoretical Physics, University of Wroclaw,*
pl. M. Borna 9,50-204, Wroclaw, Poland

^{32}*CERN,CH-1211, Geneva 23, Switzerland*

^{33}*Illinois Institute of Technology, Chicago, IL 60616*

^{34}*INFN, Sezione di Padova, 35131 Padova, Italy*

^{35}*Department of Physics and Astronomy,*
Hennings Building, The University of British Columbia,
6224 Agricultural Road, Vancouver, B.C., V6T 1Z1, Canada

^{36}*Fakultät für Physik und Astronomie,*
Universität Würzburg Am Hubland, 97074 Würzburg, Germany

(Dated: March 21, 2014)

The nuSTORM facility (Neutrinos from STORed Muons) has been designed to deliver beams of $\overset{\text{\tiny(}-\text{\tiny)}}{\nu}_e$ and $\overset{\text{\tiny(}-\text{\tiny)}}{\nu}_\mu$ from the decay of a stored $\mu^\pm$ beam with a central momentum of $3.8\,\text{GeV/c}$ and a momentum acceptance of 10%. The facility is unique in that it will:

- Allow searches for eV-scale sterile neutrinos at better than 10σ sensitivity to be carried out;

- Serve future long- and short-baseline neutrino-oscillation programs by providing definitive measurements of $\overset{\text{\tiny(}-\text{\tiny)}}{\nu}_e N$ and $\overset{\text{\tiny(}-\text{\tiny)}}{\nu}_\mu N$ scattering cross sections with percent-level precision; and

- Constitute the crucial first step in the development of muon accelerators as a powerful new technique for particle physics.

In this paper, we will report on the capabilities of the nuSTORM facility to deliver the stated physics objectives and we will specify the main features of the design of the accelerator. It will be shown that no new technology is required to deliver an accelrator facility that may resolve the eV-scale sterile neutrino hints, may provide a beam with percent-level flux uncertainties for cross-section measurements and may be the first step towards a Neutrino Factory and a Muon Collider.

---

* Also at Fermilab, P.O. Box 500, Batavia, IL 60510-5011, USA

† Corresponding author: Ryan.Bayes@glasgow.ac.uk

‡ Also at Department of Physics, University of Toronto, 60 St. George Street, Toronto, Ontario, M5S 1A7, Canada

§ Also at Fermi National Accelerator Laboratory, Box 500, Batavia, IL 60510-5011, USA

¶ Now at NikHEF, Amsterdam, The Netherlands

I. OVERVIEW

The idea of using a muon storage ring to produce a neutrino beam for experiments was first discussed by Koshkarev [1] in 1974. A detailed description of a muon storage ring for neutrino oscillation experiments was first produced by Neuffer [2] in 1980. In his paper, Neuffer studied muon decay rings with E_μ of 8, 4.5 and 1.5 GeV. With his 4.5 GeV ring design, he achieved a figure of merit of $\simeq 6 \times 10^9$ useful neutrinos per 3×10^{13} protons on target. The facility we describe in ths paper (nuSTORM) is similar to the facility proposed in 1980 and utilizes a 3.8 GeV/c muon storage ring with 10% momentum acceptance to study eV-scale oscillation physics, ν_e and ν_μ interaction physics and to develop technology for future accelerator projects. In particular, the facility can:

- Serve a first-rate neutrino oscillation physics program encompassing sensitive searches for sterile neutrinos in both appearance and disappearance modes;

- Provide detailed and precise studies of electron- and muon-neutrino-nucleus scattering over the energy appropriate for future long- and short-baseline neutrino oscillation programs; and

- Provide the technology test-bed required to carry-out the R&D critical for the implementation of the next step in a muon-accelerator based particle-physics program.

A number of results have been reported that can be interpreted as hints for oscillations involving sterile neutrinos [3–13] (for a recent review see [**?**]). Taken together, these hints warrant a systematically different and definitive search for sterile neutrinos. nuSTORM is capable of making the measurements required to confirm or refute the evidence for sterile neutrinos using a technique that is both qualitatively and quantitatively new [14, 15]. The nuSTORM facility has been designed to deliver beams of ν_e ($\bar{\nu}_e$) and $\bar{\nu}_\mu$ (ν_μ). A detector located at a distance $\sim 2\,000\,\mathrm{m}$ from the end of one of the straight sections will be able to make sensitive searches for the existence of sterile neutrinos. If no appearance ($\bar{\nu}_\mu \to \bar{\nu}_e$) signal is observed, the LSND allowed region can be ruled out at the $\sim 10\sigma$ level [16]. Instrumenting the nuSTORM neutrino beam with a near detector at a distance of $\sim 20\,\mathrm{m}$ makes it possible to search for sterile neutrinos in the disappearance $\nu_e \to \nu_X$ and $\nu_\mu \to \nu_X$ channels. In the disappearance search, the absence of a signal would permit the presently

allowed region to be excluded at the 99% confidence level [16]. For a general discussion of optimization of disappearance searches at short baseline, see [17].

The race to discover CP-invariance violation in the lepton sector and to determine the neutrino mass-hierarchy has begun with the recent discovery that θ_{13} is non-zero [18–22]. The measured value of θ_{13} is large ($\sin^2 2\theta_{13} \sim 0.1$), so measurements of oscillation probabilities with uncertainties at the percent level are required. For future long-baseline experiments to reach their ultimate precision requires that the $\overset{\scriptscriptstyle(-)}{\nu}_e N$ and the $\overset{\scriptscriptstyle(-)}{\nu}_\mu N$ cross sections are known precisely for neutrino energies (E_ν) in the range $0.5 < E_\nu < 3\,\mathrm{GeV}$. nuSTORM is therefore unique as it makes it possible to measure the $\overset{\scriptscriptstyle(-)}{\nu}_e N$ and the $\overset{\scriptscriptstyle(-)}{\nu}_\mu N$ cross sections with a precision $\simeq 1\%$ over the required neutrino-energy range. At nuSTORM, the flavor composition of the beam and the neutrino-energy spectrum are both precisely known. In addition, the storage-ring instrumentation combined with measurements at a near detector will allow the neutrino flux to be determined to the required precision of 1% or better. In effect, the unique ν beam available at the nuSTORM facility has the potential to be transformational in our approach to ν interaction physics, offering a "ν light source" to physicists from a number of disciplines.

Finally, nuSTORM's unique capabilities offer the opportunity to provide muon beams for future investigations into muon ionization cooling, while running the neutrino program simultaneously. Muon cooling is the key enabling technology needed for future ultra-high intensity muon accelerator facilities. Its demonstration would be one of the major steps towards the realization of a multi-TeV Muon Collider.

By providing an ideal technology test-bed, the nuSTORM facility will play a pivotal role in the development of accelerator systems, instrumentation techniques, and neutrino detectors. It is capable of providing a high-intensity, high-emittance, low-energy muon beam for studies of ionization cooling and can support the development of the high-resolution, totally-active, magnetized neutrino detectors. The development of the nuSTORM ring, together with the instrumentation required for the sterile-neutrino-search and the νN-scattering programs, will allow the next step in the development of muon accelerators for particle physics to be defined. nuSTORM has the potential to establish a new technique for particle physics that can be developed to deliver the high-energy ν_e ($\bar{\nu}_e$) beams required to elucidate the physics of flavor at the Neutrino Factory and to provide the enabling technologies for a multi-TeV

$\mu^+\mu^-$ collider.

nuSTORM itself represents the simplest implementation of the Neutrino Factory concept [23]. In our case, 120 GeV/c protons are used to produce pions off a conventional solid target. The pions are collected with a magnetic horn and quadrupole magnets and are then transported to, and injected into, a storage ring. The pions that decay in the first straight of the ring can yield a muons that are captured in the ring. The circulating muons then subsequently decay into electrons and neutrinos. We are using a storage ring design that is optimized for 3.8 GeV/c muon momentum. This momentum was selected to maximize the physics reach for both ν oscillation and the cross section physics. See Fig. 1 for a schematic of the facility.
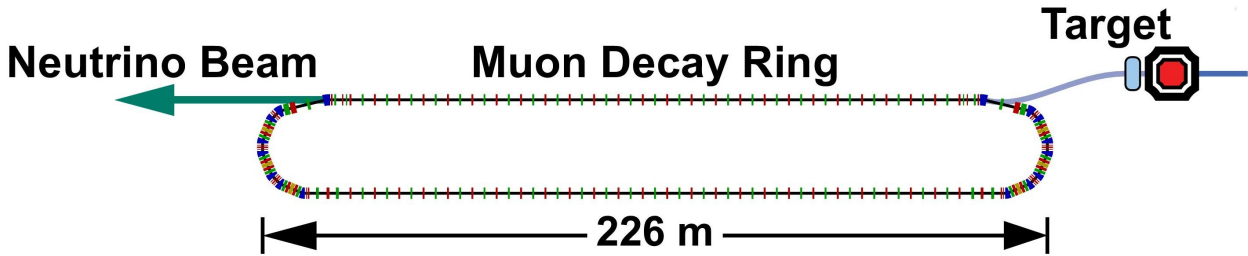
Figure 1. Schematic of the facility

Muon decay yields a neutrino beam of precisely known flavor content and energy. For example for positive muons: $\mu^+ \rightarrow e^+ + \bar{\nu}_\mu + \nu_e$. In addition, if the circulating muon flux in the ring is measured accurately (with beam-current transformers, for example), then the neutrino beam flux is also accurately known. Near and far detectors are placed along the line of one of the straight sections of the racetrack decay ring. The near detector can be placed as close as 20 meters from the end of the straight. A near detector for disappearance measurements will be identical to the far detector, but only about one tenth the fiducial mass. Additional purpose-specific near detectors can also be located in the near hall and will measure neutrino-nucleon cross sections and can provide the first precision measurements of ν_e and $\bar{\nu}_e$ cross sections. A far detector at $\simeq 2000$ m would study neutrino oscillation physics and would be capable of performing searches in both appearance and disappearance channels. The experiment will take advantage of the "golden channel" of oscillation appearance $\nu_e \rightarrow \nu_\mu$, where the resulting final state has a muon of the wrong-sign

from interactions of the $\bar{\nu}_\mu$ in the beam. In the case of μ^+ stored in the ring, this would mean the observation of an event with a μ^-. This detector would need to be magnetized for the wrong-sign muon appearance channel, as is the case for the current baseline Neutrino Factory detector [24]. A number of possibilities for the far detector exist. However, a magnetized iron detector similar to that used in MINOS is seen to be the most straightforward and cost-effective approach. For the purposes of the nuSTORM oscillation physics, a detector inspired by MINOS, but with thinner plates and much larger excitation current (larger B field) is assumed.

II. FACILITY

The basic concept for the facility was presented in Fig. 1. A high-intensity proton source places beam on a target, producing a large spectrum of secondary pions. Forward pions are focused by a horn into a capture and transport channel. Pion decays within the first straight of the decay ring can yield a muon that is stored in the ring. Muon decay within the straight sections will produce ν beams of known flux and flavor via: $\mu^+ \to e^+ + \bar{\nu}_\mu + \nu_e$ or $\mu^- \to e^- + \nu_\mu + \bar{\nu}_e$. For the implementation which is described here, we choose a 3.8 GeV/c storage ring to obtain the desired spectrum of $\simeq 2$ GeV neutrinos (see Fig. **??**). This means that we must capture pions at a momentum of approximately 5 GeV/c.

A. Primary proton beam

This section describes the reference design for the nuSTORM primary (proton) beamline. This system will extract protons from the Fermilab MI (MI) synchrotron, using a single-turn single-batch extraction method and then transport them to the target in the nuSTORM target hall. The nominal range of operation will be for protons from 60 to 120 GeV/c.

The principal components of the primary beamline include the standard magnets in the MI-40 abort line to capture protons in the synchrotron and redirect them to the nuSTORM beamline. This beamline is a series of dipoles and quadrupole magnets to transport the protons to the target. All of the nuSTORM primary-beam technical systems are being designed to support sustained, robust and precision beam operation.

In 1994, the NuMI Project Definition Report originally designed the extraction line from the MI-40 area. The MI absorber was built with the transport beam pipe installed at an estimated elevation of 714 feet. The nuSTORM facility will extract protons from the MI through this channel and continue through two enclosures towards the nuSTORM target hall [25]. In Fig. 2, this channel is indicated by the shaded-in square offset from the center of the MI Absorber. The nuSTORM primary beam is extracted using single-turn, or "fast" extraction, in which a portion of the protons accelerated in the MI synchrotron ring, will be diverted to the nuSTORM beamline within one revolution after each acceleration cycle. The train of bunches dedicated for the nuSTORM target hall extends one seventh of the MI circumference or for one "Booster Batch." The remaining bunches are dedicated to
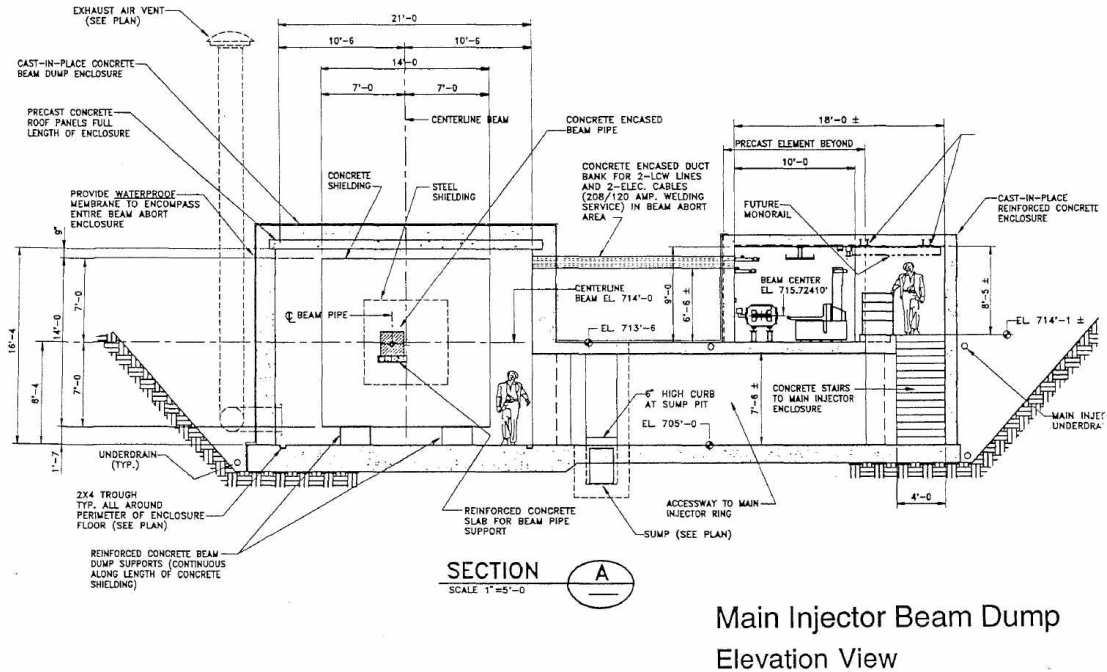
8

Figure 2. MI absorber room cross section.

additional operational beamlines running concurrently, i.e. NuMI, NoVA, or LBNE [26, 27]. After extraction, the beam is controlled by a series of dipoles (bending) and quadrupole (focusing) magnets.

The nuSTORM primary-beamline is designed to direct the beam towards the nuSTORM target hall and collection channel, with a spot size appropriate for maximizing pion production (see Section II C). nuSTORM will implement a point to point focusing design in two sections. This is allowed due to the relatively short distance between THE MI and the nuSTORM target hall (600') and also because a large beam spot is required for the MI absorber line (upstream beamline common to MI abort line and nuSTORM). The first section focuses the proton beam after the MI absorber line. The second and final focus of the beam will be used for controlling the beam spot size on the target.

1. Extraction line

In order to achieve this focused beam, the MI absorber line will be modified with respect to placement of existing quadrupole magnets and replacement of their HV cables from the MI quad focusing buss onto separate individual power supplies. All absorber line quadrupoles, Q001 through Q003, will need independent power supplies. Q002 and Q003 will need to be

moved upstream of their current locations by 23 and 30 feet respectfully. This relocation will provide adequate space for nuSTORM's extraction switch magnet and allow for proper optics in the remaining beamline. The two large bending magnets will remain in their current location, and continue to operate on the MI bend buss.

Once MI beam has achieved its flattop energy, three new kicker magnets in the MI-40 area apply a horizontal kick to the beam to the outside of the ring. This beam passes through a set of quadrupoles, Q401 and Q402, to continue the horizontal trajectory at elevation 715 feet, 9 inches. Then a series of three specialized magnets called Lambertsons [28], L001 L002 and L003, vertically extract the beam from the MI. These extraction Lambertsons are unique in that this set bend the beam downward for extraction, while in other Lambertson areas, such as MI-52 and MI-60, they bend the beam upward.

The Lambertsons sit in the path of the beam both when beam circulates and when it is being extracted, so they must accommodate both paths. The circulating beam passes through a field-free region in the magnet, and the extracted beam passes through the region of magnetic field and is bent downward from the circulating MI trajectory by 18.24 milli-radians. Fig. 3 shows a cross section of the MI Lambertson. Each Lambertson in the line
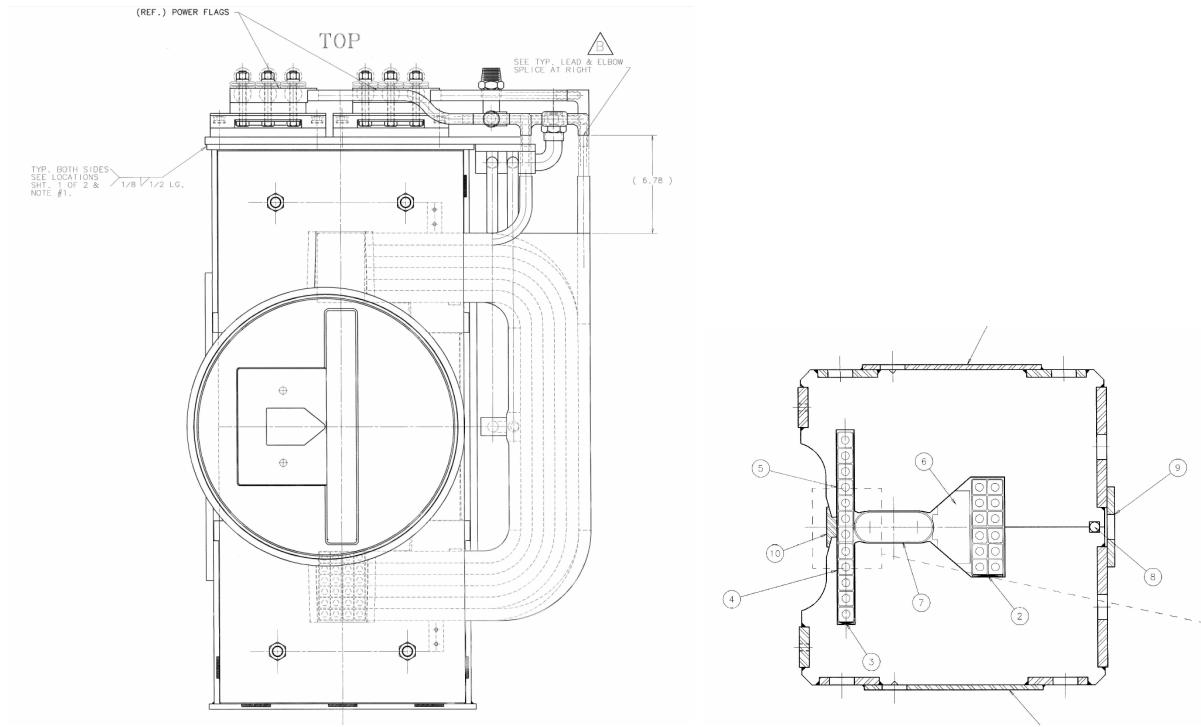
Figure 3. MI Lambertson (left) and C magnet drawings (right).

bends the beam, such that after passing through the string of Lambertsons the extracted

beam is sufficiently separated from the MI orbit to pass through the first bending magnet external to the MI, a C-magnet [29]. The C-magnet clears the MI beam tube downstream of the third Lambertson and provides an additional downward bend, 9.34 milliradians, enough so that the extracted beam can pass below the outside of the next quadrupole in the MI lattice. This also accommodates clearance for the first quadrupole, Q001, in the absorber line. Fig. 3 also shows a cross section of the MI C-magnet.

Once the nuSTORM primary beam is extracted from the MI, it shares the beam line components with the MI aborted beam. With its trajectory, the nuSTORM primary beam will be directed and focused exactly like the MI aborted beam by a series of three quadrupoles, two dipoles and several trim magnets. However, once past the last quadrupole, Q003, the beam will be bent towards the transport beam pipe in the MI absorber using a pulsed EDB (extended dipole bender) dipole named NSHV1 [30]. This horizontal pulsed magnet is rolled by 0.37 radians clockwise to necessitate the horizontal and vertical differences between the MI absorber and the transport beam pipe aperture, as shown in Fig. 2. This results in the beam being bent 4.97 milliradians horizontally away from the MI ring and 1.93 milliradians vertically downward.

Between the MI enclosure and the MI absorber room is a distance of 88 feet. This stretch of beamline is transitioned into an 24 inch wide "bermpipe" commonly used at Fermilab. This vacuum isolated stretch of bermpipe [31] will contain three beamlines, two of them converging towards the MI Absorber, while the nuSTORM trajectory is towards the Transport Beam Pipe. Fig. 4 shows this berm pipe relative to the MI enclosure and absorber room.

2.   Beam line

From the back end of the MI Absorber Room, the nuSTORM beamline continues into new construction enclosures. The first section of optics is to match the MI Abort line optics to the final focusing optics of the nuSTORM beamline. This is achieved by using only two 3Q120 quadrupole magnets, NS1Q1 and NS1Q2, at the beginning of the first enclosure NS1 [32]. Once the beam has passed the first quadrupoles in the NS1 enclosure, the beam is bent upwards by NS1V1 to correct for the downward trajectory created naturally by the MI Absorber line and the NSHV1. Here the beam line is at its lowest point 713 feet, 3 inches.
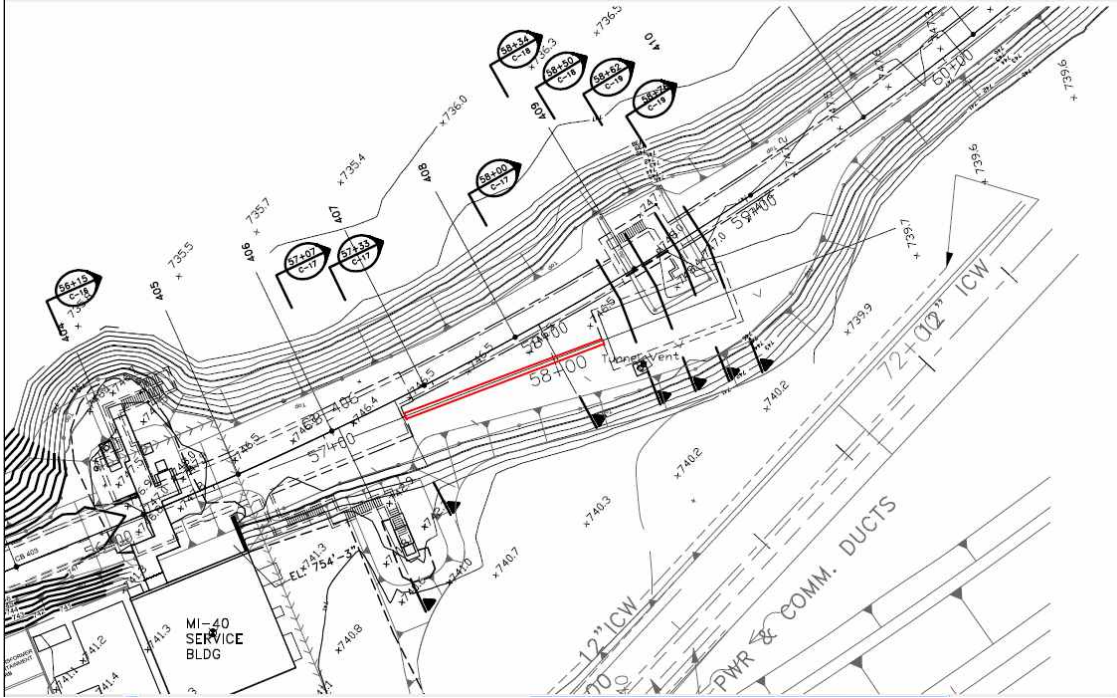
Figure 4. MI absorber berm pipe.

After the beam has had the necessary drift space to be focussed by NS1Q1 and NS1Q2, and be placed on the correct vertical trajectory by NS1V1, the first series of horizontal dipoles, NS1H1, bends the beam 0.0934 radians. This horizontal string of magnets is comprised of four B2 magnets [33] with a 1.54 Tesla field. After this string of dipoles the beam is then transported to the next enclosure, NS2.

In NS2, the beam is bent with another series of four B2 dipoles, NS2H1. This string bends the beam an additional 0.0934 radians, with a bend field of 1.54 T. After the last bend string, a single quadrupole magnet NS2Q1 focuses the beam vertically. This allows the beam to be focused after the bending by the NS2 horizontal magnet string. After the last bend, the beam is focused onto the nuSTORM target via NS2Q1. This quadrupole will be able to focus the beam on target to maximize pion production and efficiency. The beam half widths and component apertures are shown in Fig. 5 and Fig. 6. They include the FODO lattice of the MI through the absorber line and through the nuSTORM primary beamline. The nuSTORM primary beamline starts at station 481 ft. This beamline is also specifically planned so that it has very little impact on current operational surroundings. The nuSTORM beamline optics share three quadrupoles with the MI absorber line, and three dedicated quadrupoles in the primary beamline. The optics and trajectory of this

12
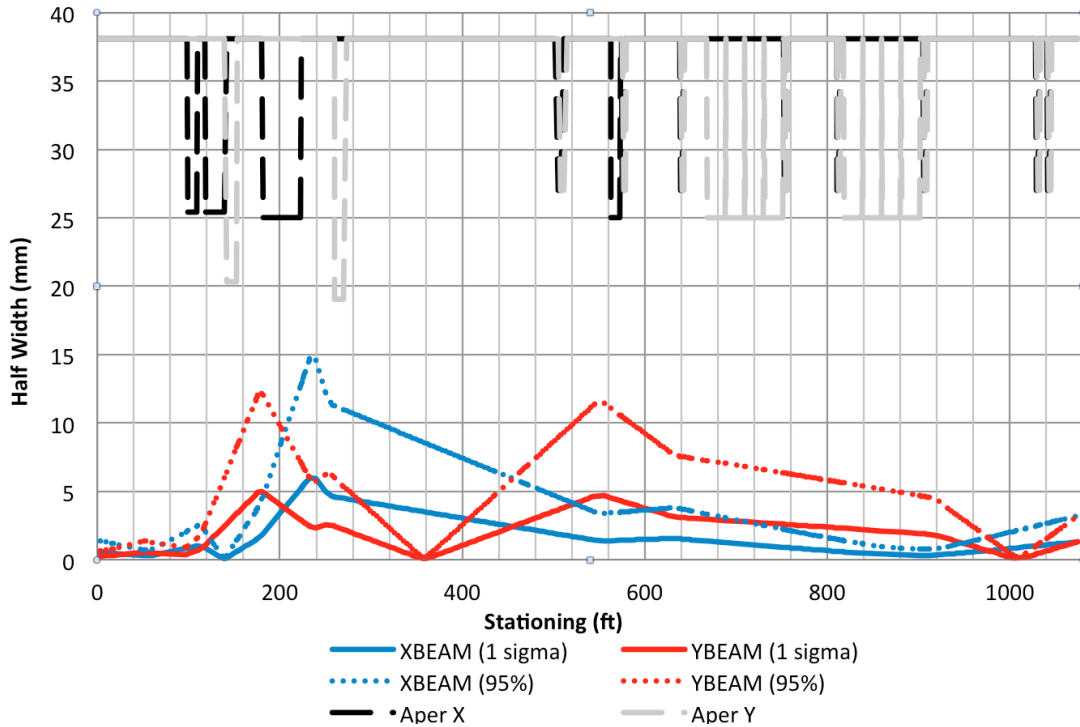
Figure 5. nuSTORM beamline half width sizes and apertures for 120 Gev/c protons.

beamline have been designed to handle different momentum protons to be operational with concurrently running experiments utilizing the MI in the future. Fig. 5 is designed for 120 GeV/c protons, however, Fig. 6 shows the beam line is capable of focusing the 60 GeV/c protons for future experiments. Table I contains the data for the nuSTORM quadrupoles for 120 GeV/c protons.   The nuSTORM beamline contains 18 correctors or 9 pairs of horizontal and vertical trims, before and after every large angle change mentioned above. Four of these correctors are placed just prior to the nuSTORM target hall for the operational ability to change the position and angle of the beam interacting with the target. This set of correctors will be useful for target scans and alignment. These correctors can correct a 0.25 mm transverse mis-alignment offset for all the major bending dipoles. For roll tolerances, the maximum acceptable error is 0.5 milliradians [34].

As mentioned above, the nuSTORM primary beamline focusing and bending elements are split between two different enclosures. These enclosures are split by a jacked pipe of 59 feet in length. Running through this jacked pipe, are individual pipes that contain the beam line and other utility supply and return lines. The primary beamline enclosure layout

13

NuStorm Primary Beamline 60 Gev/c
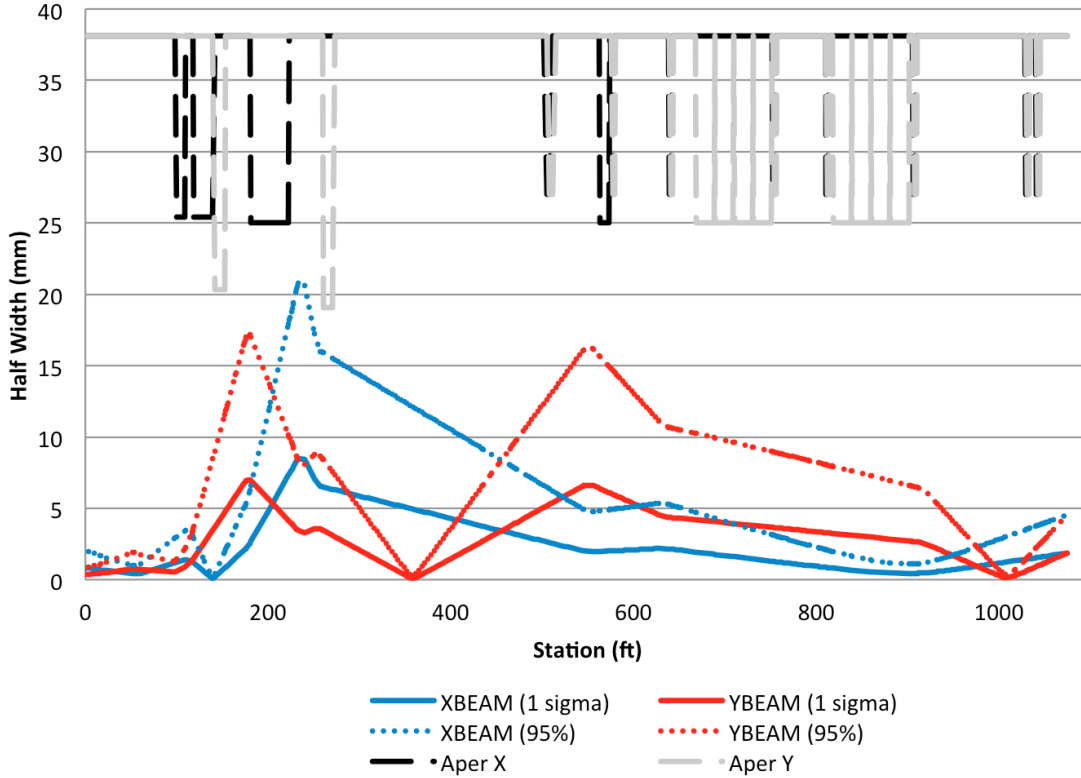
Figure 6. nuSTORM beamline half width sizes and apertures for 60 Gev/c protons.

Table I. Magnet names types and settings for 120 Gev/c protons.

Dipoles	Type	Current (Amps)	Notes
NSHV1	EDB	796.4	Rolled 0.37 radians
NS1V1	EDB	664.7	Critical Device #1
NS1H1 (4)	B2	3833.1	Critical Device #2
NS2H1 (4)	B2	3833.1	
Quadrupoles	Type	Current (Amps)	Notes
Q001	IQA	1883.2	Vertical Focusing
Q002	IQB	1423.9	Horizontal Focusing
Q003	IQB	853.0	Vertical Focusing
NS1Q1	3Q120	22.3	Vertical Focusing
NS1Q2	3Q120	11.9	Horizontal Focusing
NS2Q1	3Q120	19.5	Vertical Focusing

is shown in Fig. 7 along with the proposed target hall, Pion Decay Channel and Muon Decay Ring. nuSTORM's primary beamline will use two critical devices, as stipulated in
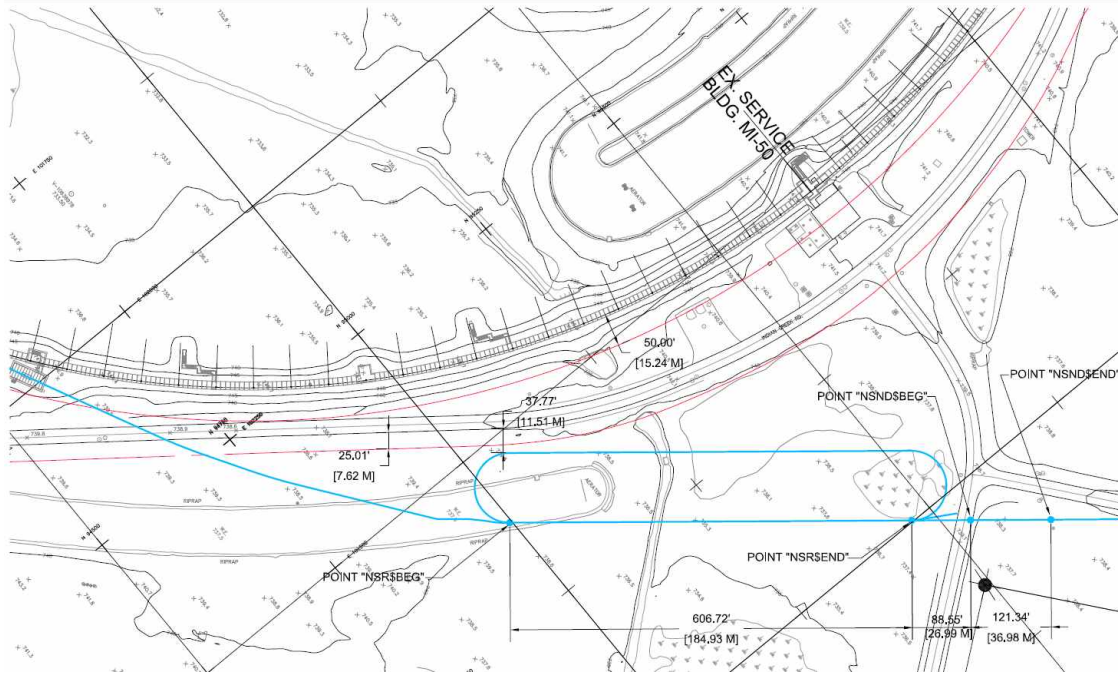
Figure 7. Enclosure layout of nuSTORM primary beamline.

the Fermilab Radiological Control Manual [35] (FRCM). The first critical device, NSHV1, is located inside the MI-40 area as described above. This switch magnet must be powered in order to allow beam to the nuSTORM target. The second critical device will be NS1H1, as described above.

nuSTORM's primary beamline will also include instrumentation packages containing Loss Monitors, Toroids, Multiwires, and Beam Position Monitors (BPMs). In this current design the beamline contains three toroids, ten Multiwires, and twelve BPMs. Loss monitors will be placed on magnets with tighter aperture constraints. Each major bending string, NS1V1, NS1H1, and NS2H1 will have loss monitors mounted on the first magnet.

Of the three toroids, the first will be located inside the MI enclosure just prior to the berm pipe. This will be able to report an input for transfer efficiency to the nuSTORM target hall. The second toroid is positioned just after the NS1H1 magnet string in the NS1 enclosure. The last toroid will be positioned in enclosure NS2 just prior to the target hall. This will provide a comparison for transfer efficiency and protons on target measurements.

Of the ten Multiwires, enclosure NS1 has four and enclosure NS2 contains the remaining six. In each Multiwire, the wire spacing is assembled with 1 mm pitch, a common spacing at Fermilab, and each plane will contain forty wires. Each BPM unit contains horizontal

and vertical plates to provide horizontal and vertical positions, saving on longitudinal space in the beamline. nuSTORM will adopt the LBNE style button BPMs. In enclosure NS1, five BPMs will be installed and the NS2 enclosure will have six BPMs.

nuSTORM's two large bending strings of NS1H1 and NS2H1 have the same operating current and bend field. For power supplies to be used by this line, it is cost efficient to use one power supply to power both the first and the second string of B2 magnets. Other magnets such as the correctors, quadrupoles, and the first critical device NSHV1, will need to use independent power supplies .

B.   Target Station

1.   Target station overview and conceptual layout

The nuSTORM target station conceptual layout addresses the requirement of providing a reliable pion production facility while providing a platform for component maintenance and replacement. Due to the severe service environment encountered in target halls, it is expected that the beamline elements will require replacement on the order of every few years.

The general operation of the target station utilizes a primary proton beam extracted from the MI and transported to interact with a target to produce pions (along with other short-lived hadrons) which are subsequently focused toward a set of capture quadrupoles by a single magnetic focusing horn. The design parameters of beam spot size, target material and interaction length, and focusing horn current and geometry are considerations for providing reliable and sufficient pion production to support the experimental requirements. The following parameters for the proton beam on target are specified for the baseline in Table II. Several considerations must be adequately understood and addressed to ensure safe and reliable operation of the target station. The target station is one area where nuSTORM can draw heavily on the successful operation and experience gained in NuMI target hall operations. The nuSTORM target station baseline conceptual layout will employ a very similar design approach to that used in the NuMI target hall complex. The following key elements address the primary requirements for safe and reliable target station operation:

- Provide adequate shielding to safely accommodate a maximum beam power of 400kW.

Table II. Proton beam parameters

Energy	120 GeV
Protons per pulse	8×10^{12}
Pulse width	1.6 μs
Beam σ	1.1 mm
Cycle time	1.33 sec.

- Utilize economical shielding and target pile design methodology to minimize cost impact.

- Provide for the installation and operation of the following active beamline components:

  1. Production target

  2. Focusing horn, electrical stripline bus, and pulsed power supply

  3. Pair of capture quadrupole magnets and related power supplies and utilities

  4. Water-cooled collimators for quadrupole secondary beam spray protection

- Provide target pile shield with air cooling while considering humidity control to minimize component corrosion and provide the ability for safe and effective tritium management.

- Provide a target, horn, and capture quadrupole-positioning module support platform including shielding, hardware support provisions, remote hot handling capability with rigid, stable alignment capability.

- Provide for hot handling operations such as failed component replacement and cooldown storage for highly radioactivated components.

- Provide the infrastructure layout for constructing and operating the facility including radioactive water cooling (RAW) systems, component power supplies, air handling systems, adequate floor space for placement of shielding blocks during maintenance periods, and a component handling interface including remote pick functionality, cameras to facilitate hot handling, and a suitable overhead crane for material handling.

Many of the above elements will be addressed by using NuMI-style components and general target station layout as the design costs and operational characteristics are well understood

17

for NuMI. In addition, manpower is a significant cost driver for new projects and utilizing or slightly modifying existing design concepts minimizes cost impact.

The general target chase (i.e., beam space) shielding requirements will be met by utilizing a shield pile layout nearly identical to that of NuMI for 400kW operation. The nuSTORM target station shielding specifies 4 feet of steel surrounded by 3 feet of concrete, with vertical shielding requirements for sky-shine requiring 9 feet of steel with 6 in of borated polyethylene for prompt neutron shielding. Fig. 8 shows a cross-section of the target pile just downstream of the horn position. Several key elements appear in Fig. 8, including the Duratek steel (now
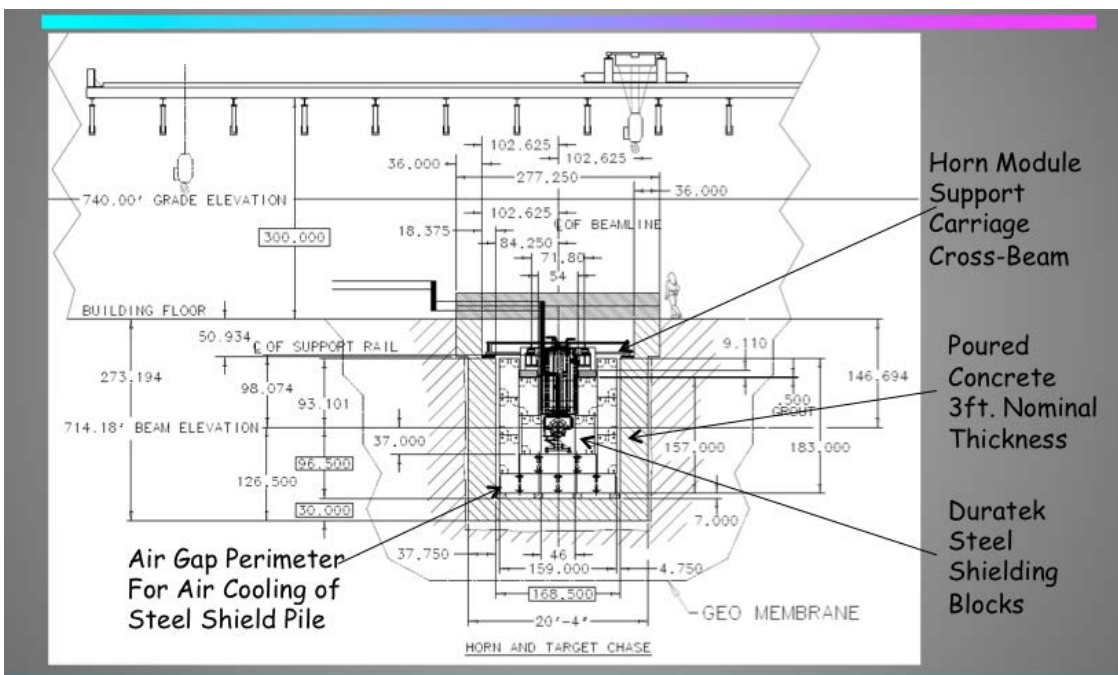
Figure 8. nuSTORM target pile and beamline chase cross-section downstream of horn looking in beam-upstream direction.

Energy Solutions) shielding block stack around the chase perimeter. These shielding blocks measure 26x52x52 in. with a corresponding weight of 10 tons each. The current nuSTORM conceptual layout requires approximately 140 Duratek blocks. As a cost benchmark, NuMI purchased a quantity of 500 Duratek blocks at a price of $226 per block (1.13 cents per pound). This underscores the benefit of using Duratek blocks, as they represent a significant source of very inexpensive steel.

Fig. 8 also depicts the horn-positioning module supported by a rigid I-beam carriage structure that is supported on an isothermal surface for accurate alignment during beam operation. Fig. 9 of this shielding configuration, as seen during NuMI construction, high-

lights additional detail. It is envisioned that this component mounting scheme and shield
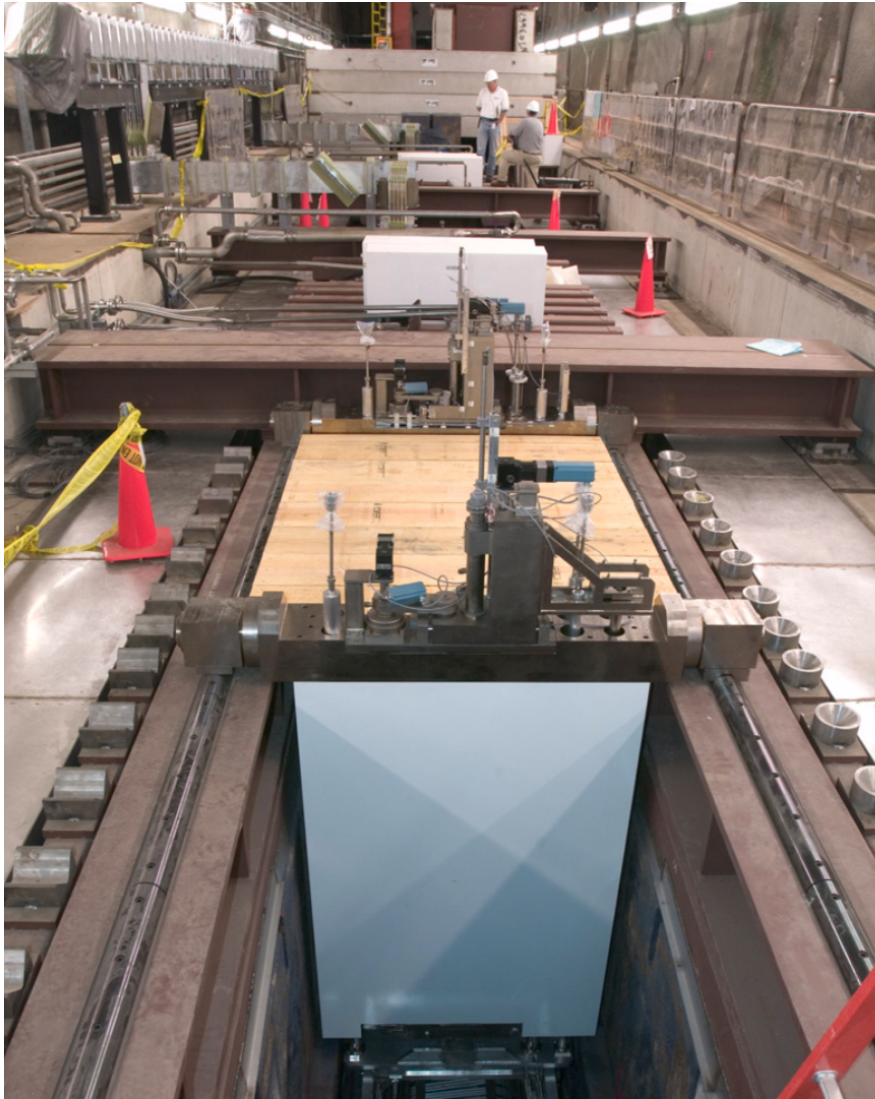
Figure 9. NuMI target pile chase, target module, and carriage I-beam support structure depicting target module installed in Duratek- lined beamline chase (view is upstream of target module looking downstream).

pile arrangement will be used for the target, horn, and capture quadrupoles.

Hot component handling and failed component replacement is addressed in the inherent design of the NuMI-style module that provides for remote handling capability. Component replacement is addressed by the use of a NuMI-style workcell that has a rail landing area identical to the beamline chase and allows for remote placement of the module into the workcell, after which a remotely operated door is closed and shielding hatch covers placed over the top-center of the module space to allow personnel access to the module top for remote disconnects and component servicing. Fig. 10 provides a sense of scale of the NuMI

workcell during construction with the target module inside for trial hot handling practice. The above noted elements are incorporated into the target station conceptual layout as an

Figure 10. NuMI Workcell for hot handling operations and failed component replacement. Image shows NuMI target module in the workcell for a hot handling procedure dry run during NuMI construction

input to the civil facility construction. Fig. 11 gives a plan view of the current version of the target station layout. Note that the layout incorporates a drop hatch and rail cart for rigging material into the complex for construction and removing failed components in a shielded transportation cask for long-term storage. A morgue is included in the layout for temporary storage of radioactive elements and failed component cool-down. The active functional area includes the target shield pile and beamline chase and an area that will be likely separated by a masonry wall to house power supplies, RAW water skids and a chase air handling system.

2. Pion Production Target

The nuSTORM baseline target is very similar to the NuMI low energy target used in the MINOS and MINERνA run from CY2005 thru CY2012. This style of target has undergone significant analysis and optimization during that time period. When properly constructed
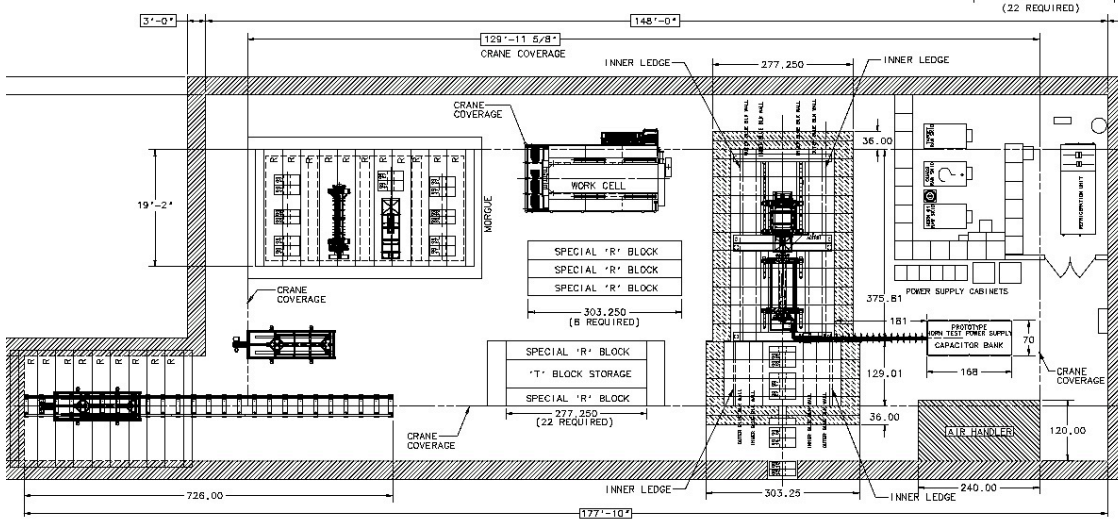
Figure 11. nuSTORM target station main level plan view.

and qualified by sufficient QA steps during construction, the target has been successfully operated for 6×10^{20} protons on target (NuMI target NT-02) at beam powers near 400kW and 4.4×10^{13} protons per pulse. Target replacement is, therefore, not expected for the 10^{21} POT exposure for nuSTORM.

Since the energy deposition is proportional to atomic number, Z, this style of low-Z target has been specified and successfully used in several neutrino experiments when coupled with a large depth of field focusing device, such as the magnetic focusing horn, to achieve high pion yields at a range of energies dependent upon the relative placement of target to horn. For the NuMI low energy beamline with 4.4×10^{13} protons on target, the energy deposition per pulse was calculated at 5.1 kJ per pulse. For the 400kW case cycle time of 1.87 seconds, the average power into the graphite is approximately 2.7kW. Scaling to nuSTORM with 0.8×10^{13} protons per pulse and a cycle time of 1.33 seconds, one expects a total average power of 770W. Note that these targets have successfully operated at much higher power levels.

Graphite possesses favorable material properties for pulsed-beam operation to minimize dynamic stress waves and thermal stress gradients including high thermal conductivity, relatively high specific heat capacity, relatively low thermal expansion and Young's Modulus of elasticity, possesses reasonable strength when considering the above properties, and is able to survive at high temperatures in the absence of an oxidizing (i.e., oxygen) environment. Scaling from the NuMI experience to the nuSTORM expected power levels and the inte-

grated yearly proton on target value, the graphite should not experience significant material irradiation damage for the specified beam parameters for several years of operation.

Physically, the nuSTORM current baseline design will consist of a 2-interaction length POCO graphite grade ZXF-5Q fin-style target. The target construction consists of 47 graphite target segments each 2 cm in length, 15mm in vertical height, and 6.4mm in width. The nominal target overall length is 95 cm, with the fins being brazed to a cooling pipe on the top and bottom surfaces of the graphite fin. Cooling of the target fins from beam interaction is accomplished via conduction of heat through the graphite fin to the cooling pipe water. The target core assembly is encapsulated in a thin-wall (0.4mm) aluminum tube to minimize pion absorption and capped at each end by a 0.25mm thick beryllium window. This allows the target canister to be evacuated and back-filled with helium to minimize graphite oxidation and provides a conduction path for cooling the outer aluminum tube at higher beam powers (note that for the NuMI low energy configuration the target inserts 60cm into the horn and not much external airflow is available for convection cooling on the outer surface of the aluminum tube). In addition, the thin-wall aluminum tube provides containment to mitigate the spread of radioactive contamination from target material degradation due to large amounts of beam exposure.

Colleagues from IHEP in Protvino, Moscow Region fabricated all NuMI low energy targets for the MINOS/MINERνA running that ended in CY2012. Towards the last $1\frac{1}{2}$ years of that run period, enhancements to the targets were made at Fermilab, including a prototype core fabrication of a complete ZXF-5Q graphite fin target brazed to a titanium cooling pipe. Analysis has shown this combination to be more robust than the prior targets which used a Russian proprietary grade of high-chromium steel cooling pipe. It is likely that some amount of engineering effort will be required to repackage and slightly redesign the low energy target for nuSTORM use, but given our experience and knowledge base, this effort is viewed as low risk and not requiring large amounts of manpower for redesign.

Efforts are ongoing to investigate the use of a medium-Z target material (e.g., Inconel 718) to enhance pion yield (see Section II B 2 a), but this effort will need to provide a thorough analysis of target material energy deposition and thermal-mechanical response as well as understanding the additional heat load input to the horn inner conductor from a higher-z target material.

Fig. 12 delineates the basic design of the nuSTORM target, which in the baseline configuration is very similar to the NuMI low energy targets. As previously noted, the NuMI
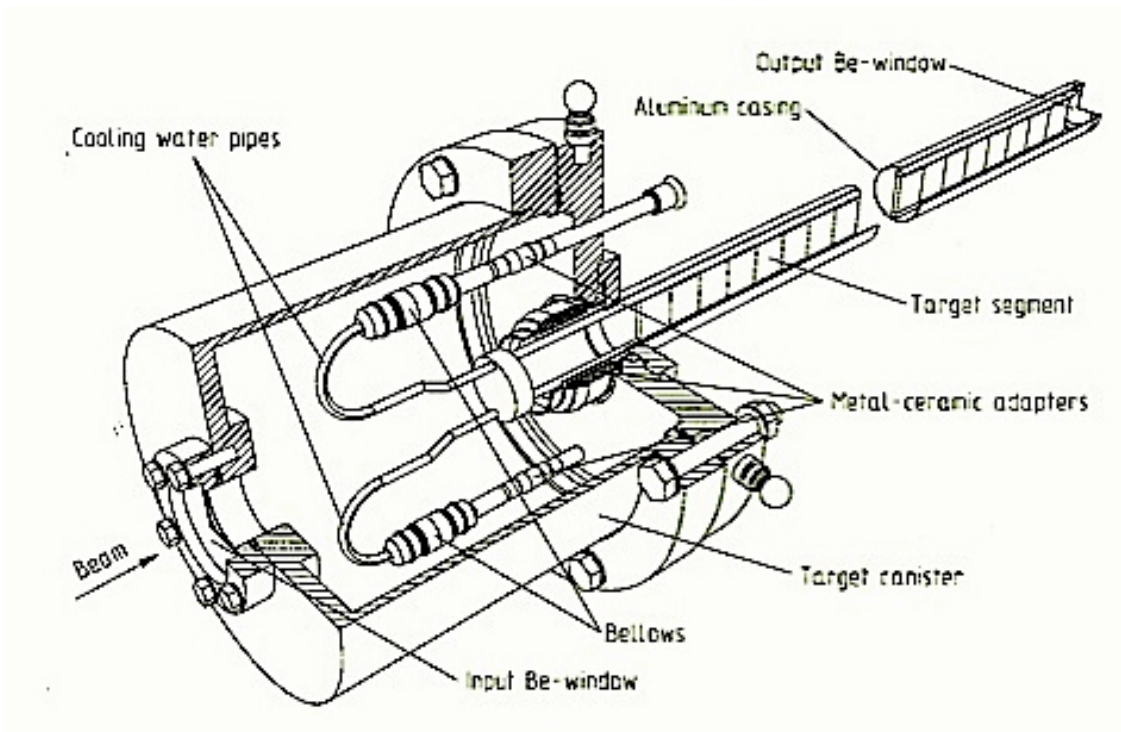

Figure 12. NuMI-style low energy graphite fin target.

target is designed in conjunction with the horn inner conductor shape to optimize neutrino production in the 1 to 3 GeV region. This low energy range is achieved by inserting the target 60cm into the field free bore-region of the horn. The target is mounted on a target carrier frame that allows for target z-motion of 2.5m along the beamline. This entire carrier frame is mounted to the positioning module and allows for different target to horn spacing or simply provides the means to insert the target into the horn for normal low energy running. Fig. 13 demonstrates the target to horn relationship.

Target Inserted into
Horn 60cm

Horn 1
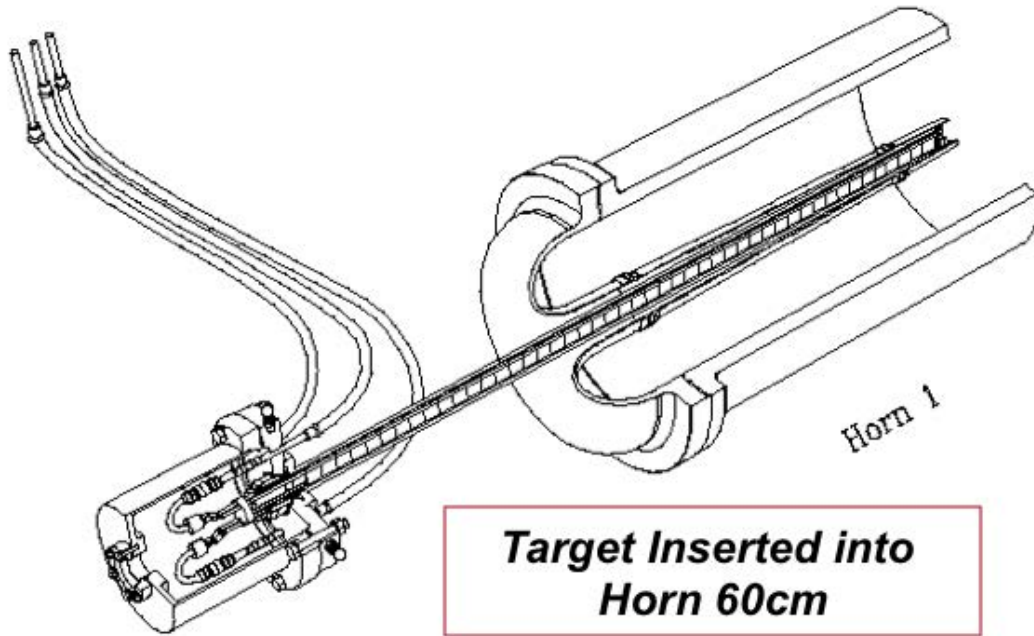
Figure 13. NuMI-style graphite fin target in low energy position (inserted into horn 60 cm).

Table III. MARS simulation parameters.

Parameter	Value Unit
Material	Inconel 718
Diameter	0.7 cm
Length	25 cm
Beam Energy	120 GeV
Beam $\sigma_{x,y}$	1.1 mm
Protons/pulse	8×10^{12}
Pulse Length	1.6 μsec
Rep Rate	0.752 Hz

a. INCONEL target option

Although the baseline nuSTORM production target material is graphite, as can be seen in Section II C, the use of Inconel gives up to a 40% increase in pion yield. We have, therefore, considered a cylindrical Inconel 718 target with a 7 mm diameter and 25cm length. We have performed an energy deposition study with MARS and have determined the resulting thermal load. Based upon this thermal loading, the resulting temperature profiles for a variety of cooling methods were evaluated, with forced Helium cooling being the leading candidate for further analysis. Basic structural analyses were also carried out, showing that further work on the structural design is necessary due to plastic deformation. Further analysis will be necessary to look into target geometry optimization, more realistic temperature estimates via CFD, dynamic stress effects, and resonant effects on the structural analyses.

1. MARS 15 Model and Results MARS15(2013) was used to calculate the energy deposition into the target from the incoming proton beam. The simulation parameters used are listed in Table III. Based on these inputs, the energy deposition was compiled and converted to a format suitable for input into ANSYS. The total heat loading on the target is about 4.8kW. A graphical, axisymmetric plot of energy deposition along the target is shown below in Fig. 14. The beam travels from left to right starting at the (0,0) point. It should also be noted that MARS15 predicts high DPA rates in the radial center of the target, with a peak of about 40DPA/yr. assuming continuous beam. Material degradation from radiation damage must be considered in the final design and target lifetime calculations. A plot of
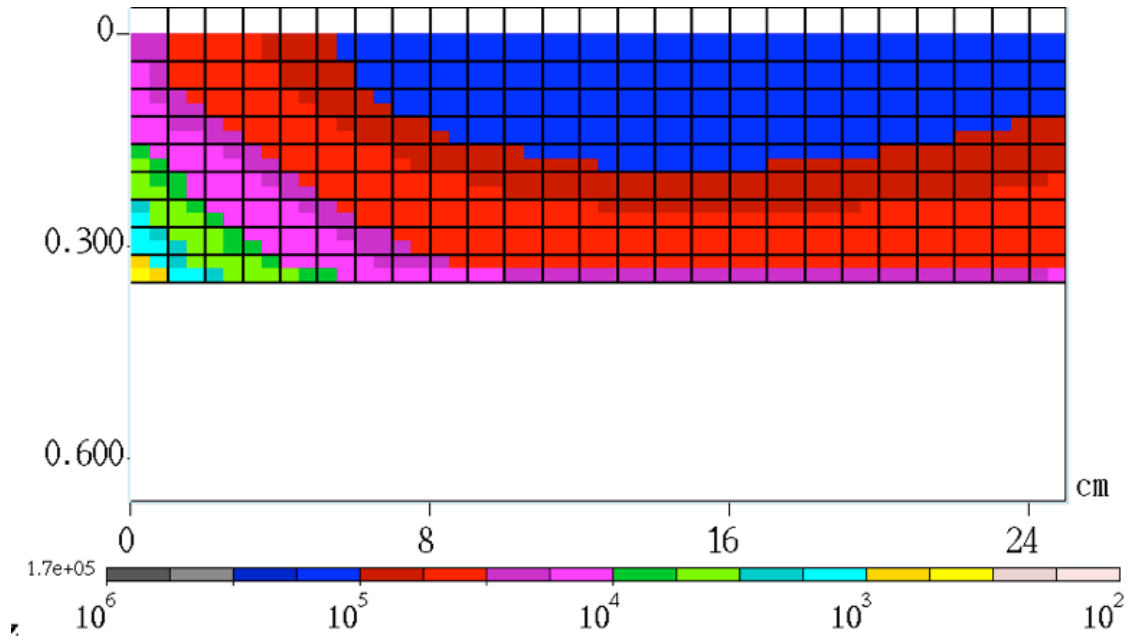
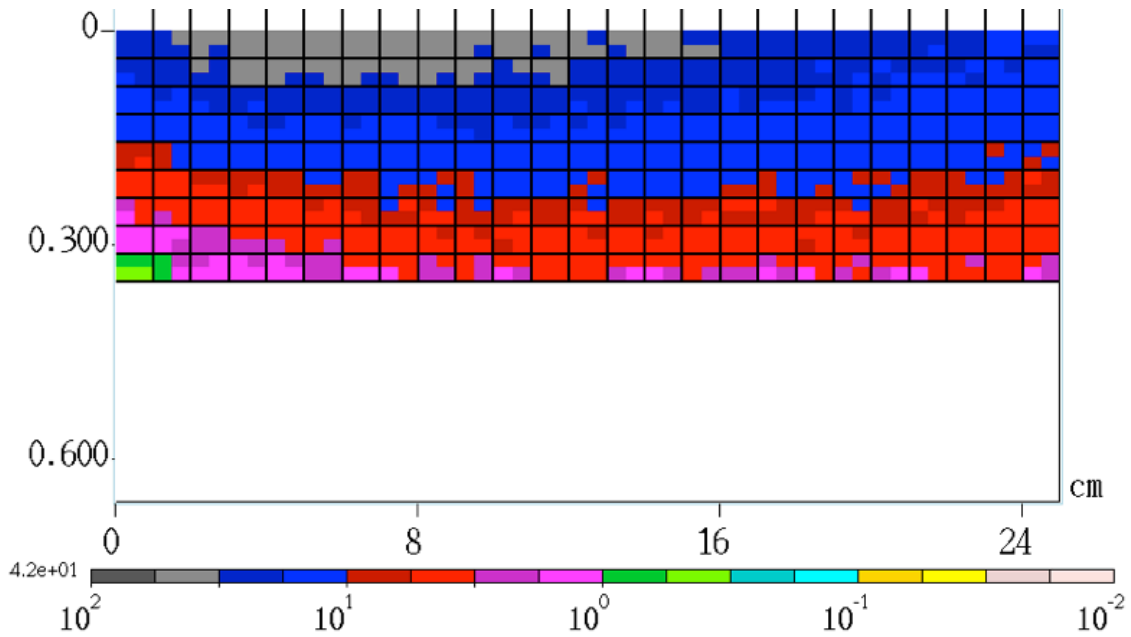Figure 14. Energy deposition [mW/g] into Inconel target.

DPA/yr is shown in Fig. 15.

Figure 15. DPA/yr in Inconel target.

2. ANSYS Simulations ANSYS 14 was used to calculate the thermal and structural effects from the energy deposition. Temperature dependent material properties for Inconel 718 were used for all analyses, containing information up to 1200C. A simple axisymmetric

26

Table IV. Steady state target temperatures with varying convection coefficients.

Method	Convection Coefficient	Peak Steady-State Temperature	Peak Fluid Interface Temperature
	[W/(m^2-K)]	°C	°C
Forced Helium (1 bar, mach 0.3)	1500	1065	950
Forced Air (10 bar, mach 0.3)	3500	580	420
Forced Helium (10 bar, mach 0.3)	10000	370	160
Water (5 m/s)	25000	310	80
Water (10 m/s)	45000	285	55

model was used for initial scoping to minimize simulation time. PLANE77 (thermal) and PLANE183 (structural) elements were used with a size of 0.4mm to accurately capture the maximum temperatures ($\simeq$ 3 elements per beam sigma) and resulting stress effects.

Thermal analysis - Steady state

A convection boundary condition was placed on the outer surfaces of the target and was varied according to different cooling methods as shown in Table IV with a reference temperature of 22°C. It should be noted that this model does not include heating of the fluid from flow along the surface. The fluid is also assumed to be in full contact with the outer wall of the target. A full CFD model will be necessary for accurate predictions of all temperatures. Pressurized Helium and Air both appear to be possible candidates for further study, and water cooling will need further analysis to determine the fluid interface temperature during the dynamic effect of a beam pulse. Optimizations of target geometry would also be helpful to reduce peak steady state temperatures.

Thermal analysis - Steady state + transient effects

To understand the peak temperatures at both the radial center of the target and the cooling fluid interface immediately following a pulse, a transient thermal analysis was run. This run uses a steady state heat generation profile until the steady state temperature is reached (5-15s), then the heat generation from a pulse is applied for 1.6μs.. A typical plot of temperature vs. time is shown in Fig. 16. Using the same boundary conditions and convection coefficients as in the previous analysis, peak steady state temperature, peak temperature in the target, and peak temperature at the fluid interface were found and are shown in
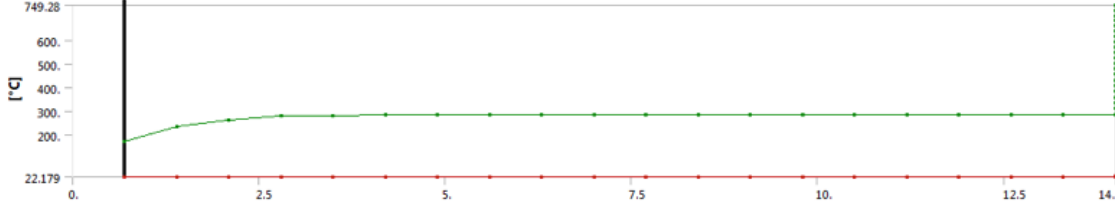
Figure 16. Typical temperature vs time profile for transient case.

Table V. Steady state + transient target temperatures with varying convection coefficients.

Method	Convection Coefficient	Peak Steady-State Temp.	Peak Temp. After Pulse	Peak Fluid Interface Temp.
	[W/(m²-K)]	°C	°C	°C
Forced Air (10 bar)	1500	-	-	
Forced Helium (1 bar)	3500	580	1010	585
Forced Helium (10 bar)	10000	370	820	350
Forced Water (5 m/s)	25000	310	770	**270**
Forced Water (10 m/s)	45000	285	750	**245**

Table V. Temperatures listed are obtained immediately after the pulse is applied. Water cooling can be ruled out since the interface temperature is above the boiling point of water and could lead to accelerated corrosion and pitting. Pressurized Helium appears to be the leading candidate for cooling based on this analysis.

Structural analysis - Steady state + transient effects

A structural model was constructed in the same manner as the previous transient thermal analysis to determine the stress state of the target both in the steady state condition and after a beam pulse. Refer to Fig. 16 for a plot of temperature over time. Instead of modeling multiple pulses of the beam and observing the ratcheting effect, this method saves some simulation time while giving accurate results. Only two cooling cases were analyzed: the compressed air and helium cases. A large temperature gradient develops across a very short radial dimension which induces a large stress in the material. A typical plot of maximum principal stress is shown in Fig. 17 where blue colors are compressive and red colors are tensile. The peak steady-state Von-Mises stress for both cooling cases is listed in Table VI. Fig. 18 shows the temperature dependent tensile yield and ultimate strengths for Inconel 718. Steady state stresses are relatively low for this material and temperature. Next the

E: Transient Structural
Maximum Principal Stress
Type: Maximum Principal Stress
Unit: MPa
Time: 14.
5/3/2013 3:38 PM

985.2 Max
842.6
699.99
557.38
414.78
272.17
129.57
-13.041
-155.65
-298.25 Min
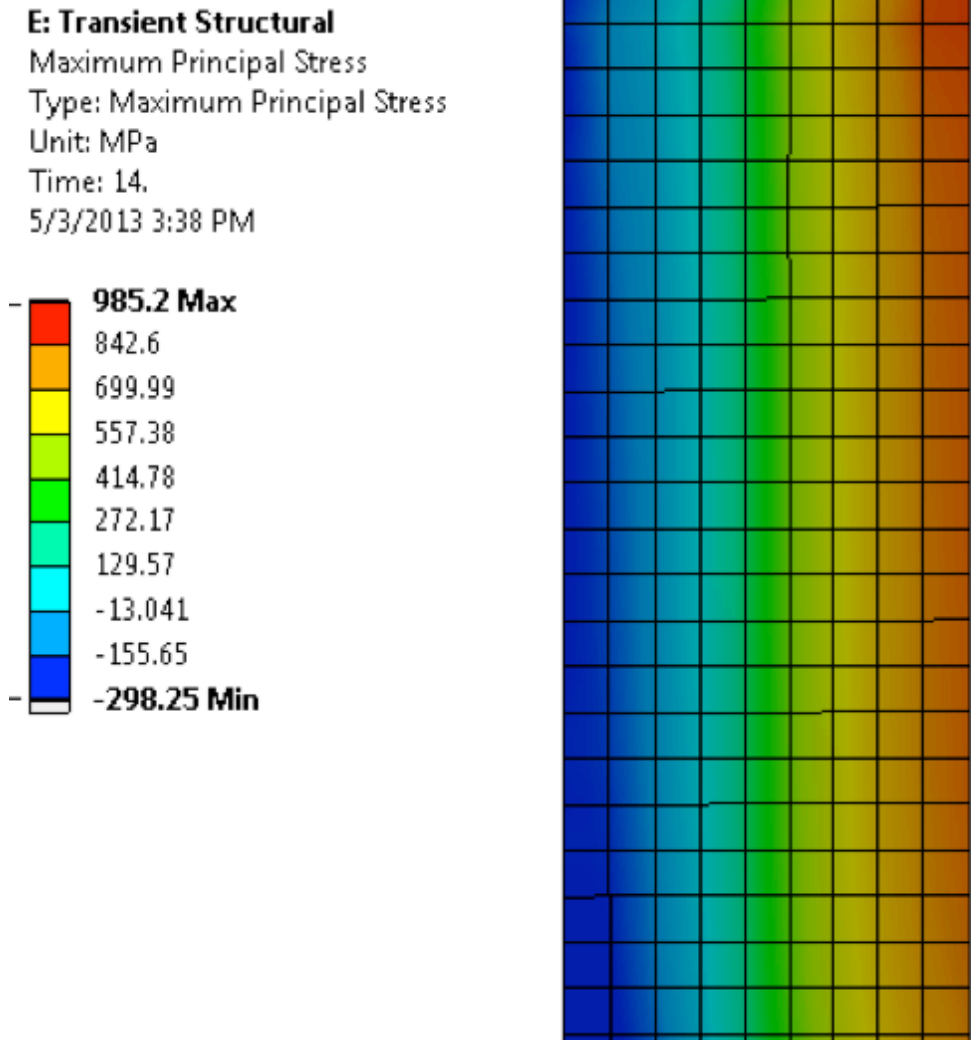
Figure 17. Typical maximum principal stress plot.

Table VI. Steady state VM stress for various cooling methods.

Convection Coefficient	Peak VM Stress Steady State
W/(m²-K)	Mpa (ksi)
3500	300 (44)
10000	380 (55)

transient effects were evaluated with a beam pulse after the steady state temperature was obtained. Table VII shows the peak tensile and compressive temperatures and stresses. While it is possible that there will be no yielding on the outer surface of the target, yielding will most likely occur in the radial center of the target where the compressive stress is concentrated. Segmenting the target may help reduce the stress and should be further analyzed.

29
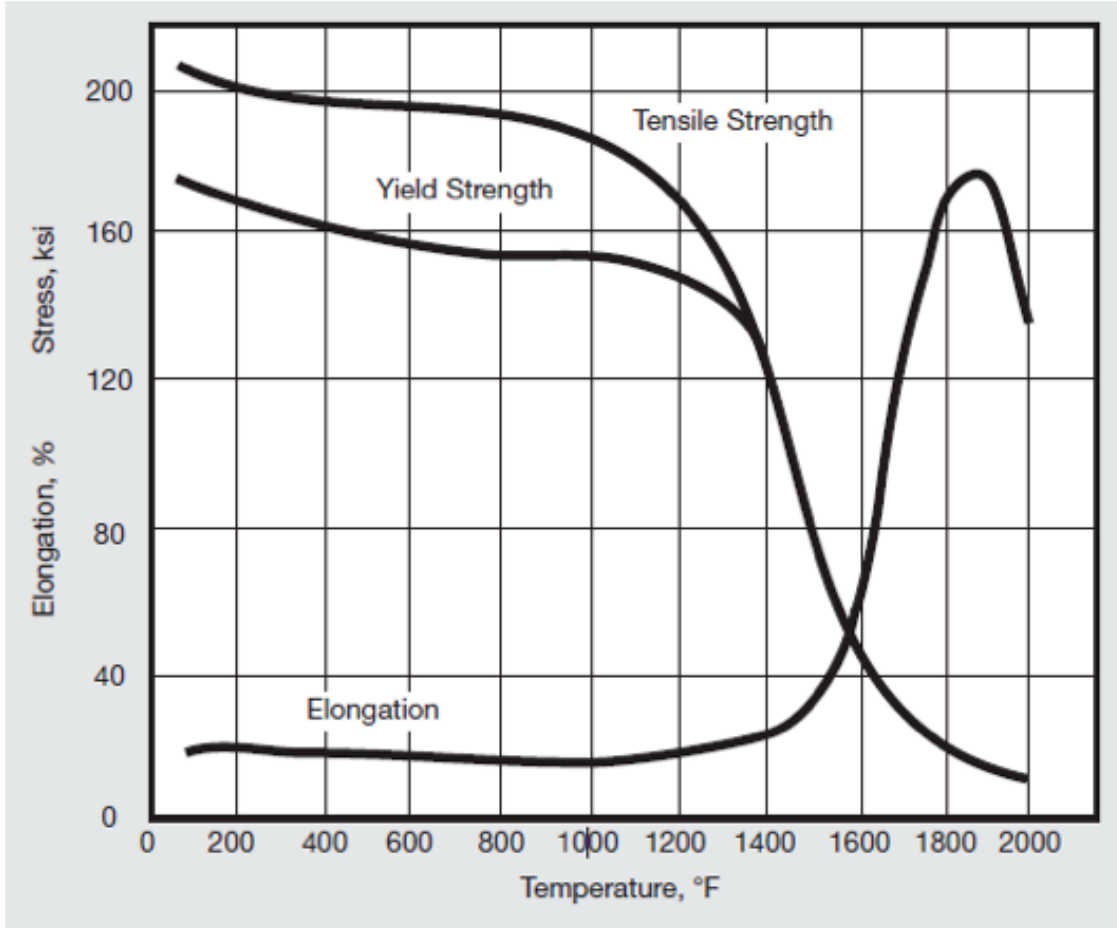
Figure 18. Tensile yield, ultimate strength, and elongation as a function of temperature.

Table VII. Peak temperatures and stresses after pulse.

Convection Coefficient	Peak VM Stress Steady State
W/(m^2-K)	[Mpa (ksi)]
3500	300 (44)
10000	380 (55)

3. **Next steps in the analysis for Inconel** Further analysis of the Inconel target is needed in at least four areas to get a better understanding of the beam response and interaction with the target geometry:

- Fluid flow and heating (CFD)

- Dynamic stress effects

- Resonant effects

- Target segmentation

30

CFD analysis is needed to determine a more accurate temperature profile of the target. ANSYS thermal calculations do not include fluid heating and this can only be evaluated with a CFD model. Dynamic stress waves have been shown to increase stress in a target by up to 2× depending on the geometry because of the interference between stress waves. This effect needs to be studied with a longer run after the beam pulse with short time-steps. Resonant modes of the target will also come into play and have an effect on the dynamic stress. A modal analysis needs to be conducted to determine the resonant modes of the target and any supporting structures. The effect of target segmentation needs to be looked at, including all of the previously described areas for further analysis. It has also been suggested to investigate the additional heat loading onto the horn because of the larger shower coming from the target. This can be done with a fairly simple MARS model. While a completely solid target will undergo plastic deformation during a beam pulse, optimization of the geometry may allow the target stresses to be reduced to an acceptable range. Geometry optimization would also allow lower steady state temperatures and stresses. Further analysis is needed to define an optimized target geometry.

3.   Focusing Horn

The primary objective of the focusing horn is to collect the pion phase space from the target interaction with the primary beam and focus the pions such that they are stably captured by the quadrupole magnets just downstream of the horn. This leads to several requirements of the horn for reliable and effective operation:

1. The horn should have the ability to operate at sufficiently high currents to maximize the pion focus to the capture quadrupoles.

2. The inner conductor of the horn should be sufficiently thin to minimize absorption of off-axis pions produced in the target that enter the field region of the horn.

3. The horn should have sufficient structural integrity to survive a reasonable number of high current pulses with adequate safety factor to allow reliable operation for several years of service.

4. The horn should employ radiation hard structural and insulating materials.

5. The horn should employ suitable corrosion resistant materials to mitigate erosion of the thin-wall inner conductor from the water-cooling spray.

6. The horn should be designed with a fabrication tolerance that assure uniform field region.

7. The horn should have adequate cooling plus overhead for the expected 100kW beam power and the 200kA (or higher) current pulse.

The horn provides large depth of field focusing compatible with a low-Z target in order to maximize the pion capture rate. This is achieved by using a target with a small cross-sectional component. allowing pions to exit the target material without further interaction. Pions with a nearly on-axis trajectory travel through the field free region of the inner bore of the horn inner conductor, while pions with an off-axis trajectory travel through the thin-wall inner conductor of the horn into the field region and are subject to a focusing force vector which is proportional to the vector cross-product of instantaneous velocity and the magnetic field vector. The selection of the horn inner conductor thickness is a balance between minimizing pion absorption, providing adequate thickness to allow for precision machining and fabrication, and providing adequate margin of safety relative to the operating stress that results from the thermal components of secondary particle beam heating, joule heating from current pulse resistive heating, and the magnetic forces from the interaction of current density and magnetic field. Fig. 19 outlines the basic structure of the focusing horn. nuSTORM expects to utilize the successful operational experience of NuMI and the baseline configuration consists of a NuMI style horn 1. The NuMI horns have operated successfully for more than 3×10^6 pulses of operation with average beam powers as high as 375kW and maximum proton intensity of 4.4×10^{13} protons per pulse. In addition, significant analysis and understanding of horn operational characteristics and reliability exists at Fermilab. Such analyses are well documented for the 400kW NuMI/MINOS beamline operation, the upcoming 700kW NOvA era running, and the 700kW baseline LBNE configuration. In particular, a recent analysis for LBNE indicates that it may be possible to operate with adequate safety margin at horn currents of 230kA for the 700kW LBNE beam. It is believed that this scenario is likely for nuSTORM, but would require some further analysis to understand the entire load history to accurately calculate the fatigue life safety factor. Note that the fatigue life value is highly dependent upon the coupled loading of beam thermal energy,
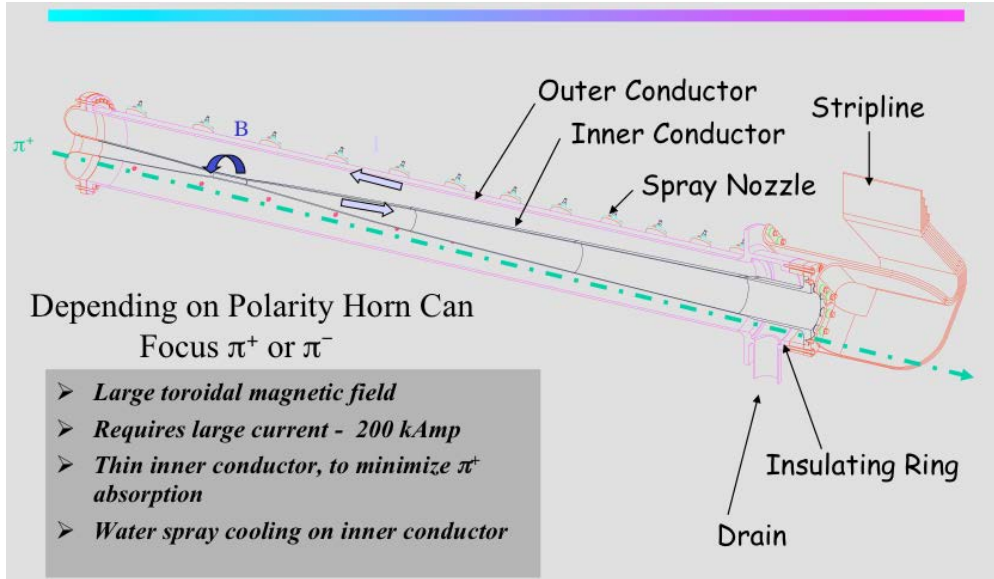
Figure 19. NuMI Horn 1 basic elements.

current pulse resistive heating, and magnetic loading stress value and sign (compressive vs. tensile stress), as the magnitude of alternating stress has significant effect on fatigue life.

An additional consideration for using a NuMI-style horn is that Fermilab has the infrastructure for, and experience in, fabricating all NuMI horns to date. A few examples of the benefits to such expertise in addressing the challenge of fabricating these critical devices include the in-house CNC welding and straightening of the inner conductor structure to very high tolerances ($\pm$ 0.25mm), a ready design with little modification for nuSTORM use (i.e., minimizes the cost of manpower for a new design or substantial redesign), and the infrastructure to pulse test and field map a finished horn before beamline installation. Fig. 20 shows a NuMI horn 1 ready spare. The design package of a new-style horn, module, and supporting hardware represents significant manpower effort and cost. It is envisioned that nuSTORM can utilize most elements of the NuMI design. The fabrication costs and operating envelope are well understood. Minor design effort does exist in that the horn hangers and module for NuMI are designed for a beamline pitch of 58 milliradians. The nuSTORM beamline pitch is level. Such modifications to the NuMI horn and module design are viewed as relatively minor when compared to more substantial redesign efforts and are expected to pose negligible risk to design reliability. Fig. 21 depicts the NuMI horn 1 package during the installation into the NuMI beamline. Similar hardware is specified for the target, the first 2 capture quadrupoles immediately downstream of the horn, and beam spray protection

Figure 20. NuMI Horn 1 ready spare.

collimators for those quadrupole magnets.

Figure 21. NuMI Horn 1 and positioning module installation in beamline chase.

4. Quad capture magnets

Unlike a conventional neutrino beam where pions exiting the horn are launched into a decay pipe, in nuSTORM we have a pion capture and transport channel that brings the pions to the decay ring. The initial part of this section (just downstream of the horn) consists of two quadrupoles. They are in the target chase and see a very large radiation dose and, therefore, must be radiation hard. There are two options we have considered: MgO insulated magnets and HTS magnets following the BNL magnets designed for the Facility for Rare

Isotope Beams (FRIB) [36]. The current baseline design for the capture quad section of the pion capture channel (see Section II C 1) uses magnets with a 40 cm bore. However, recent studies indicate that a 20 cm bore can be used with little loss in flux. This would allow nuSTORM to use the same magnets that have been designed for FRIB and would represent a substantial cost savings. These magnets have a unique design and technology that uses Second Generation (2G) High Temperature Superconductor (HTS). These magnets can survive very intense heat and radiation loads (up to 10 MGy/year) and can operate at an elevated temperature of 40 K, instead of $\simeq$ 4 K as needed in the conventional low temperature superconductors. This elevated temperature has a major impact regarding the heat load on the cryogenic system. In addition, a large temperature margin allows for robust operation by tolerating a large local increase in temperature. These HTS quadrupoles are the baseline design for the fragment separator region of FRIB which follows the production target ($\simeq$ 400 kW beam power).

The BNL magnet group [37] has looked into the feasibility of a HTS Quad with a 40 cm bore for nuSTORM. Fig. 22 shows the preliminary magnetic design and field contour for this magnet.
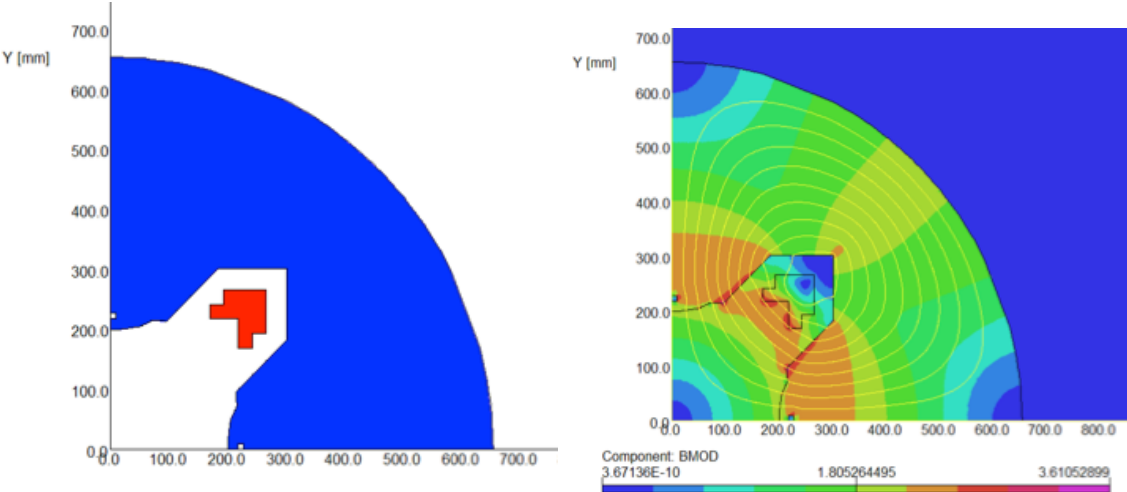
Figure 22. A preliminary magnetic design of the HTS quadrupole for nuSTORM (model on left and field contours on right). In the model, blue represents the warm steel and the red represents the HTS conductor.

C. Pion Production

It is known that the maximum pion yield can be achieved with a target radius ~ 3 times the proton beam RMS size. The optimal target length depends on the target material and the secondary pion momentum. The results of our optimization study are presented in Table VIII. We see that approximately 0.11 π^+/POT can be collected into $\pm 10\%$ momentum acceptance off medium to heavy targets with very small proton beam size (0.15 mm). The difference between the yield from heavy and light targets becomes about $2 \times$ smaller for a more realistic beam size with a 1 mm RMS. These numbers are for pions within the 2 mm-radian acceptance of the decay ring.

We have considered two options for pion capture, a lithium lens and a horn. The existing Fermilab lithium lens has a working gradient of 2.6 Tesla/cm at 15 Hz. The optimal distance between the target and lens center is about 25 cm. Pions produced into 2 mm-radian acceptance have a wide radial distribution, however. The current lens with its 1 cm radius would only capture 40% of the pions within the desired $\pm 10\%$ momentum acceptance. With a 2 cm lens radius, the pion capture efficiency increases to 60%. Further improvement could be achieved by increasing the lens gradient, but increasing the gradient reduces the focal length. Maximal efficiency would reach 80% with a 4 Tesla/m gradient and a 2 cm lens radius. These parameters are beyond the state-of-art for an operating lens, however, and the target's downstream end would need to be very close to the lens. Therefore for nuSTORM, we have abandoned consideration of a Li Lens.

The existing NuMI horn was considered as the other capture option. Different target materials, horn currents, beam RMS sizes (target size) were studied. Results for a 60 GeV/c proton beam are presented in Table IX. We see that approximately 0.06 π^+/POT can be captured into a $\pm 10\%$ momentum acceptance for 1 mm (σ_b^{rms}) proton beam. Yield can be increased by using a heavy target and very small beam transverse size.

Approximately twice as many pions can be collected with 120 GeV/c protons and a NuMI-style horn. Table X presents the pion yield dependence on target material for this configuration. Using a conventional graphite target and NuMI horn at 230 kA, 0.094 π^+/POT are captured after the horn into the 2 mm-radian acceptance. The phase-space distribution of pions downstream of the target and downstream of the horn are shown in Fig. 23 and

Fig. 24, respectively. The ellipse shown in each figure represents the acceptance of the muon decay ring.

120 GeV proton, $\sigma_x = \sigma_y = 1$ mm
graphite target, 95cm long, 3 mm radius, 5cm after target
π^+: $\delta p/p = 0.1$, $\varepsilon = 2$ mm rad, $\beta = 337.5$ cm, $\alpha = -3.5$
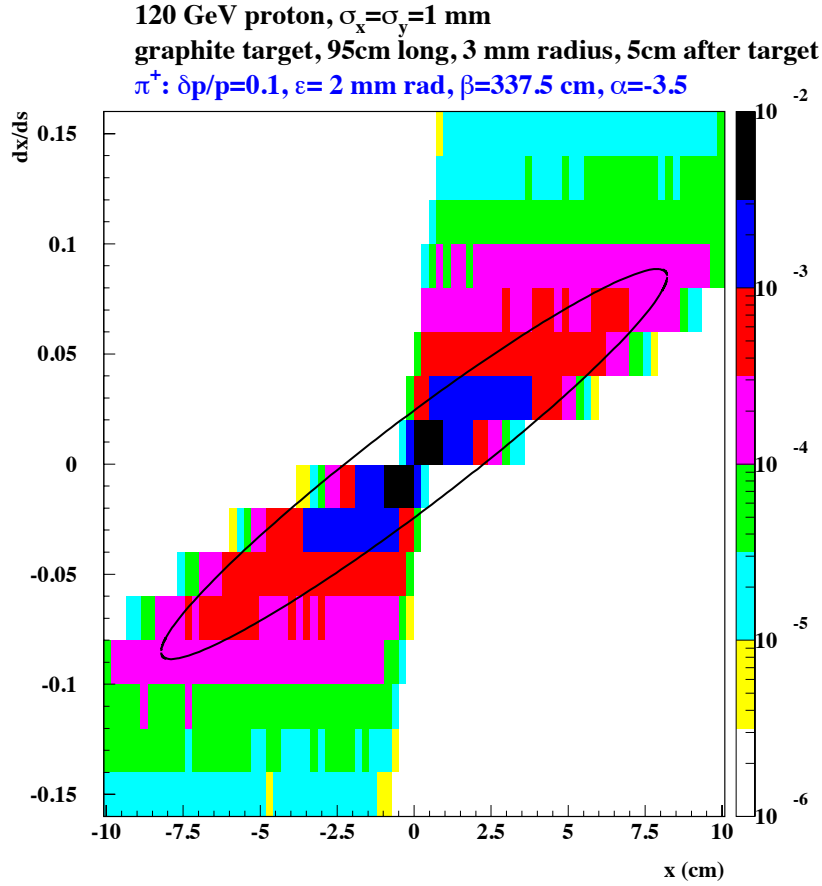
Figure 23. Phase-space distribution of pions 5 cm downstream of target

1. Capture and Transport

As described in the previous section, the pion distribution at the downstream end of the horn was simulated and generated by MARS. A shell script code converts the MARS output to G4beamline[38] conventions, for the simulation's input beam. Another script converts OptiM[39] lattice output to G4beamline lattice input. Assuming a phase space acceptance of 2 mm·rad for pions, it is convenient to fit the transverse distribution to a 2D Gaussian with a covariance matrix obtaining Courant-Snyder(CS or Twiss) parameters [40]. These parameters are used for the matching condition for designing the transport line.

From the downstream end of the horn, we continue the pion transport line with several

Table VIII. π^+ yield/POT at 60 GeV into 2 mm radian acceptance.

material	momentum (GeV/c)	±15%	±10%	±5%	target length (cm)	density (g/cm^3)	σ_b (mm)
Carbon	3	0.085	0.056	0.028	27.3	3.52	0.15
Carbon	5	0.099	0.067	0.033	32.2	3.52	0.15
Inconel	3	0.131	0.087	0.044	19.2	8.43	0.15
Inconel	5	0.136	0.091	0.045	27.0	8.43	0.15
Tantalum	3	0.164	0.109	0.054	15.3	16.6	0.15
Tantalum	5	0.161	0.107	0.053	21.3	16.6	0.15
Gold	3	0.177	0.118	0.059	18.0	19.32	0.15
Gold	5	0.171	0.112	0.056	20.0	19.32	0.15
Gold	5	0.143	0.094	0.047	20.0	19.32	1.
Graphite	5	0.085	0.057	0.028	95.0	1.789	0.15
Graphite	5	0.096	0.064	0.032	95.0	1.789	1.

Table IX. π^+ yield/POT at 60 GeV into 2 mm radian acceptance after NuMI horn. 5 ± 0.5 GeV/c

material	Current (kA)	horn length (cm)	σ_b^{rms} (mm)	α	β (cm)	yield
Gold	300	200	0.15	0.	522.5	0.081
Gold	300	300	0.15	0.	427.5	0.077
Gold	300	200	1.	0.	542.5	0.063
Gold	300	300	1.	0.5	812.5	0.059
Graphite	300	200	.15	0.5	257.5	0.049
Graphite	300	300	.15	0.5	202.5	0.049
Graphite	300	200	1.	0.5	282.5	0.056
Graphite	300	300	1.	0.	217.5	0.056
Graphite	185	200	1.	-1	682.5	0.056
Graphite	185	300	1.	-0.5	987.5	0.054
Graphite	230	200	1.	0.5	512.5	0.057
Graphite	230	300	1.	0.5	687.5	0.056
BeO	230	200	1.	0.	602.5	0.065
BeO	230	300	1.	0.5	782.5	0.066
NuMI tgt	185	200	1.1	-1.5	852.5	0.056
NuMI tgt	185	300	1.1	-0.5	1097.5	0.054
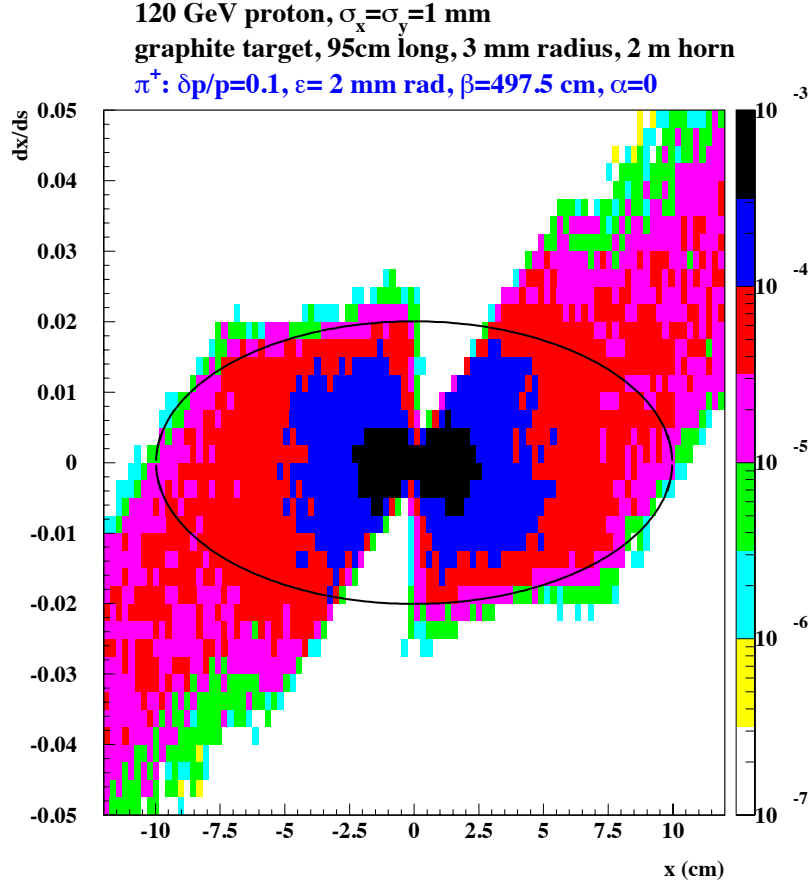
Figure 24. Phase-space distribution of pions downstream of the horn

Table X. π^+ yield/POT after NuMI horn at 230 kA. 120 GeV/c proton beam with 1 mm RMS. 5 ± 0.5 GeV/c

material	target length(cm)	horn length (cm)	α	β (cm)	yield (2 mm rad)	yield (r≤20 cm)
Graphite	95	200	0.	497.5	0.094	0.156
Graphite	95	300	0.5	612.5	0.092	0.139
BeO	66	200	0.	547.5	0.115	0.174
BeO	66	300	0.5	742.5	0.115	0.154
Inconel	38	200	-0.5	742.5	0.122	0.179
Inconel	38	300	0.5	897.5	0.126	0.157

quadrupoles. Although conventional from the magnetic field point of view, these first two to four quads still need special and careful treatment in their design in order to maximize their lifetime in this high-radiation environment. As described in Section II B 4, the FRIB quads show promise regarding suitability for nuSTORM.

40

The injection scenario for the decay ring, that will be discussed in section II D, needs a large dispersion value at the injection point. This dispersion D_x and its derivative D'_x both need to be matched to 0 at the horn, although this is not necessarily the case in the whole transport line. Considering this constraint, along with the requirement for spacing between target station and decay ring, two bending dipoles are used in the transport line, which bend the pions to the ring injection point. Two long drift spaces are reserved before the first dipole for collimators to reduce downstream radiation. The field strength, which is roughly 4.9 T in the first dipole, requires it to be superconducting. The long distance between the two dipoles separates the pions from the high energy residual protons, which go into a separate transport line and then into a MI-style proton absorber.

2. Proton Absorber

The current design uses the same proton absorber size that the MI uses, which is 4.3 meters both in width and height, and 10.7 meters in length. Because the first dipole also bends the protons at the same time as the π^+ or π^-, another long dipole is needed in order to bend protons back to their initial direction. No other magnets are needed for the proton absorber beam line. The layout drawing is shown in Fig. 25. The absorber, located at ~ 32 meters after the second dipole in Fig. 25 collects 43.5% of the total energy from the residual protons remaining after the target.
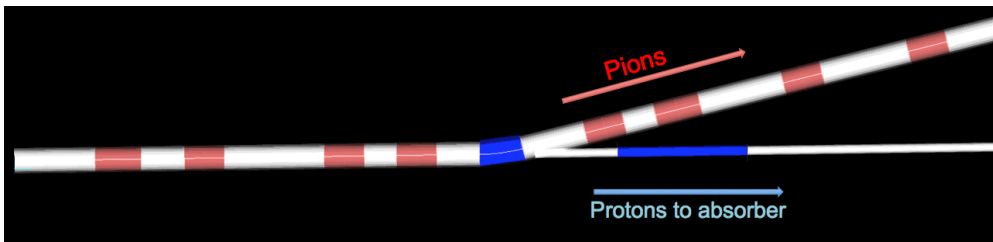
Figure 25. Separation of proton absorber beamline and pion transport line. Red: quadrupole, Blue: dipole, White: drift.

D. Pion Injection

The straight-section FODO cells were designed to have betatron functions β_x, β_y (the Twiss parameters) optimized for beam acceptance and neutrino beam production. Larger betatron

functions increase the beam size, following $\sigma =\sim \sqrt{\beta \epsilon_{rms}}$ and cause aperture losses. On the other hand, smaller betatron functions increase the divergence of the muon beam and also the divergence of the resulting neutrino beams, following $\delta\theta =\sim \sqrt{\epsilon_{rms}/\beta}$. In addition, the muon beam emittance is increased by the angular divergence from pion decay following $\delta\epsilon \sim \beta_t \theta_{decay}{}^2/2$.

Balancing these criteria, we have chosen FODO cells with $\beta_{\max} \sim 30.2$ m, and $\beta_{\min} \sim 23.3$ m for the 3.8 GeV/c muons, which for the 5.0 GeV/c pions, implies ~ 38.5 m and ~ 31.6 m pion's $\beta_{\max}$ and $\beta_{\min}$, respectively.

Fig. 26 shows results of a set of simulations used in determining this lattice design, showing the relative increase in angular divergence obtained by reducing the FODO betatron functions.
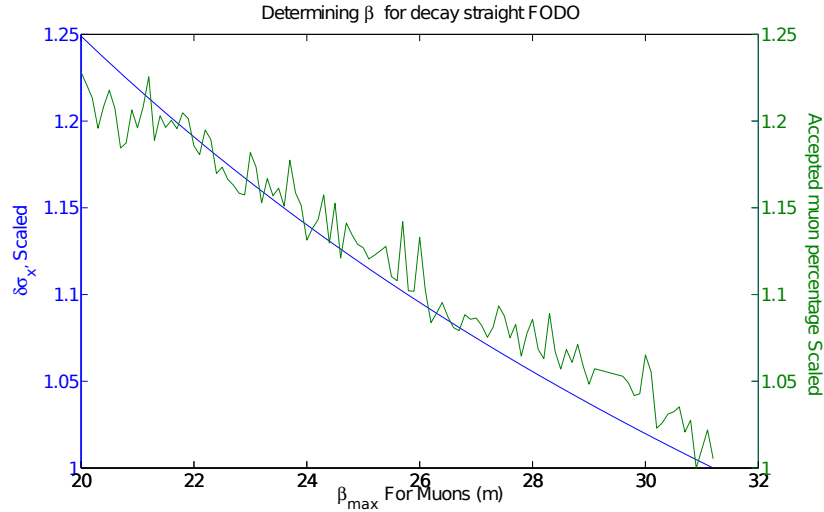
Figure 26. Determining the Twiss for decay straight FODO cells

As discussed in section II C 1, a large dispersion D_x is required at the injection point, in order to achieve beam separation. A carefully designed "beam combination section", or "BCS", can readily reach this goal. The schematic drawing of the injection scenario is shown in Fig. 27. The pure sector dipole for muons in the BCS has an exit angle for pions that is non-perpendicular to the edge, and the pure defocusing quadrupole in the BCS for muons is a combined-function dipole for the pions, with both entrance and exit angles non-perpendicular to the edges. The corresponding optics from OptiM are shown in Fig. 28. The BCS will be followed by a short matching section to the decay FODO cells (see Fig. 29). At the other end of the decay straight, another BCS will be used to extract the pions which
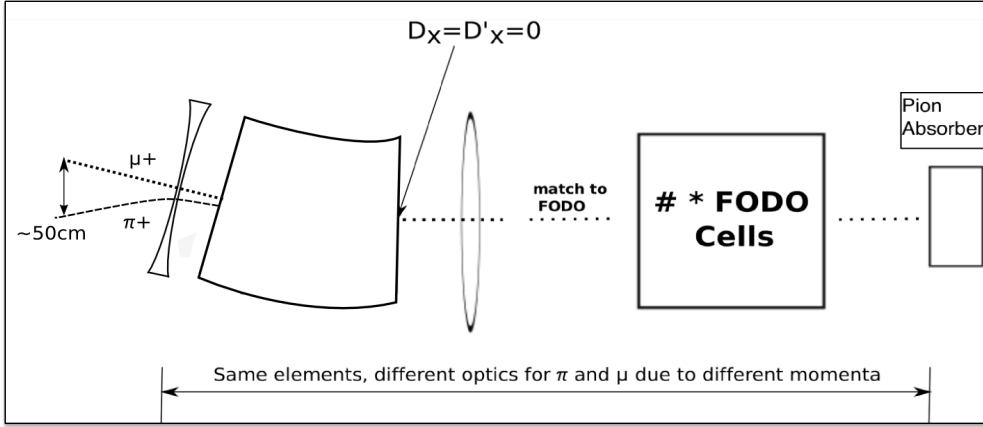
Figure 27. The schematic drawing of the injection scenario
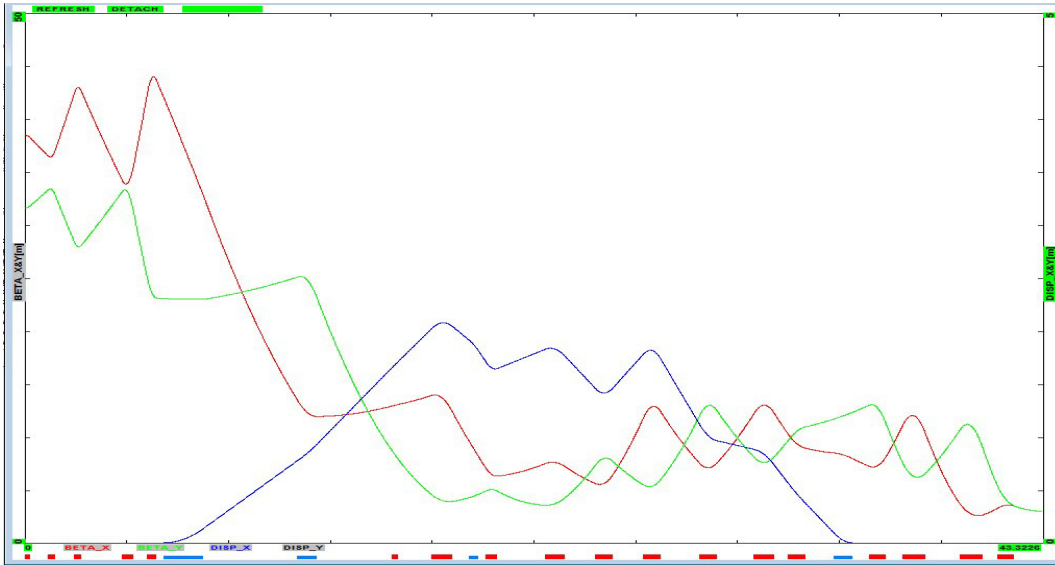
Figure 28. The optics of π transport and injection. The optics shown start in the decay straight and end at the downstream end of the horn (left to right).larger

have not decayed. This BCS, which also extracts muons within the pion momentum range, will be discussed in Section II F.

The performance of the injection scenario can be gauged by determining the number of muons at the end of the decay straight using G4beamline. We were able to obtain 0.012 muons per POT (see Fig. 30). These muons have a wide momentum range (beyond that which the ring can accept, 3.8 GeV/c $\pm$ 10%) and thus will only be partly accepted by the ring. The green region in Fig. 30 shows the 3.8$\pm$10% GeV/c acceptance of the ring, and the red region shows the high momentum muons which will be extracted by the BCS. This will be discussed in Section II F. The muons also occupy a very large phase-space, which is also
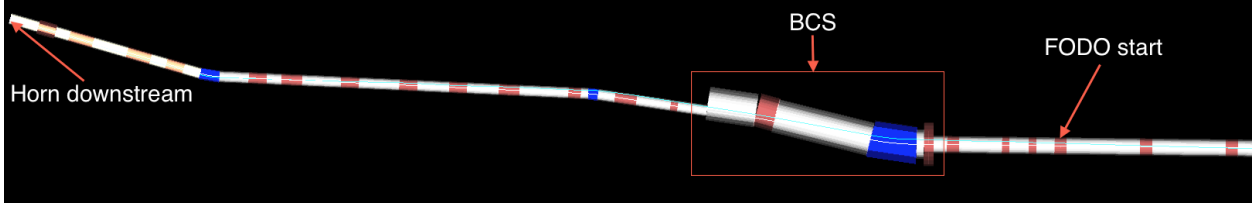
Figure 29. The G4beamline drawing from horn downstream to the FODO cells. Red: quadrupole, Blue: dipole, White: drift.

shown in Fig. 30.
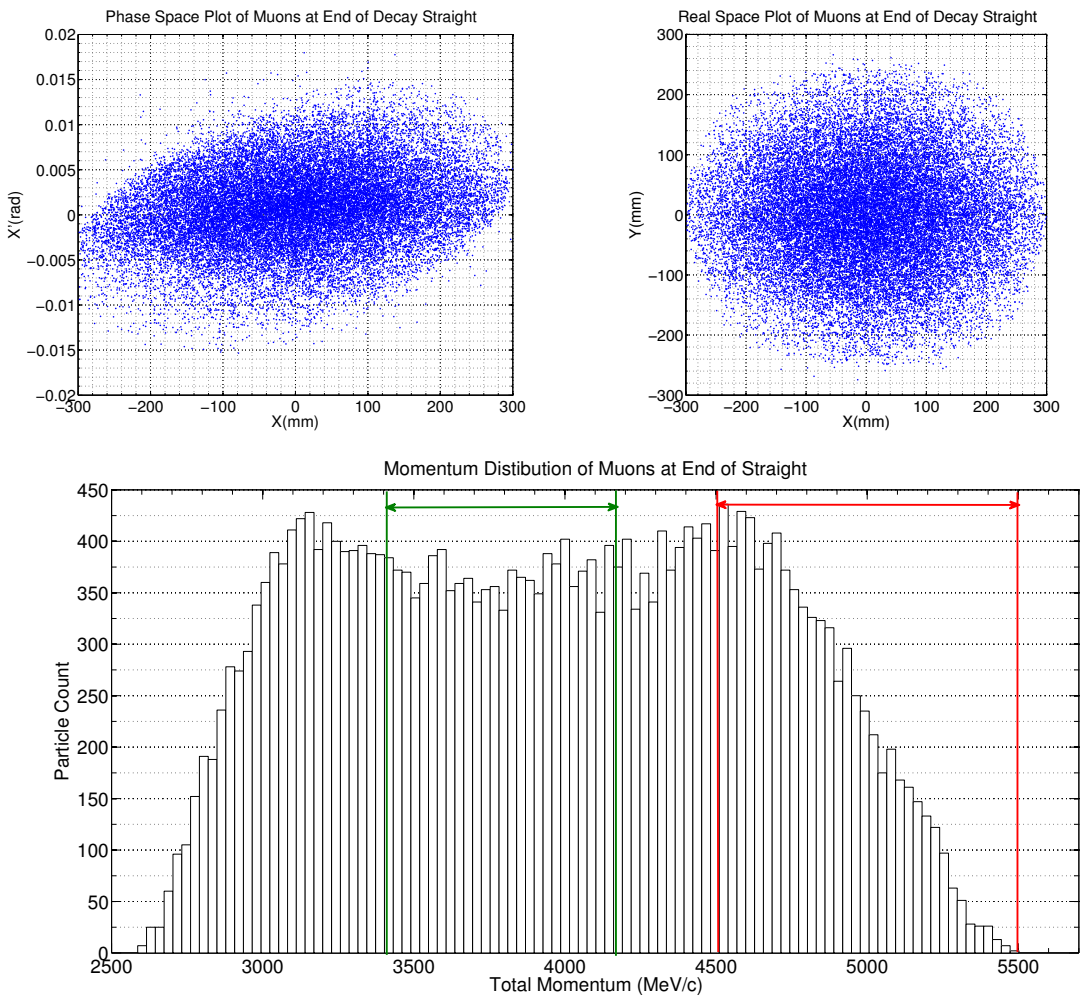
Figure 30. The muon real space distribution (upper right), phase space distribution (upper left) and the muon momentum distribution (lower) at the end of decay straight.

E. Decay ring

We have investigated both a FODO racetrack and a FFAG racetrack for the muon decay. The FODO ring that is described in detail below uses both normal and superconducting magnets. A FODO lattice using only normal-conducting magnets (B $\lesssim$ 1.8T) is also being studied. The racetrack FFAG (RFFAG) is described in Section II E 2. Table XI gives a comparison between the FODO and the RFFAG with regard to the ratio of the total number of useful muons stored per POT, assuming that capture off the target and injection into the ring are the same for both. Acceptance for all the decay ring options we are considering will be studied and compared in order to obtain a cost/performance optimum but, for now, the FODO lattice is the nuSTORM baseline.

Table XI. Relative μ yield for FODO vs. RFFAG rings

Parameter	FODO	RFFAG
$L_{straight}$ (m)	185	240
Circumference (m)	480	606
Dynamic aperture A_{dyn}	0.6	0.95
Momentum acceptance	$\pm$ 10%	$\pm$ 16%
π/POT within momentum acceptance	0.094	0.171
Fraction of π decaying in straight (F_s)	0.52	0.57
Ratio of $L_{straight}$ to ring circumference (Ω)	.39	.40
Relative factor ($A_{dyn} \times \pi$/POT $\times F_s \times \Omega$)	0.011	0.037

1. FODO ring Lattice Design

A FODO ring with such a large phase space and momentum acceptance has not been previously developed [41]. Here we propose a compact racetrack ring design (480 m in circumference) based on large aperture, separate function magnets (dipoles and quadrupoles). The ring is configured with FODO cells combined with DBA (Double Bend Achromat) optics. The ring layout, including pion injection/extraction points, is illustrated in Fig. 31 and the current ring design parameters are given in Table XII.   The design goal for the ring was to maximize both the transverse and momentum acceptance (around the 3.8 GeV/c central momentum), while maintaining acceptable physical apertures of the magnets. These requirements would drive the lattice design towards strongly focusing (large transverse acceptance)

Figure 31. Racetrack ring layout. Pions are injected into the ring at the Beam Combination Section (BCS). Similarly, extraction of pions and muons at the end of the production straight is done using a mirror image of the BCS.

Table XII. Decay ring specifications

Parameter	Specification	Unit
Central momentum P_μ	3.8	GeV/c
Momentum acceptance	$\pm$ 10%	
Circumference	480	m
Straight length	185	m
Arc length	50	m
Arc cell	DBA	
Ring Tunes (ν_x, ν_y)	9.72, 7.87	
Number of dipoles	16	
Number of quadrupoles	128	
Number of sextupoles	12	

and low chromaticity (large momentum acceptance) optics in the arcs. Furthermore, one side of the arc needs to accommodate pion injection/extraction sections. The stochastic injection, as described in Section II D, drives the dispersion value to about 3 m, which puts a serious limitation on the transverse acceptance. The large dispersion at the injection point must be suppressed in the arc. To accommodate this, we have used Double-Bend Achromat (DBA) optics in the arcs, which controls the beam size.

To maintain the compactness of the arc, while accommodating adequate drift space between magnets, we limit the overall arc length to about 50 m, keeping the dipole fields at $\simeq$ 4 Tesla. We use DBA optics, which maintains reasonably small values of the beta functions and dispersion. We limit the maximum field at the quadrupole magnet pole tip to be less than 5 Tesla. The overall arc optics are illustrated in Fig. 32. The decay straight requires much larger values of the beta functions ($\simeq$ 27 m average) in order to assure small beam divergence ($\simeq$ 7 mrad). The resulting muon beam divergence is a factor of 4 smaller than
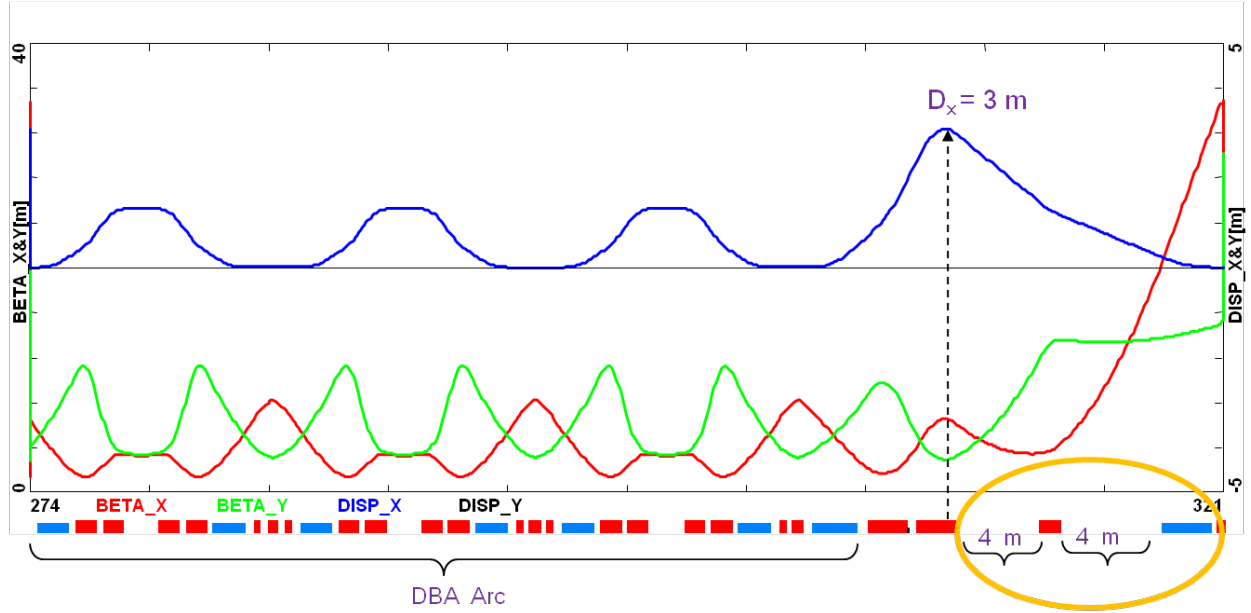
Figure 32. The arc optics illustration

the characteristic decay cone of $1/\gamma$ (0.029 at 3.8 GeV). The decay straight is configured with a much weaker focusing FODO lattice ($\simeq$ 15 deg. phase advance per cell). It uses normal conducting, 30 cm radius aperture quads with a modest gradient of 2 Tesla/m (0.6 Tesla at the pole tip).

The opposite straight, which is not used for neutrino production, can be designed with much smaller beta functions. This straight also uses normal conducting quads, but with a gradient of 11 Tesla/m (1.6 Tesla at the pole tip).

Finally, the racetrack ring optics are illustrated in Fig. 33. It features a low-beta straight matched to a 180 deg. arc and is then followed by a high-beta decay straight connected to the other arc with a compact telescope insert. The complete ring optics and the single turn beam loss histogram are shown in Fig. 34.

It is very likely that the large beam loss where the beam enters the decay ring arc is caused by beta chromaticity, or "beta beat" raised by momentum difference. It is observed in simulations that, with sextupole and octupole correction, the orbit response of off-momentum particles can be well corrected (See Fig. 35 and Fig. 36). Using particle tracking in G4beamline, we are able to achieve approximately 60% beam survival rate, for a Gaussian distributed muon beam, after 100 turns in the ring (without higher-order correc-
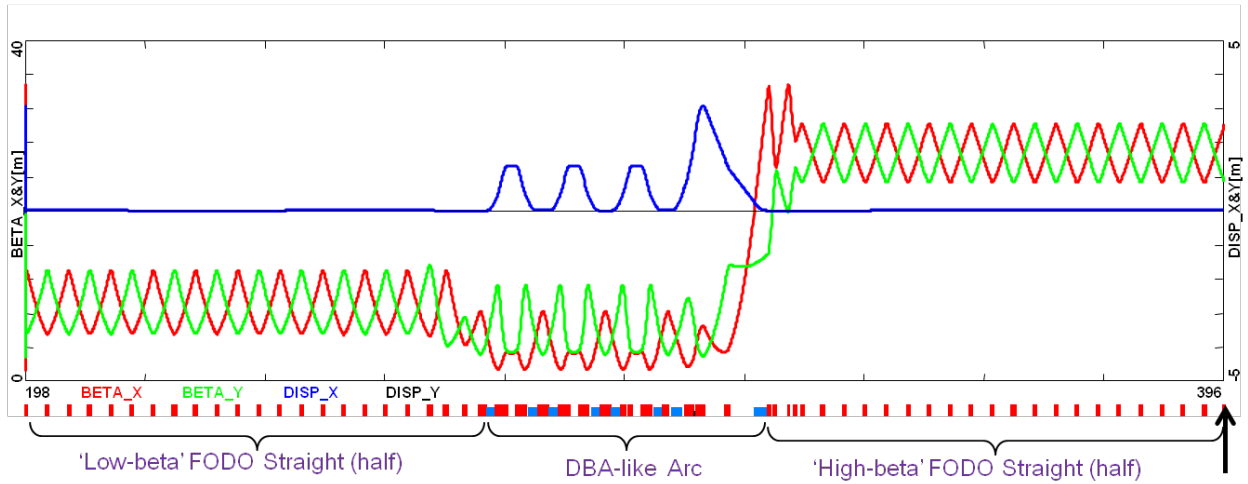
Figure 33. Ring optics.

tors). This number can be increased when further detailed corrections of tune chromaticity and beta chromaticity are developed.
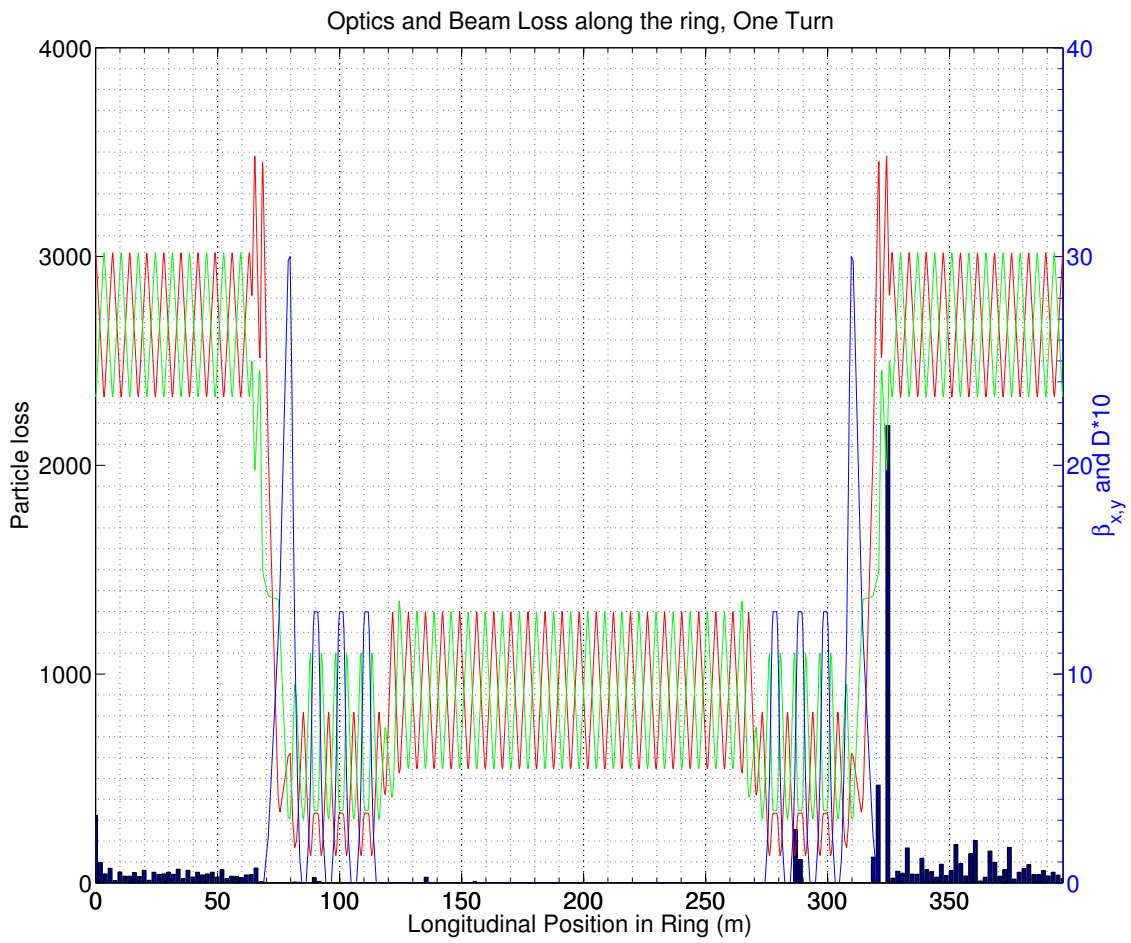
Figure 34. The complete ring optics and single-turn beam loss histogram.
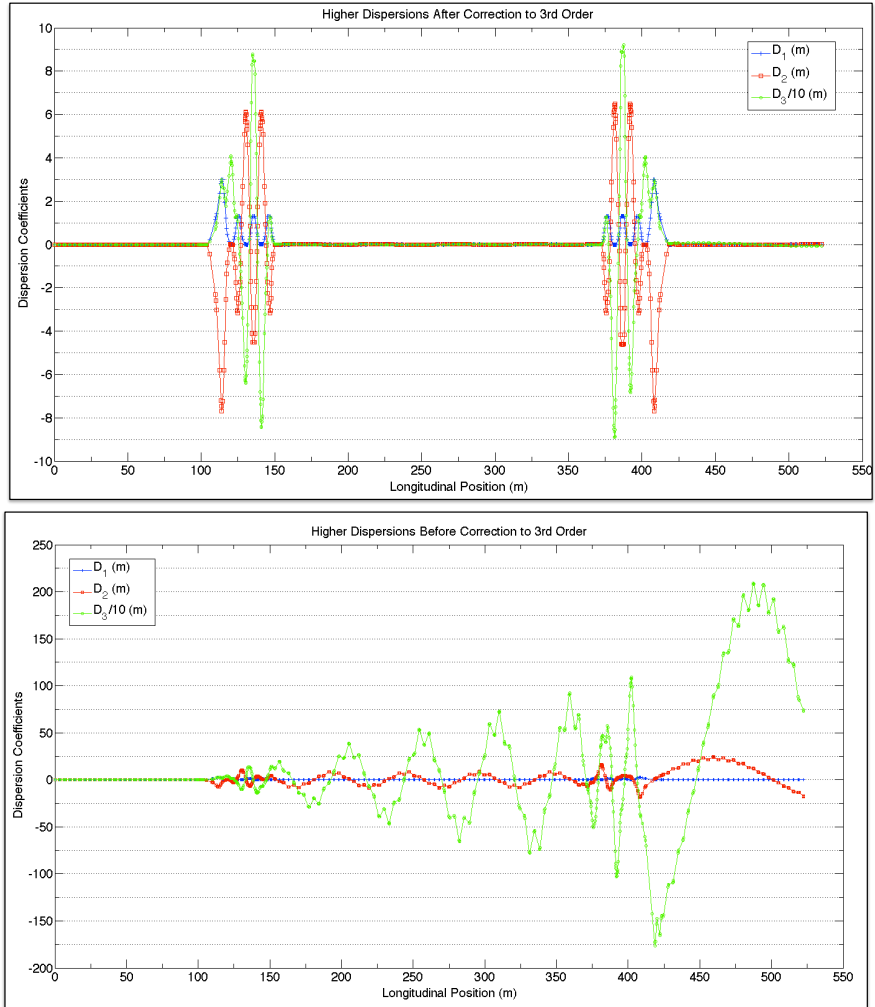
Figure 35. The higher order dispersions (up to 3rd order) before(lower) and after(upper) correction
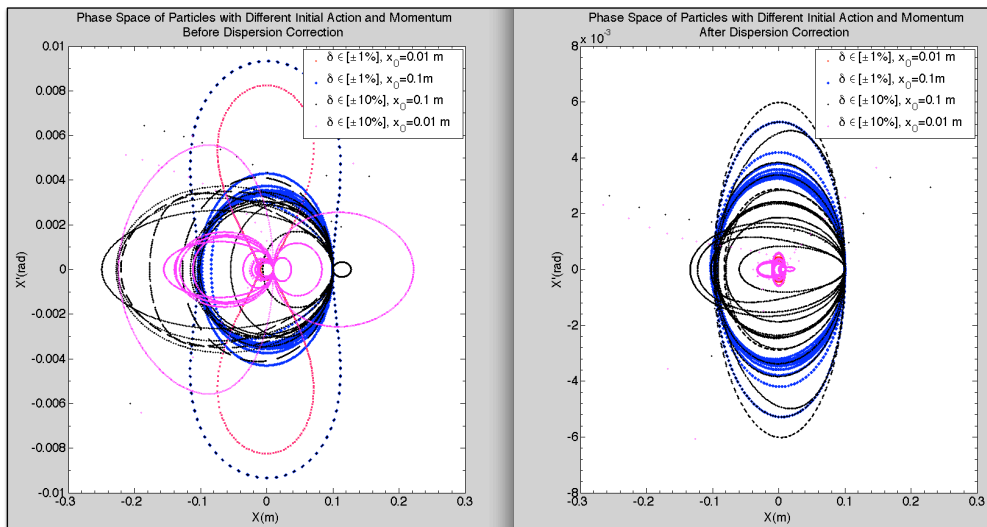
Figure 36. The 100-turn tracking for off-momentum particles before(left) and after(right) correction.

2. Advanced scaling FFAG

The racetrack FFAG ring is composed of two cell types: a) a straight scaling FFAG cell and b) a circular scaling FFAG cell. There are 40 straight FFAG cells in each long straight section (80 for the whole ring) and 16 circular FFAG cells in each of the arc sections.

a. Straight scaling FFAG cell parameters

In the straight scaling FFAG cell, the vertical magnetic field B_{sz} in the median plane follows:

$$B_{sz} = B_{0sz}e^{m(x-x_0)}\mathcal{F},$$

with x the horizontal Cartesian coordinate, m the normalized field gradient, $\mathcal{F}$ an arbitrary function and $B_{0sz} = B_{sz}(x_0)$. The parameters of the straight scaling FFAG cell are summarized in Table XIII. The cell is shown in Fig. 37. The red line represents the $\simeq 3.8$ GeV/c

Table XIII. Parameters of the straight scaling FFAG cell.

Cell type		DFD triplet
Number of cells in the ring		80
Cell length		6 m
x_0		36 m
m-value		$2.65\,\mathrm{m}^{-1}$
Packing factor		0.1
Collimators $(x_{min}, x_{max}, z_{max})$		(35.5 m, 36.5 m, 0.3 m)
Periodic cell dispersion		0.38 m
Horizontal phase advance		13.1 deg.
Vertical phase advance		16.7 deg.
D_1 magnet parameters		
	Magnet center	0.2 m
	Magnet length	0.15 m
	Fringe field fall off	Linear (Length: 0.04 m)
	$B_0(x_0 = 36\ m)$	1.28067 T
F magnet parameters		
	Magnet center	3 m
	Magnet length	0.3 m
	Fringe field fall off	Linear (Length: 0.04 m)
	$B_0(x_0 = 36\ m)$	-1.15037 T
D_2 magnet parameters		
	Magnet center	5.8 m
	Magnet length	0.15 m
	Fringe field fall off	Linear (Length: 0.04 m)
	$B_0(x_0 = 36\ m)$	1.28067 T

muon reference trajectory, and its corresponding magnetic field is shown in Fig. 38. Periodic β functions are shown in Fig. 39.
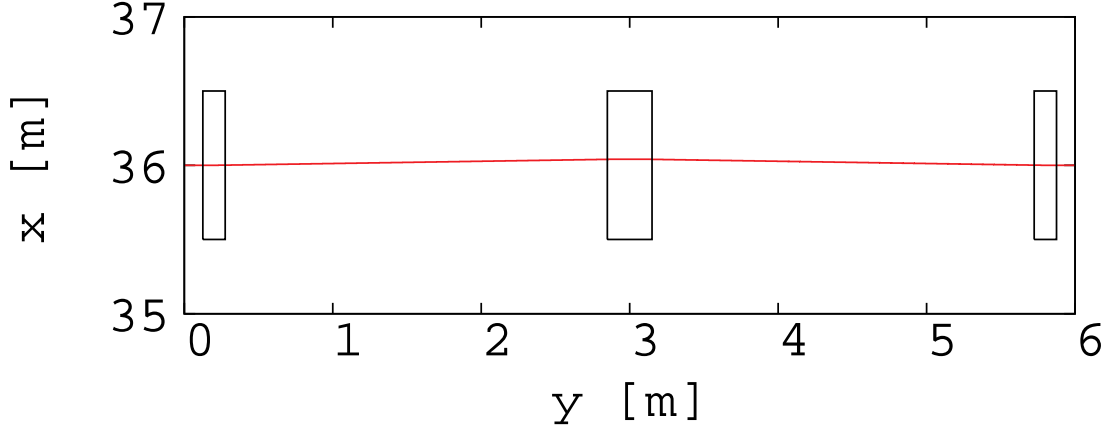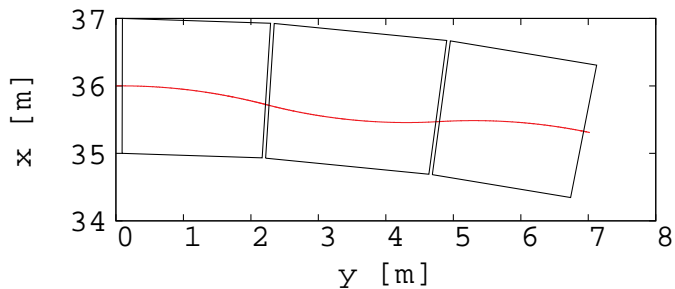

Figure 37. Top view of the straight scaling FFAG cell. The 3.8 GeV/c muon reference trajectory is shown in red. Effective field boundaries with collimators are shown in black.
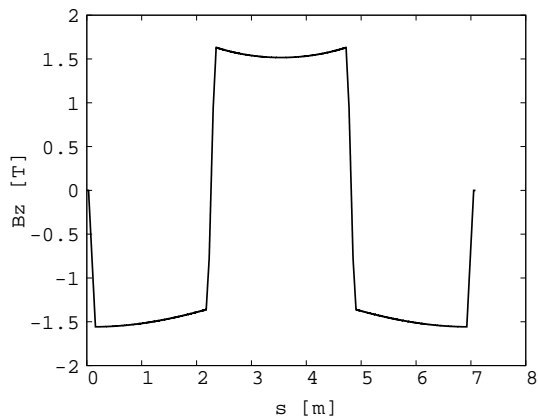
b.   Circular scaling FFAG cell parameters

In the circular scaling FFAG cell, the vertical magnetic field B_{cz} in the median plane follows

$$B_{cz} = B_{0cz} \left(\frac{r}{r_0} \right)^k \mathcal{F},$$

with r the radius in polar coordinates, k the geometrical field index, $\mathcal{F}$ an arbitrary function and $B_{0cz} = B_{cz}(r_0)$. The parameters of the circular scaling FFAG cell are summarized in Table XIV. The cell is shown in Fig. 40. The red line represents the 3.8 GeV/c muon reference trajectory, and its corresponding magnetic field is shown in Fig. 41. Periodic β functions are shown in Fig. 42.
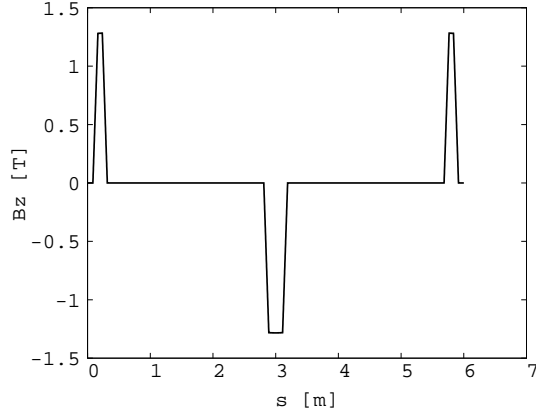
Figure 38. Vertical magnetic field for 3.8 GeV/c muon reference trajectory in the straight scaling FFAG cell.
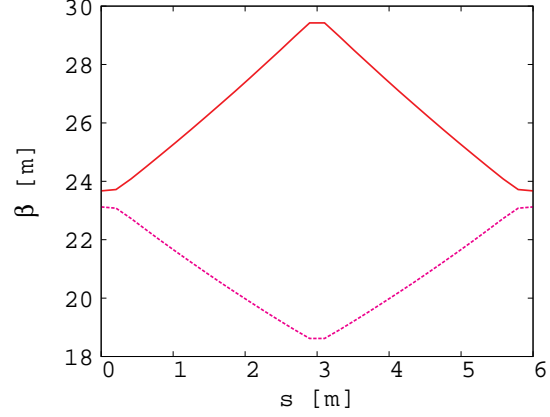
Figure 39. Horizontal (plain red) and vertical (dotted purple) periodic β functions of the straight scaling FFAG cell.

Table XIV. Parameters of the circular scaling FFAG cell.

Cell type		FDF triplet
Number of cells in the ring		32
Cell opening angle		11.25 deg
r_0		36 m
k-value		10.85
Packing factor		0.96
Collimators $(r_{min}, r_{max}, z_{max})$		(35 m, 37 m, 0.3 m)
Periodic cell dispersion		1.39 m (at 3.8 GeV/c)
Horizontal phase advance		67.5 deg.
Vertical phase advance		11.25 deg.
F_1 magnet parameters		
	Magnet center	1.85 deg
	Magnet length	3.4 deg
	Fringe field fall off	Linear (Length: 0.1 deg)
	$B_0(r_0 = 36\ m)$	-1.55684 T
D magnet parameters		
	Magnet center	5.625 deg
	Magnet length	4.0 deg
	Fringe field fall off	Linear (Length: 0.1 deg)
	$B_0(r_0 = 36\ m)$	1.91025 T
F_2 magnet parameters		
	Magnet center	9.4 deg
	Magnet length	3.4 deg
	Fringe field fall off	Linear (Length: 0.1 deg)
	$B_0(r_0 = 36\ m)$	-1.55684 T

Figure 40. Top view of the circular scaling FFAG cell. The 3.8 GeV/c muon reference trajectory is shown in red. Effective field boundaries with collimators are shown in black.

Figure 41. Vertical magnetic field for the 3.8 GeV/c muon reference trajectory in the circular scaling FFAG cell.
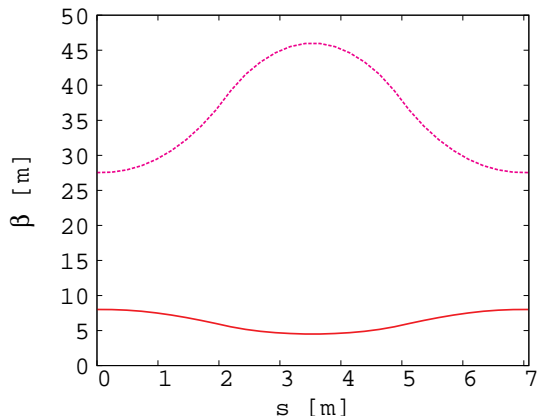
Figure 42. Horizontal (plain red) and vertical (dotted purple) periodic β functions of the circular scaling FFAG cell.

c. Single particle tracking

Stepwise tracking using Runge Kutta integration in a field model with linear fringe fields has been performed where interpolation of the magnetic field away from the mid-plane has been done to first order. Only single particle tracking has been done so far. We used μ^+ with a central momentum, p_0, of 3.8 GeV/c, a minimum momentum, p_{min}, of 3.14 GeV/c and a maximum momentum, p_{max}, of 4.41 GeV/c. $\Delta p/p_0$ is thus $\pm 16\%$. The tracking step size was 1 mm. The exit boundary of a cell is the entrance boundary of the next cell.

The ring tune point is (8.91,4.72) at the central momentum, p_0. Stability of the ring tune

has been studied over the momentum range. The tune shift is presented in Fig. 43. The tune point stays within a 0.1 shift in both planes over this momentum range.
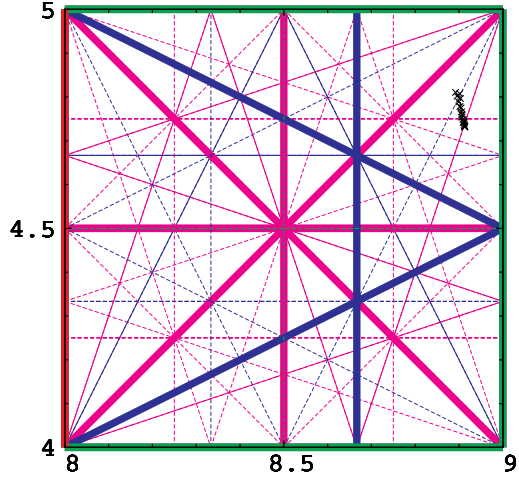
Figure 43. Tune diagram for muons from p_{min} to p_{max} ($\pm 16\%$ in momentum around 3.8 GeV/c). Integer (red), half-integer (green), third integer (blue) and fourth integer (purple) normal resonances are plotted. Structural resonances are in bold.

Closed orbits of p_0, p_{min}, and p_{max} particles are shown in Fig. 44. The magnetic field for the p_{max} closed orbit is presented in Fig. 45. Dispersion at p_0 is shown in Fig. 46. β functions for p_0, p_{min}, and p_{max} are plotted in Fig. 47.

An acceptance study at fixed energy has also been done. The maximum amplitudes with stable motion at p_0 over 30 turns are shown for horizontal and vertical motion in Fig. 48 (left) and in Fig. 49 (right), respectively. The same procedure has been done for p_{min} (see Fig. 50) and p_{max} (see Fig. 52). The results are comparable. The unnormalized maximum emittance is more than 1 mm-radian.

d.   **Multi-particle tracking**

Multi-particle beam tracking in 6-D phase space has been carried out for the beam with $\Delta p/p_0 = \pm 16\%$. Fig. 54 and 55 show the results of the beam tracking simulation in the horizontal and vertical directions, respectively. A normalized emittance of 14 mm-radian in the transverse direction is assumed. In these figures, the blue dots show the initial particle distribution and the red ones are after 60 turns. No beam loss is observed in 60 turns.
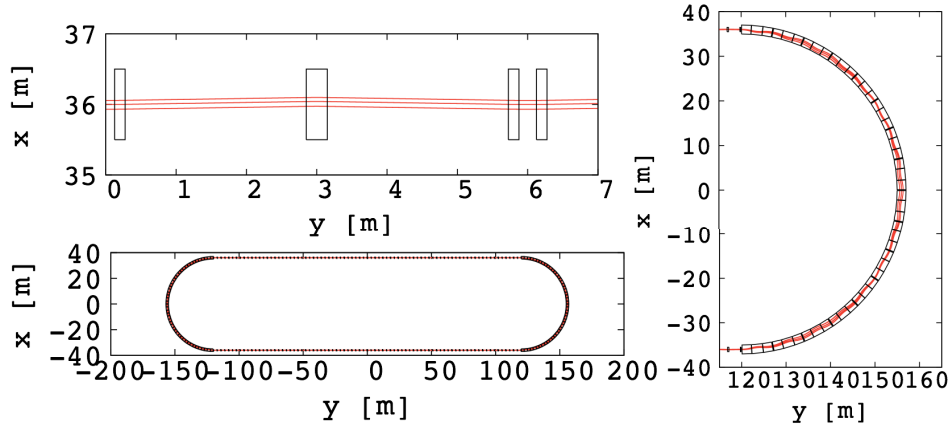
Figure 44. Top view of the racetrack FFAG lattice (bottom left scheme). The top left shows a zoom of the straight section and on the right we show a zoom of the arc section. p_0, p_{min}, and p_{max} muon closed orbits are shown in red. Effective field boundaries with collimators are shown in black.
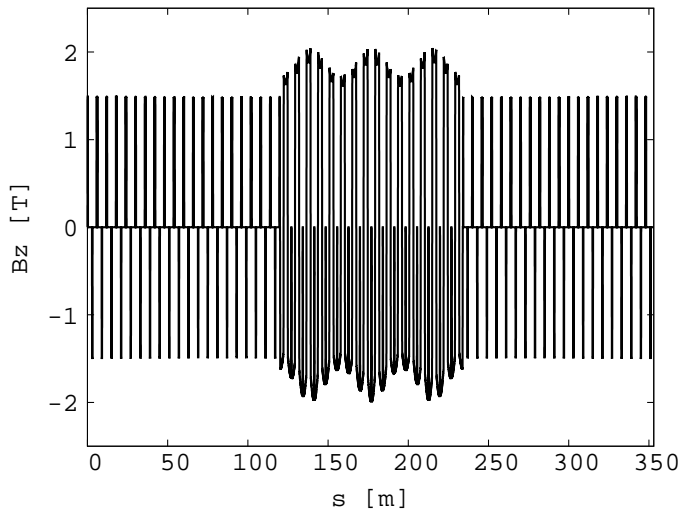
Figure 45. Vertical magnetic field for p_{max} muon closed orbit in the racetrack FFAG ring.
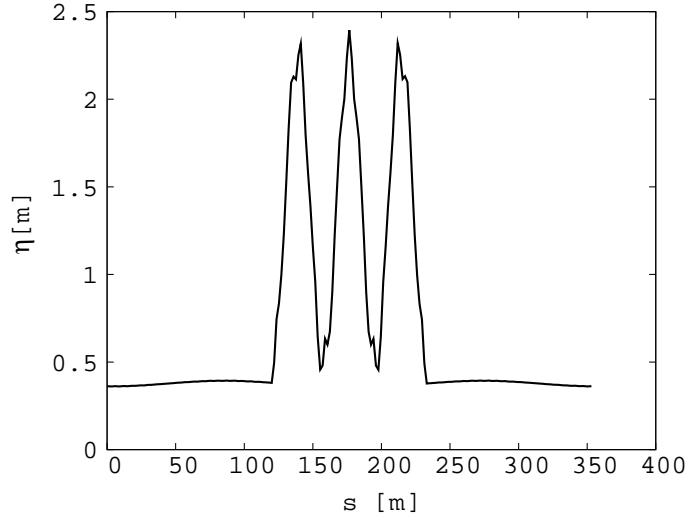
Figure 46. Dispersion function for p_0 in half of the ring. The plot is centered on the arc part.
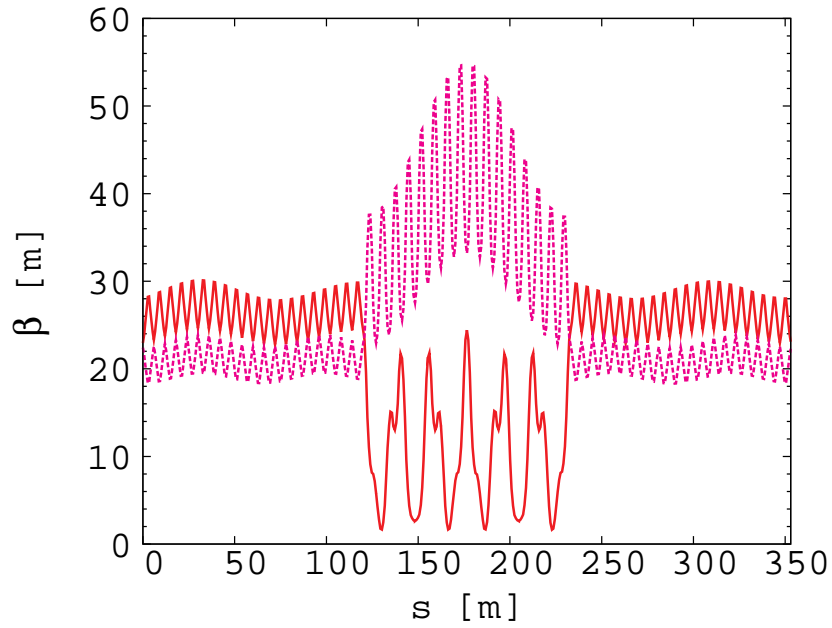
Figure 47. Horizontal (plain red) and vertical (dotted purple) periodic β functions of half of the ring for p_0. The plot is centered on the arc part.
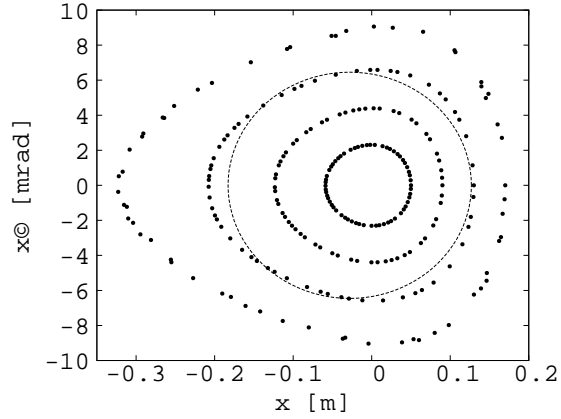
Figure 48. Stable motions in the horizontal Poincare map for different initial amplitudes (5 cm, 9 cm, 13 cm and 17 cm) over 30 turns for p_0. The ellipse shows a 1 mm-radian unnormalized emittance.
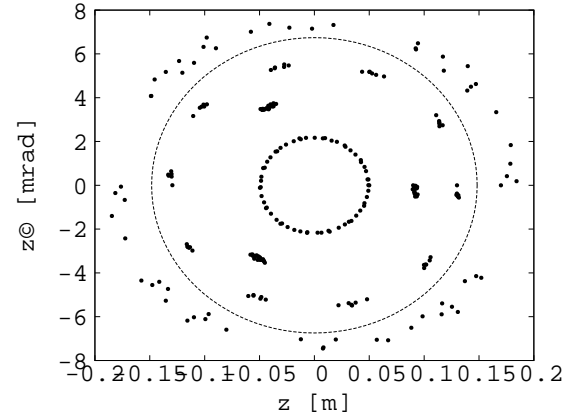
Figure 49. Stable motions in the vertical Poincare map for different initial amplitudes (5 cm, 9 cm, 13 cm and 17 cm) over 30 turns for p_0. The ellipse shows a 1 mm-radian unnormalized emittance.
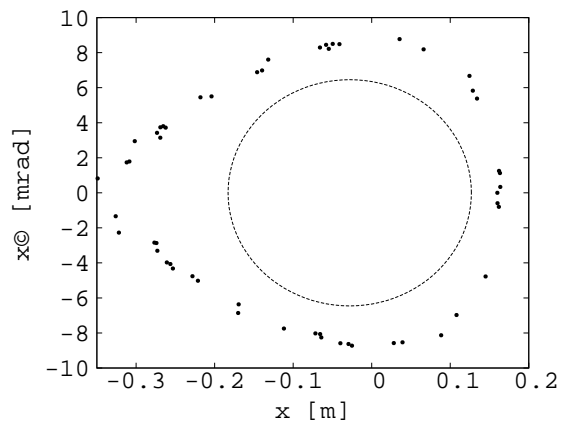
Figure 50. Horizontal Poincare map for maximum initial amplitude (16 cm) with stable motion over 30 turns for p_{min}. The ellipse shows a 1 mm-radian unnormalized emittance.
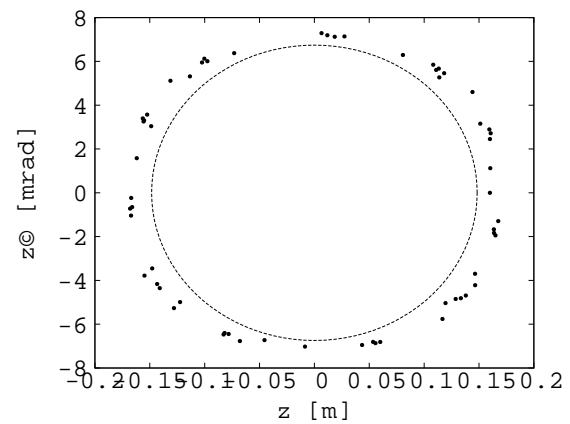

Figure 51. Vertical Poincare map for maximum initial amplitude (16 cm) with stable motion over 30 turns for p_{min}. The ellipse shows a 1 mm-radian unnormalized emittance.
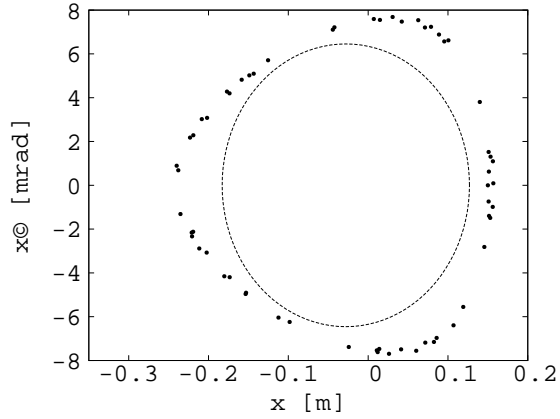
Figure 52. Horizontal Poincare map for maximum initial amplitude (15 cm) with a stable motion over 30 turns for p_{max}. The ellipse shows a 1 mm-radian unnormalized emittance.
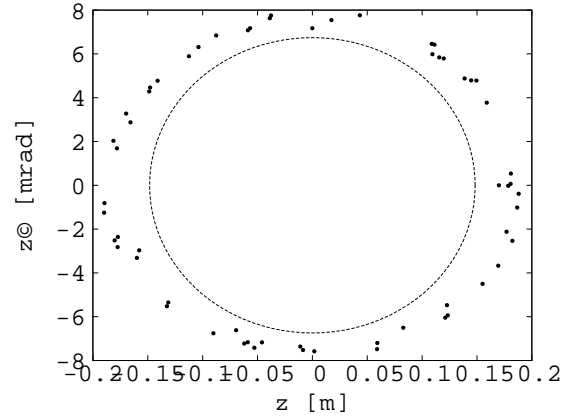
Figure 53. Vertical Poincare map for maximum initial amplitude (17 cm) with a stable motion over 30 turns for p_{max}. The ellipse shows a 1 mm-radian unnormalized emittance.
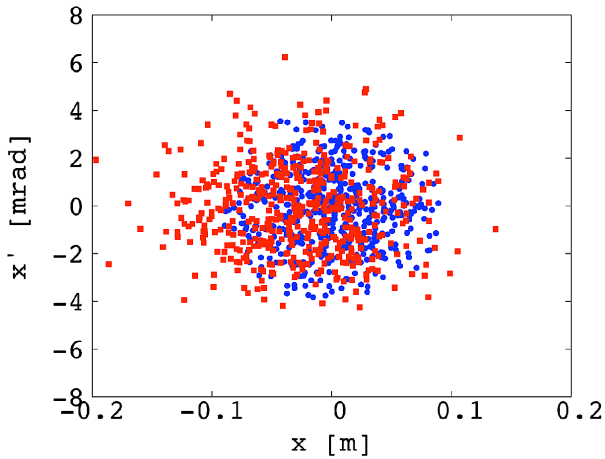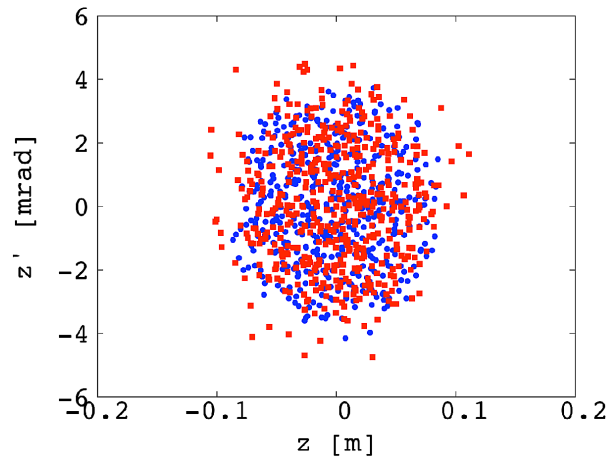

Figure 54. Beam tracking results in the horizontal phase space for a beam with $\Delta p/p_0 = \pm 16\%$. The blue shows the initial particle distribution and the red the final distribution after 60 turns.

Figure 55. Beam tracking results in the vertical phase space for a beam with $\Delta p/p_0 = \pm 16\%$. The blue shows the initial particle distribution and the red the final distribution after 60 turns.

e. Compact arc design for the racetrack FFAG ring

In order to reduce the construction and operational cost of the racetrack FFAG decay ring, a compact arc has been designed. It assumes the use of super-ferric combined-function magnets with magnetic field strengths up to 3 T. The arc consists of four regular FDF triplet cells in the centre and two matching FDF triplet cells on each side of the regular cells, four matching cells in total for the arc. The purpose of the matching section is to match the dispersion function between the production section, assuming straight FFAG cells with small, but non-zero dispersion of 0.38 m, and the centre of the arc. It must also accommodate straight sections which allow for the stochastic injection of 5 GeV/c pions. The parameters of the regular scaling FFAG arc cell are summarized in Table XV. In the circular matching scaling FFAG cell, the vertical magnetic field in the median plane follows the circular scaling law, as in the circular cell. The parameters of the matching scaling FFAG cell are summarized in Table XVI. The arc layout of the ring is shown in Fig. 56. The central orbit, p_0 (3.8 GeV/c) and the orbits for p_{min} (-16%) and p_{max} (+16%) are also shown in Fig. 56. The magnetic field for the p_{max} closed orbit is shown in Fig. 57. The dispersion at p_0 is shown in Fig. 58 and the beta-functions at p_0 in Fig. 59.
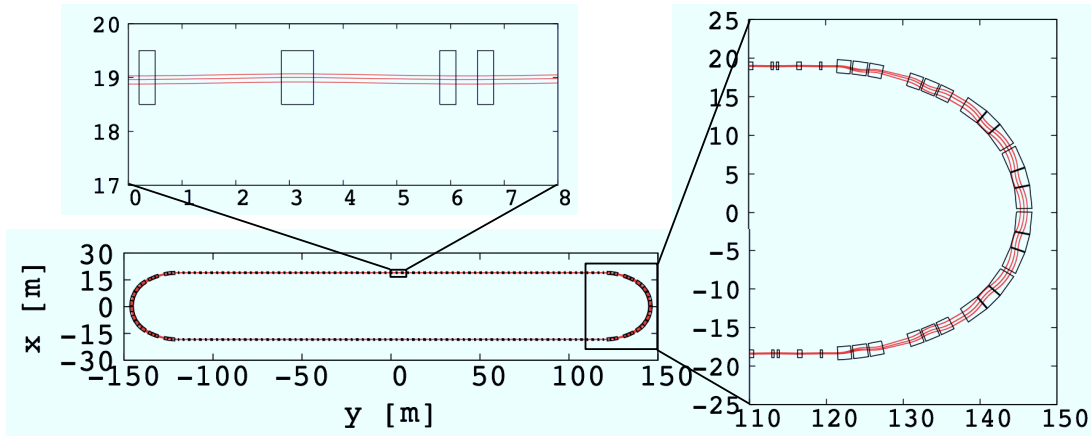

Figure 56. Top view of the racetrack FFAG lattice (bottom left figure). The top left figure shows a detail of the straight section and the right figure a detail of the arc. Muon closed orbits for p_0, p_{min}, and p_{max} are shown in red. Effective field boundaries with collimators are shown in black.

Future studies on the racetrack FFAG decay ring will include a ring reconfiguration to adjust the ratio of the production straight and the arc length, detailed optimization of the

Table XV. Parameters of the circular regular scaling FFAG arc cell.

Cell type		FDF triplet
Number of cells in the ring		8
Cell opening angle		30 deg
r_0		16 m
k-value		6.25
Packing factor		0.92
Collimators $(r_{min}, r_{max}, z_{max})$		(15 m, 17 m, 0.4 m)
Periodic cell dispersion		2.21 m (at 3.8 GeV/c)
Horizontal phase advance		90 deg.
Vertical phase advance		13.92 deg.
F_1 magnet parameters		
	Magnet center	5.8 deg
	Magnet length	10 deg
	Fringe field fall off	Linear (Length: 0.7 deg)
	$B_0(r_0 = 16\ m)$	-1.70382 T
D magnet parameters		
	Magnet center	15 deg
	Magnet length	7.6 deg
	Fringe field fall off	Linear (Length: 0.7 deg)
	$B_0(r_0 = 16\ m)$	2.13119 T
F_2 magnet parameters		
	Magnet center	24.2 deg
	Magnet length	10 deg
	Fringe field fall off	Linear (Length: 0.7 deg)
	$B_0(r_0 = 16\ m)$	-1.70382 T

working point and tracking studies. In addition, the detailed geometry of the pion injection together with the design of the super-ferric magnets must also be addressed.

Table XVI. Parameters of the matching scaling FFAG cell.

Cell type		FDF triplet
Number of cells in the ring		8
Cell opening angle		15 deg
r_0		36.15 m
k-value		26.98
Packing factor		0.58
Collimators $(r_{min}, r_{max}, z_{max})$		(35.3 m, 37 m, 0.4 m)
Periodic cell dispersion		1.29 m (at 3.8 GeV/c)
Horizontal phase advance		90 deg.
Vertical phase advance		16.95 deg.
F_1 magnet parameters		
	Magnet center	4.2 deg
	Magnet length	2.8 deg
	Fringe field fall off	Linear (Length: 0.7 deg)
	$B_0(r_0 = 36.15\ m)$	-2.18805 T
D magnet parameters		
	Magnet center	7.5 deg
	Magnet length	3.0 deg
	Fringe field fall off	Linear (Length: 0.7 deg)
	$B_0(r_0 = 36.15\ m)$	2.74622 T
F_2 magnet parameters		
	Magnet center	10.8 deg
	Magnet length	2.8 deg
	Fringe field fall off	Linear (Length: 0.7 deg)
	$B_0(r_0 = 36.15\ m)$	-2.18805 T
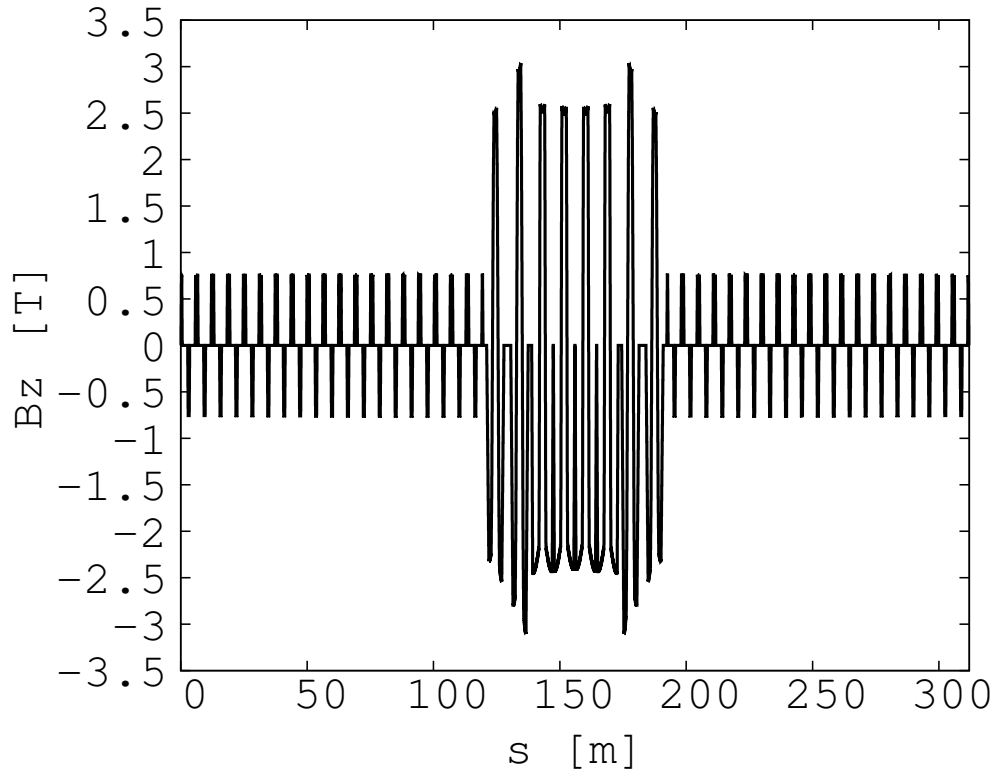
Figure 57. Vertical magnetic field for the muon closed orbit at p_{max} in the racetrack FFAG ring.
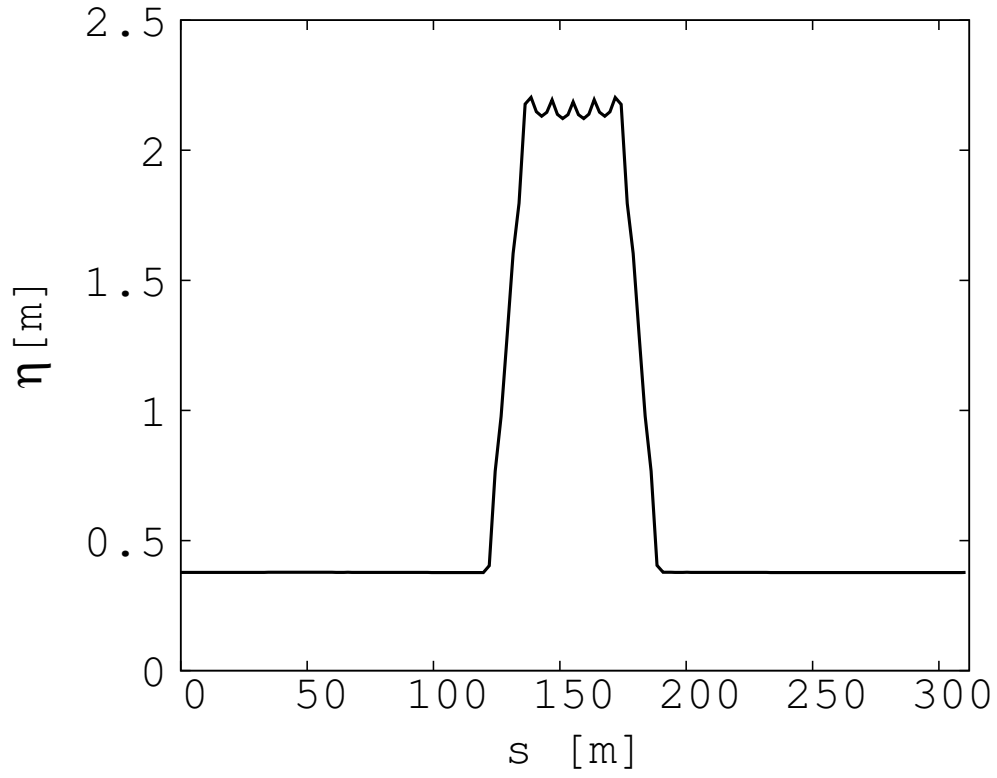
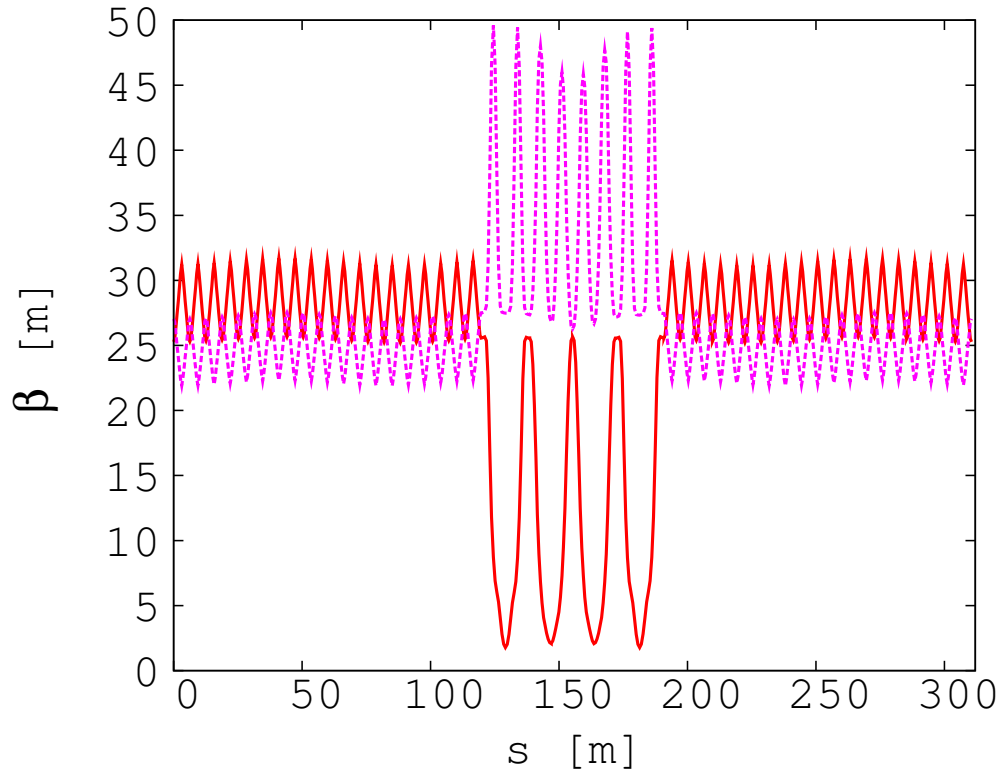Figure 58. Dispersion function for p_0 in half of the ring. The plot is centered on the arc.

Figure 59. Horizontal (plain red) and vertical (dotted purple) periodic beta-functions of half of the ring for p_0. The plot is centered on the arc.

3. Decay ring instrumentation

The goal of the beam instrumentation for nuSTORM is twofold. First, the instrumentation is needed in order to determine the neutrino flux at the near and far detectors with an absolute precision of $< 1\%$. Both the number of neutrinos and their energy distribution must be determined. If both the circulating muon flux in the storage ring is known on a turn-to-turn basis, and the orbit and orbit uncertainties (uncertainty on the divergence) are known accurately, then the neutrino flux and energy spectrum can be predicted with equal precision. Our measurement goals for the suite of beam instrumentation diagnostics for the decay ring are summarized below:

1. Measure the circulating muon intensity (on a turn by turn basis) to 0.1% absolute.

2. Measure the mean momentum to 0.1% absolute.

3. Measure the momentum spread to 1% (FWHM).

4. Measure the tune to 0.01.

Second, from the accelerator standpoint, in order to commission and run the storage ring, turn-by-turn measurements of the following parameters are crucial: trajectory, tune, beam profile and beam loss. Our current estimate of these requirements is summarized in Table XVII below.

Table XVII. Decay ring instrumentation specifications

	Absolute accuracy	Resolution
Intensity	0.1%	0.01%
Beam position	5 mm	1 mm
Beam profile	5 mm	1 mm
Tune	0.01	0.001
Beam loss	1%	0.5%
Energy	0.5%	0.1%
Energy spread	1%	0.1%

a. Beam intensity

In order to measure the circulating muon intensities, one option is to use a toroid-based Fast Beam Current Transformer (FBCT), such as the one recently developed at CERN for L4 [42]and shown in Fig. 60. Its specifications are given in Table XVIII. It consists of a one turn calibration winding and a 20 turn secondary winding, wound on a magnetic core and housed in a 4 layer shielding box. The mechanical dimensions will have to be adapted to the large beam pipe of nuSTORM. It should be noted that obtaining an absolute precision of 0.1% will be challenging. Problems associated with the pulsed calibration and with EMI will influence the absolute accuracy of the FBCT.
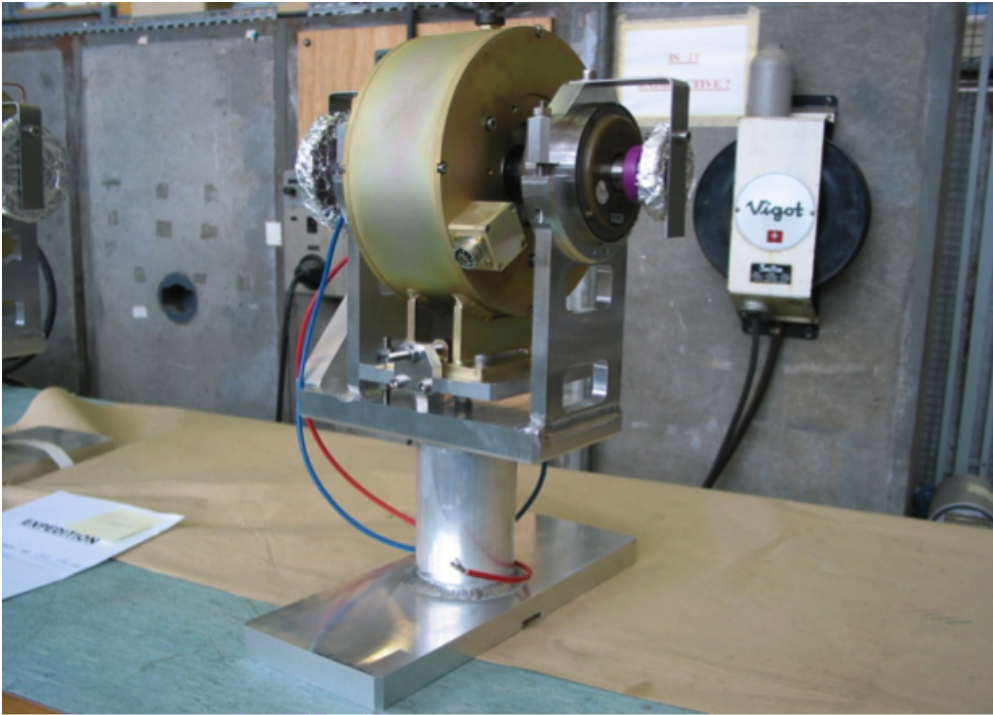
Figure 60. CERN L4 beam current transformer

Table XVIII. FBCT parameters

Droop @ 500 μs	0.5%
Bandwidth	10 MHz
Accuracy	$\simeq 1\%$
Resolution	$\simeq 10\mu$A
Rise time	35 ns

b. Beam position

Button beam-position monitors (BPMs) are, in general, cheap and their frequency response fits very well with that of nuSTORM. They are widely used in the LHC. A photo of the 25mm diameter button is shown in Fig. 61. Due to the large vacuum chamber size and
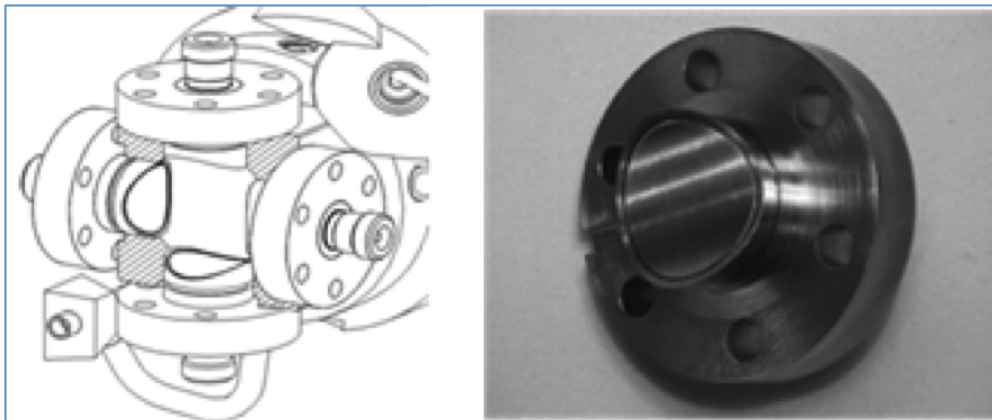

Figure 61. LHC beam-position monitor button

the, at present, uncertainties regarding the circulating beam parameters, it is difficult to estimate the ultimate resolution which can be obtained. However, we can estimate the resolution assuming the following: a 100mm diameter button, bunch length of 4 ns, bunch intensity of 5×10^8 and an input noise of $2nV/\sqrt{Hz}$. With these assumptions, the expected electrode signal can be simulated and is shown in Fig. 62. As a first order approximation the 15mV peak amplitude on the button corresponds to 50V/mm in a 600mm diameter vacuum chamber. With the assumed bandwidth and noise of the system (output noise $\sim 30\mu$V), the expected resolution is on the order of 5 mm with a signal to noise ratio of 10. This single bunch, single turn resolution can of course be improved by averaging over all bunches, i.e., by a factor of up to 10.

c. Transverse profile measurements

Due to the relatively low intensities (compared to primary or secondary beamlines) and very short lifetime (100μs), our first estimations indicate that using Ionization Profile Monitors (IPM) to measure the transverse profiles is not feasible. Other detectors based on ionization (MWPC, IC, GEM) are destructive and would require a quite complicated design. (The use of low-mass MWPC is possible with further study, however.) The use of wire
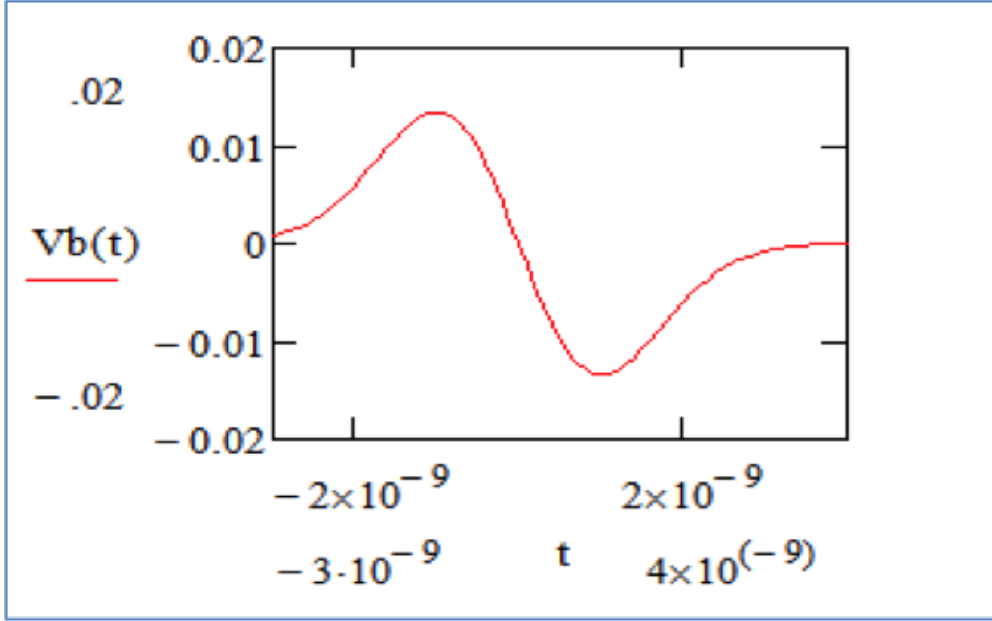
Figure 62. Button impulse response

scanners is not possible due to the short beam lifetime.

Destructive measurement techniques using either scintillation screens or SEM-strips can be utilized. One option is to adapt the LHC dump line BTV to nuSTORM. The BTV consists of a 2 m long by 60 cm diameter vacuum tank (see Fig. 63). In this design, the fixed scintillation screen is observed with a camera, which is read out using a VME based control and data acquisition card. We estimate that this system could provide an overall position accuracy of $\sim$ 2 mm in the nuSTORM decay ring. As designed for the LHC dump line, the system can only be used for diagnostics. It would have to be taken out of the beam during running due to the mass of the screen. However, investigating whether a low-mass screen option is possible is worth further study. The specification on the maximum tolerable material budget in the screen can be determined once we have the decay ring lattice fixed and have circulating beam in our G4Beamline simulation.

d. Tune measurements

For the measurement of the non-integer part of the nuSTORM tune we propose to use the Direct Diode Detection Base-Band Q (3D-BBQ) developed at CERN by M. Gasior [43] and shown schematically in Fig. 64. This very sensitive method allows for the observation of very small amplitude modulations on high level signals. The pulses obtained from any of the
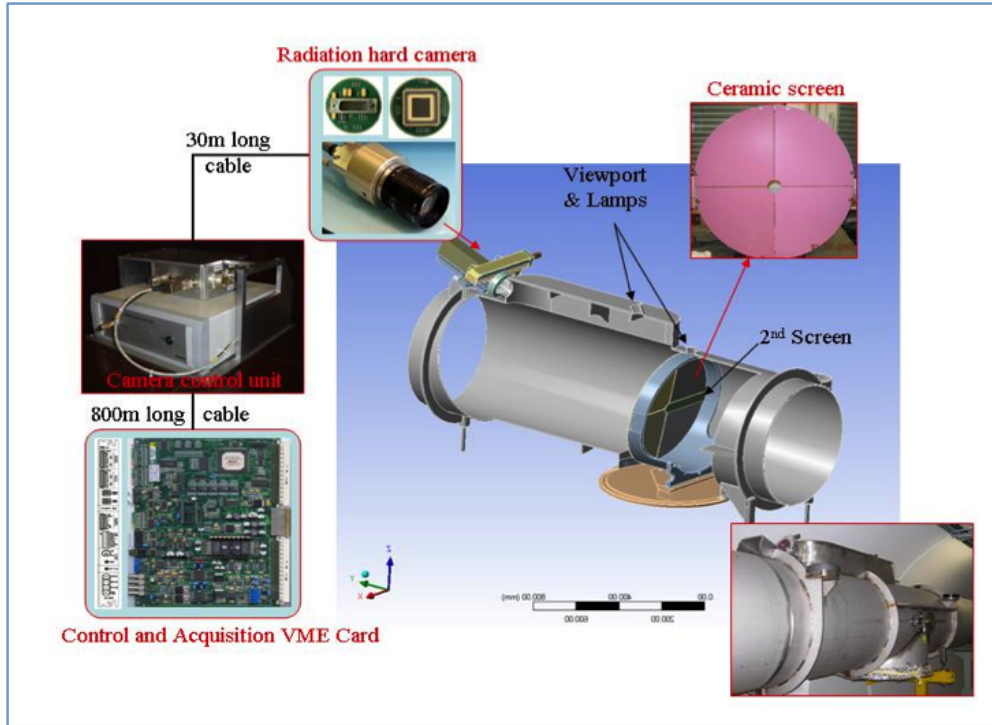
69

Figure 63. LHC dump line BTV

beam position monitors are connected to simple diode detectors which convert the amplitude modulation of the BPM pulses to a signal in the audio frequency range. The dominate part of the BPM signal is related to the beam intensity, and becomes a DC voltage. This DC component is easily removed using a simple capacitor at the detector output. The two base band signals are then subtracted in a difference amplifier and digitized for tune calculations in the frequency domain.

Due to our uncertainty on the bunch intensities at this time, it is, at present, difficult to estimate if a tune kicker is needed to enhance the betatron amplitudes to obtain the required tune and time resolution. At first estimate, we believe that connecting one or several BPMs to the system should be sufficient.

e.   **Beam loss measurements**

Beam loss monitors would be used mostly for diagnosing the performance of the ring with emphasis on the injection point using some monitors in the straight sections and in the arcs. We propose to use "slow" ionisation chambers (Fig. 65) for integration of the total loss around the ring and diamond-based fast secondary emission monitors (Fig. 66) for
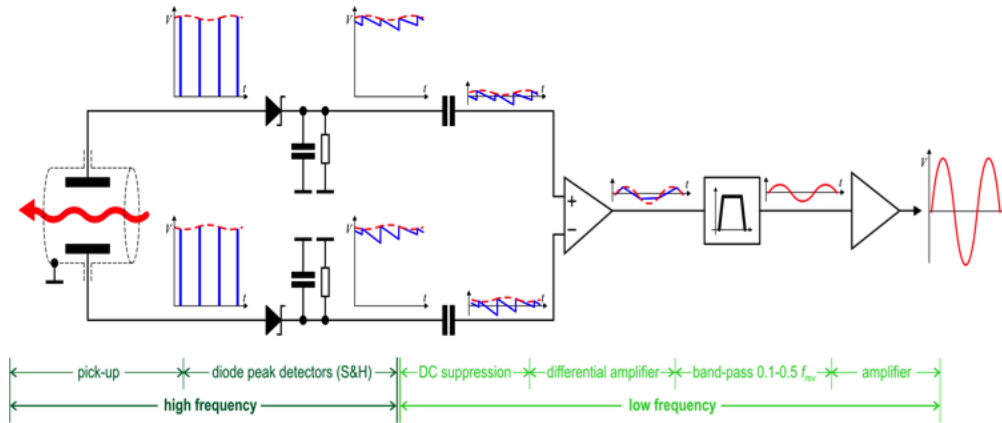
70

Figure 64. Base-band tune measurement principle

observation of the "fast" injection losses. Both types of detectors are sensitive to charged particles only.

The ionization chamber consists of a 60 cm long stainless steel cylinder, with parallel Al electrodes separated by 0.5 cm to which a voltage of 1.5 kV is applied to every second electrode. The entire volume is filled with Nitrogen gas. The output current from the grounded electrodes is then proportional to the beam loss. The diamond detector consists
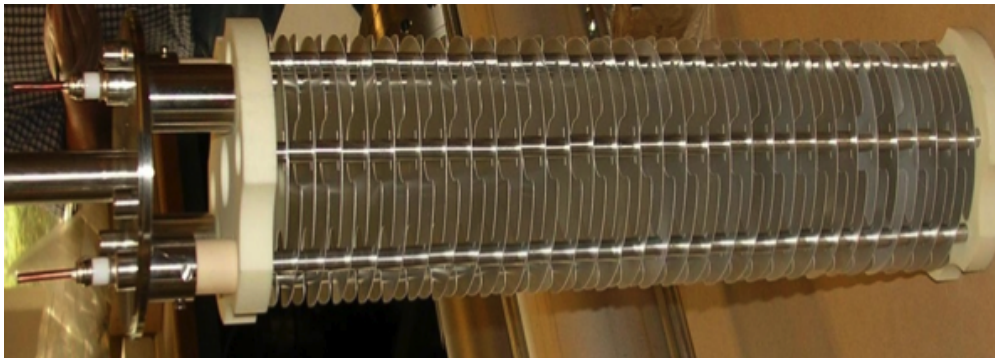

Figure 65. Photograph of an ionization chamber for total beam loss (slow) measurements

of a 10 mm × 10 mm × 0.5 mm polycrystalline chemical vapor deposition (pCVD) diamond substrate coated on each side with 200 nm thick gold electrodes. A biasing voltage of ∼ 500 V is used. A 40 dB broadband radiation hard current amplifier with a bandwidth 100 MHz to 2 GHz is needed to amplify the very low currents.

71

Figure 66. Diamond-based secondary emission monitor

f. Summary

In the above sections, we have shown how existing beam instrumentation or extrapolations from existing designs can meet the needs of nuSTORM and gives the basis for making realistic cost estimates for the instrumentation. However, obtaining full knowledge regarding how well the instrumentation will perform in the nuSTORM decay ring will only come after the lattice design is finalized (addition of higher-order correctors). Once this has been accomplished, we then have the tools in place within the G4Beamline simulation framework to understand, in detail, how this instrumentation will perform.

F.   A future 6D muon ionization cooling experiment

Fig. 67 shows a schematic of the decay ring. As is described in section II D, $5\,\mathrm{GeV/c}$ pions are injected at the beginning of the straight section of the ring. With the $185\,\mathrm{m}$ length for the straight, $\sim 48\%$ of the pions decay in the injection straight. Since the arcs are set for the central muon momentum of $3.8\,\mathrm{GeV/c}$, the pions remaining at the end of the straight will not be transported by the arc. The power contained within the pion beam that reaches the end of the injection straight is $2\,\mathrm{kW}$–$3\,\mathrm{kW}$ making it necessary to guide the undecayed pion beam into an appropriate absorber.
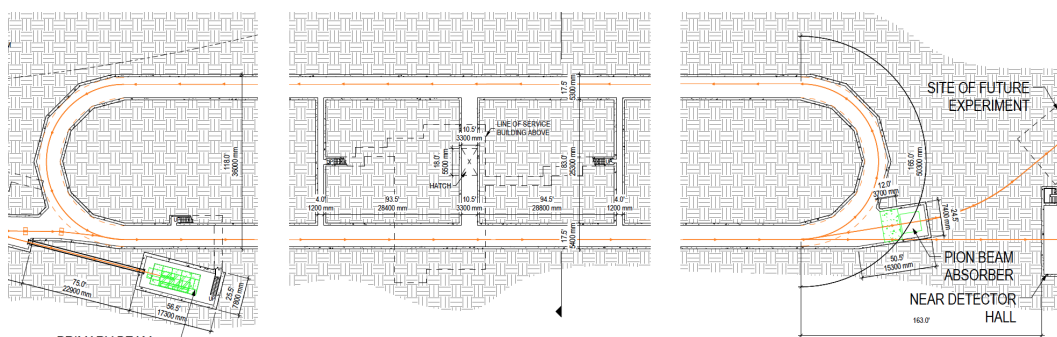
Figure 67. Schematic of the nuSTORM decay ring.

As discussed earlier, another BCS, which is just a mirror reflection of the injection BCS, is placed at the end of the decay straight. It extracts the residual pions and muons which are in the 5 ± 0.5 GeV/c momentum range. These extracted muons will enter the absorber along with pions in this same momentum band.

However, if the absorber is "redefined" to be a "degrader" capable of stopping the pions but allowing muons above a certain energy to pass, then a low-energy muon beam appropriate for a 6D muon cooling experiment can be produced. The left panel of Fig. 68 shows the momentum distribution for the first pass of muons at the end of the decay-ring straight. The green band indicates the momentum acceptance of the decay ring. The red band covers the same momentum band as the input pions and these muons will be extracted along with the remaining pions. If the degrader is sized appropriately, a muon beam of the desired momentum for a 6D cooling experiment will emerge downstream of the degrader. The right panel of Fig. 68 shows a visualization of a G4Beamline [38] simulation of the muons in the pion momentum band ($5 \pm 10\%\,\mathrm{GeV/c}$) propagating through a $3.48\,\mathrm{m}$ thick
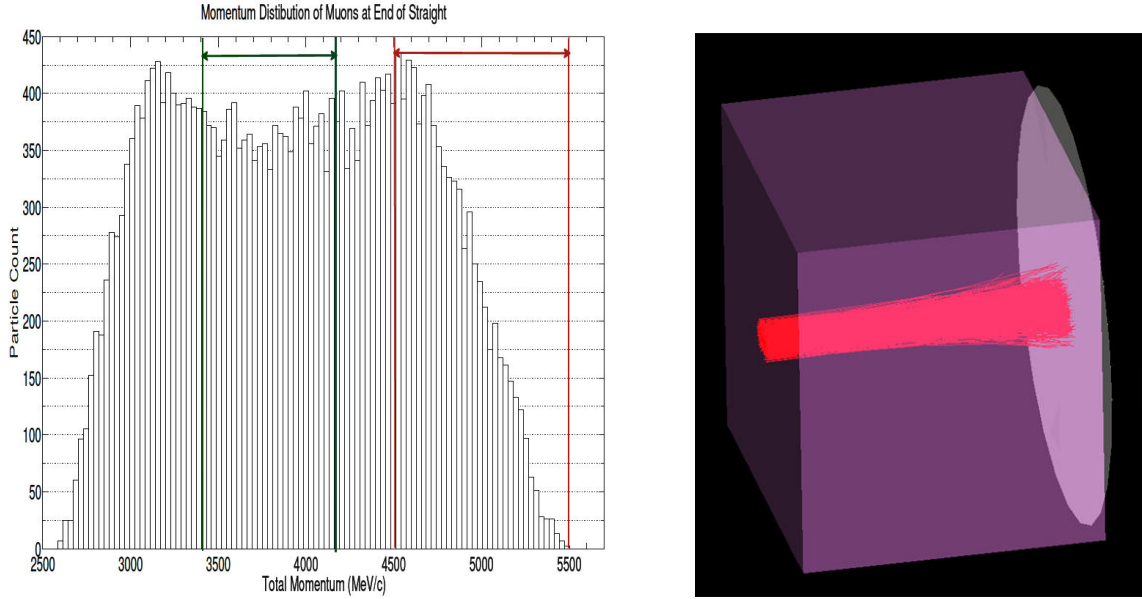
Figure 68. Left panel: Momentum distribution of muons after the first straight. Right panel: Visualization of muons in the degrader.

iron degrader. The left panel of Fig. 69 shows the $x - y$ distribution of the muon beam exiting the degrader while the right panel shows the $x - x'$ distribution. Figure 70 shows the muon momentum distribution of the muons that exit the degrader. Our initial estimate is that, in the momentum band of interest for a six-dimensional (6D) cooling experiment (100–300 MeV/c), we will have approximately 10^{10} muons in the 1.6μsec spill.

Advanced R&D on the high intensity 6D ionization cooling channel required for a Muon Collider could be pursued using the nuSTORM facility and this muon beam. The two key 6D cooling channels currently under detailed study can be tested at the nuSTORM facility without affecting the main neutrino activities: the Guggenheim and the Helical Cooling Channel (layouts in Fig. 71–72). After selection of one of these cooling schemes and a successful bench test, the hardware for the section of the cooling channel long enough to demonstrate 6D cooling could be set up at the nuSTORM facility in order to run a test demonstration experiment with the intense muon beam. Preliminary studies with one and two cells of both the initial (with 201 MHz RF) and the final (with 805 MHz RF) stages of the Guggenheim cooling channel suggest promising muon transmission rates. These are summarized in Table XIX. The corresponding momentum distribution and phase portraits are shown in Fig. 73.
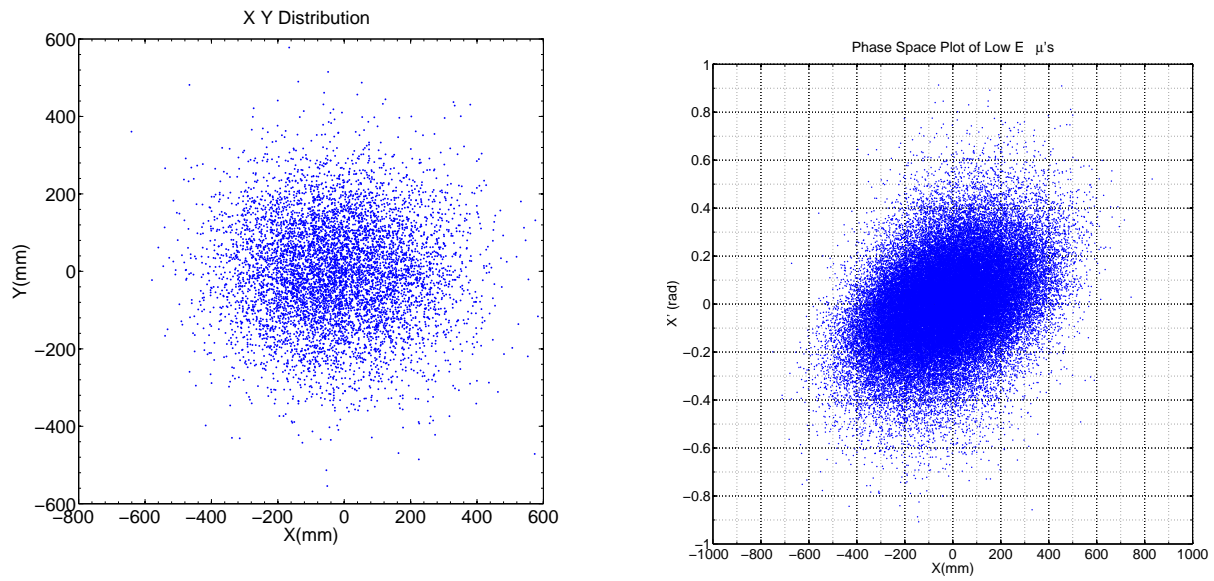
Figure 69. Phase-space of the muon beam as it leaves the degrader. Left panel: $x - y$ distribution; Right panel: $x - x'$ distribution.
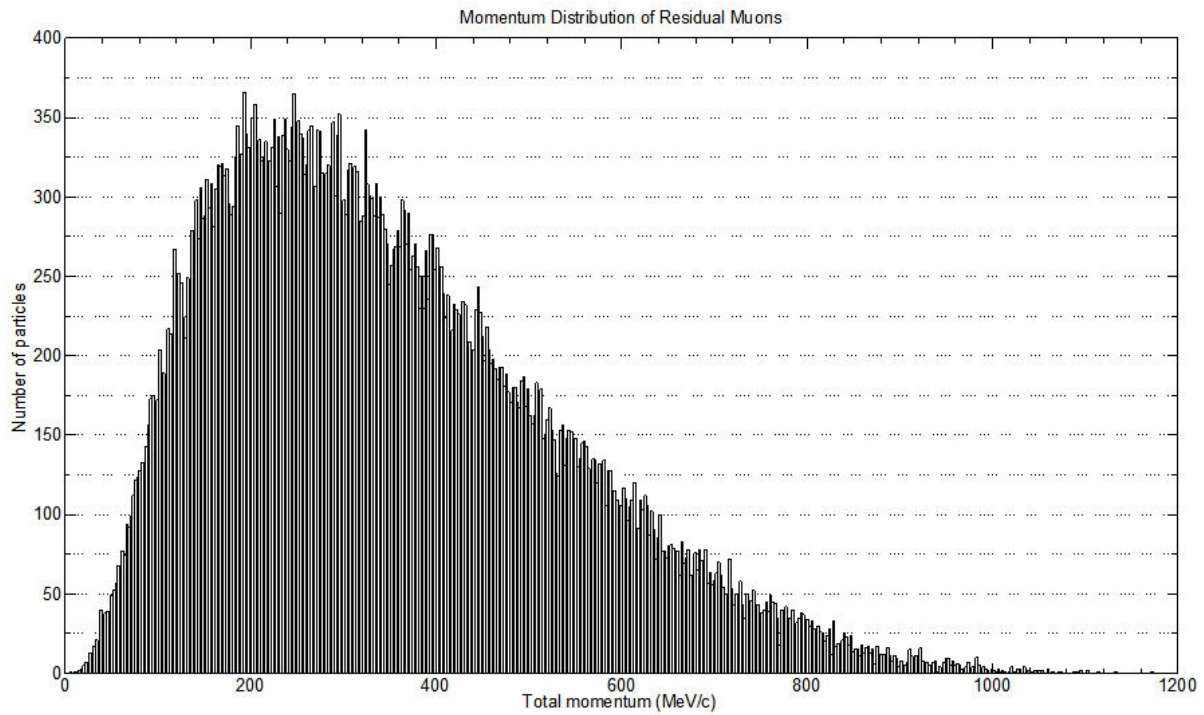

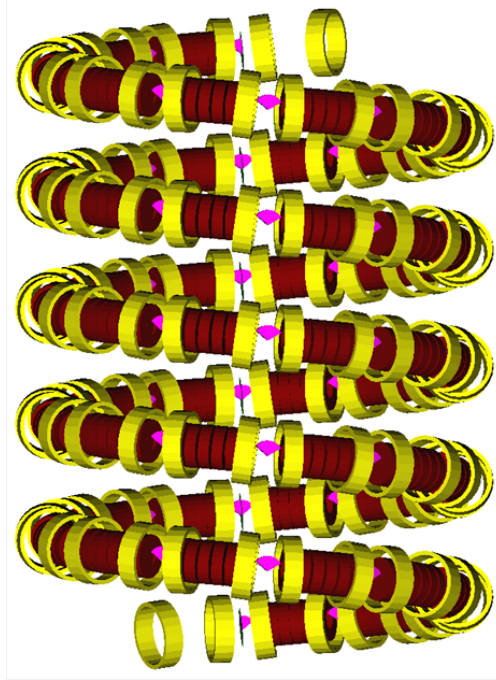Figure 70. Muon momentum distribution after degrader.

Figure 71. Layout of the initial stages of the Guggenheim cooling channel. Yellow: magnetic coils to generate focusing and bending field required for emittance exchange; magenta: liquid Hydrogen wedge absorbers to reduce momentum; red: RF cavities to restore momentum lost in the absorbers.
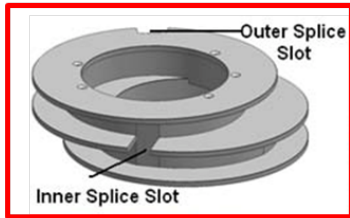
Table XIX. Percentage of muons surviving one and two cells of the 201 MHz and 805 MHz Guggenheim channel, and its dependence on the degrader length.

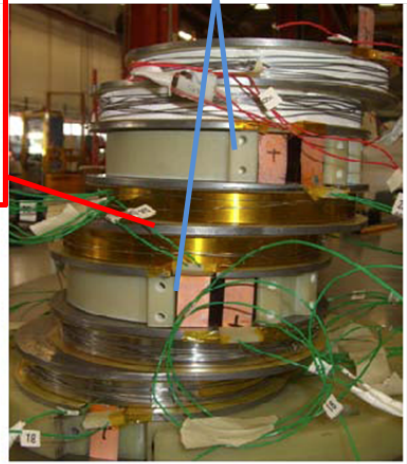| Degrader [mm]	201 MHz, one cell	201 MHz, two cells	805 MHz, one cell	805 MHz, two cells
3500	24%	8.6%	4.7%	0.6%
3480	24%	8.5%	4.9%	0.6%
3460	24%	8.4%	5.1%	0.6%
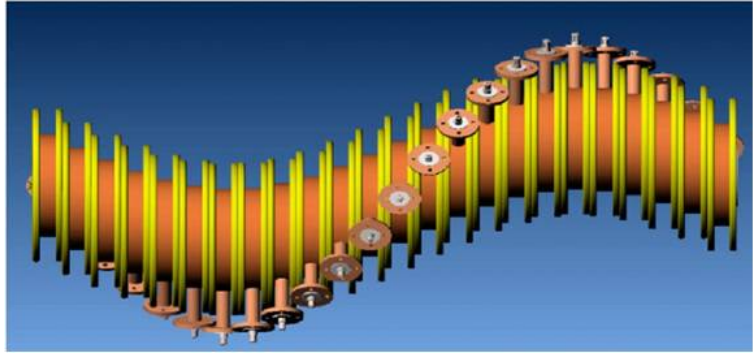
Figure 72. Top: conceptual drawing of the Helical Cooling Channel; bottom: test coil assembly producing helical solenoid field.
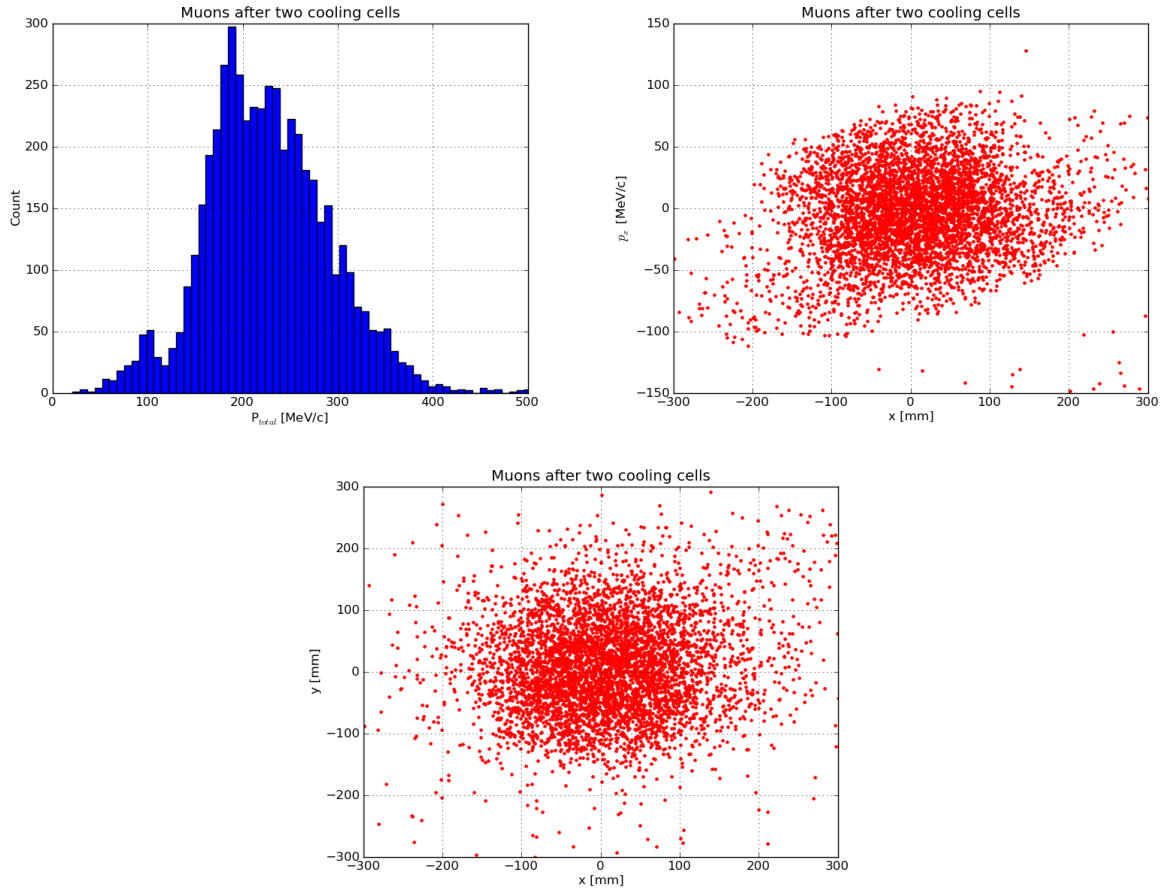
Figure 73. Top-left: muon momentum distribution after passing through two cells of the initial 201 MHz Guggenheim cooling channel; Top-right: $(x - p_x)$ phase portrait of the distribution; bottom: $(x - y)$ phase portrait of the distribution.

III. NUSTORM CONVENTIONAL FACILITIES

The nuSTORM Conventional Facilities are anticipated to consist of six (6) functional areas consisting of the Primary Beamline, Target Station, Transport Line/Muon Decay Ring, Near Detector Hall, Far Detector Hall and the Site Work.

The facilities will be located in an area south of the existing Main Injector accelerator and west of Kautz Road on the Fermilab site. In general terms, a proton beam will be extracted from the existing Main Injector at the MI-40 absorber, directed east towards a new below grade target station, pion transport line and muon decay ring. The neutrino beam will be directed towards a Near Detector Hall located 20 m East of the muon decay ring and towards the Far Detector located approximately 1900 m away in the existing D0 Assembly Building (DAB). Fig. 74, below, shows a site photo with the nuSTORM Conventional Facilities superimposed. We have also considered an East site for nuSTORM which would put all of

Figure 74. Fermilab site view looking North and showing the nuSTORM facilities.

the facility East of Kautz Road. This eliminated any potential interference with existing infrastructure near the main site, in the event there would be significant future expansions to the nuSTORM facility (see Fig. 75), but requires a long ($\simeq 510$ m) primary proton beam line from the Main Injector. The current West site does not impact existing infrastructure, while still allowing for future expansion. Full details of the nuSTORM Conventional Facilities are given in the nuSTORM project definition report [44]. DAB provides an ideal space for location of the far detector(s) for the short-baseline oscillation program. With relatively

Figure 75. Fermilab site view looking North and showing the nuSTORM facilities at the East site.

minor retro-fitting, the DAB pit area can accommodate a 1.3 kT Fe-scintillator detector (SuperBIND, see Section **??**) while providing enough space for a future kT-scale magnetized LAr detector. Fig. 76 shows a 3D view of the setup in DAB indicating the positions of SuperBIND (left) and a conceptualized LAr detector set next to the D0 experimental hall. The height of the area allows approximately 6' of heavy concrete overburden below the crane (indicated in the figure above the SuperBIND detector).
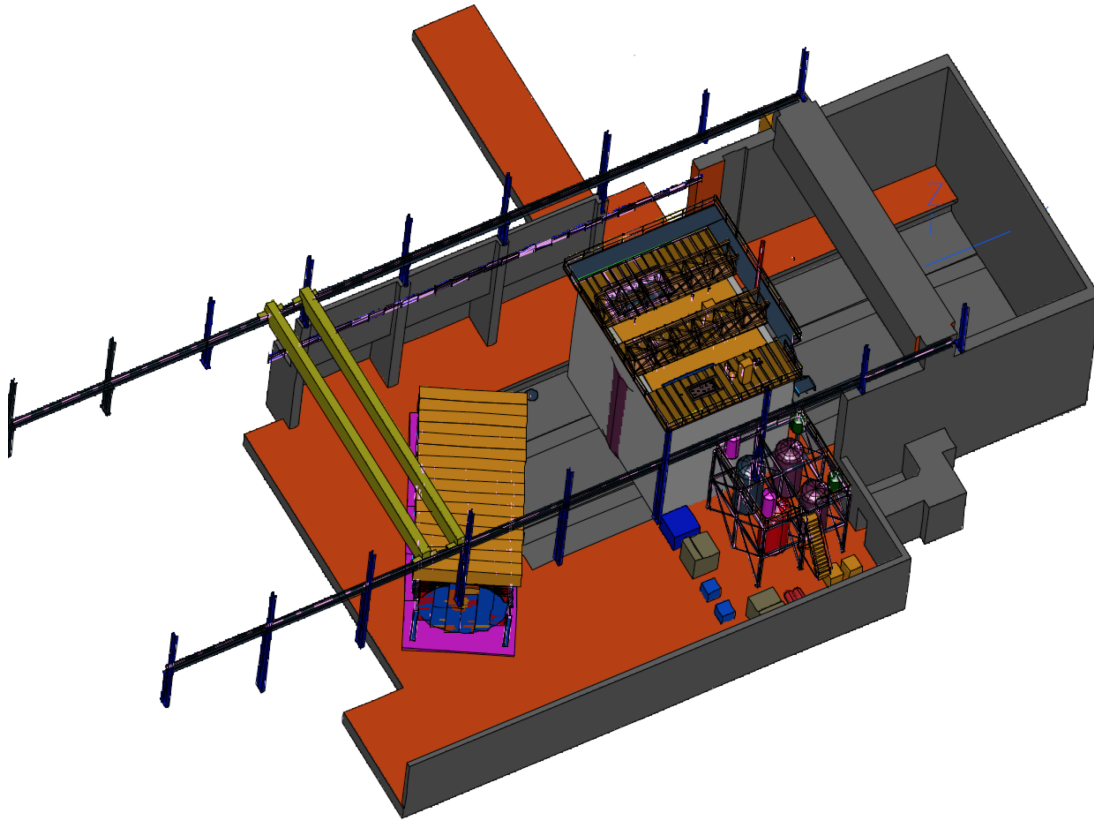
Figure 76. Schematic of far detector hall (DAB) showing SuperBIND and demonstrating that there is room to add another detector (a conceptualized kT-scale magnetized LAr detector is shown) at some future date.

IV.   OUTLOOK AND CONCLUSIONS

In this proposal we have presented a compelling case for the nuSTORM facility. As mentioned in the introduction, nuSTORM's motivation rests on three central themes: 1. A search for sterile neutrinos for unprecedented precision, 2. Unique opportunities in ν interaction physics and 3. Presents a powerful technology test bed for muon accelerator physics. With respect to search for sterile neutrinos, nuSTORM present the only facility that can do all of the following:

- Make a direct test of the LSND and MiniBooNE anomalies.

- Provide stringent constraints for both ν_e and ν_μ disappearance to over constrain $3+N$ oscillation models and to test the Gallium and reactor anomalies directly.

- Test the CP- and T-conjugated channels as well, in order to obtain the relevant clues for the underlying physics model, such as CP violation in $3 + 2$ models.

With respect to ν interaction physics, nuSTORM presents the first opportunity to measure both ν_e and ν_μ cross sections at the the 1% level with a ν beam that can be characterized 5 to 10 times more precisely than conventional ν beams.

Lastly, with respect to accelerator R&D, nuSTORM can provide muon beams suitable for the next generation of studies into muon ionization cooling which are so crucial to the viability of any $\mu^+\mu^-$ collider. This can be done simultaneously while carrying out its neutrino physics program.

[1] D. G. Koshkarev (1974), CERN/ISR-DI/74-62.

[2] D. Neuffer, *Design Considerations for a Muon Storage Ring* (1980), Telmark Conference on Neutrino Mass, Barger and Cline eds., Telmark, Wisconsin.

[3] A. Aguilar et al. (LSND) (????).

[4] A. A. Aguilar-Arevalo et al. (MiniBooNE), Phys. Rev. Lett. **98**, 231801 (2007), 0704.1500.

[5] A. Aguilar-Arevalo et al. (MiniBooNE Collaboration), Phys.Rev.Lett. **105**, 181801 (2010), 1007.1150.

[6] T. Mueller, D. Lhuillier, M. Fallot, A. Letourneau, S. Cormon, et al., Phys.Rev. **C83**, 054615 (2011), 1101.2663.

[7] P. Huber, Phys.Rev. **C84**, 024617 (2011), 1106.0687.

[8] G. Mention, M. Fechner, T. Lasserre, T. Mueller, D. Lhuillier, et al., Phys.Rev. **D83**, 073006 (2011), 1101.2755.

[9] P. Anselmann et al. (GALLEX Collaboration.), Phys.Lett. **B342**, 440 (1995).

[10] W. Hampel et al. (GALLEX Collaboration), Phys.Lett. **B420**, 114 (1998).

[11] J. Abdurashitov, V. Gavrin, S. Girin, V. Gorbachev, T. V. Ibragimova, et al., Phys.Rev.Lett. **77**, 4708 (1996).

[12] J. Abdurashitov et al. (SAGE Collaboration), Phys.Rev. **C59**, 2246 (1999), hep-ph/9803418.

[13] J. Abdurashitov, V. Gavrin, S. Girin, V. Gorbachev, P. Gurkina, et al. (SAGE Collaboration), Phys.Rev. **C73**, 045805 (2006), nucl-ex/0512041.

[14] P. Kyberd et al. (nuSTORM Collaboration) (2012), 1206.0294.

[15] D. Adey et al. (nuSTORM Collaboration) (2013), 1308.6822.

[16] D. Adey et al. (nuSTORM Collaboration), Phys.Rev.D (2014), 1402.5250.

[17] W. Winter, Phys.Rev. **D85**, 113005 (2012), 1204.2671.

[18] F. An et al. (DAYA-BAY Collaboration), Phys.Rev.Lett. **108**, 171803 (2012), 1203.1669.

[19] J. Ahn et al. (RENO collaboration), Phys.Rev.Lett. **108**, 191802 (2012), 1204.0626.

[20] Y. Abe et al. (DOUBLE-CHOOZ Collaboration), Phys.Rev.Lett. **108**, 131801 (2012), 1112.6353.

[21] K. Abe et al. (T2K Collaboration), Phys.Rev.Lett. **107**, 041801 (2011), 1106.2822.

[22] P. Adamson et al. (MINOS Collaboration), Phys.Rev.Lett. **107**, 181802 (2011), 1108.0015.

[23] S. Geer, Phys.Rev. **D57**, 6989 (1998), hep-ph/9712290.

[24] S. Choubey et al. (The IDS-NF collaboration) (2011), 1112.2853.

[25] 1219664, *The Fermilab Main Injector Technical Design Handbook* (1994).

[26] 610465, *The NuMI Technical Design Handbook* (2002).

[27] V. Papadimitriou, *Status of the LBNE Neutrino Beamline* (2011), 1112.0720.

[28] Fermilab, *Technical Division MI Lambertson design*, URL http://tdserver1.fnal.gov/AcceleratorSupport/fmi-magnets/ILA.

[29] Fermilab, *Technical Division, MI C Magnet design*, URL http://tdserver1.fnal.gov/AcceleratorSupport/fmi-magnets/ICA.

[30] Fermilab, *EDB Dipole design*, URL {http://tdserver12.fnal.gov/search?SearchableText=351156}.

[31] FNAL, *FNAL FESS MI Radiation Safety Drawing no 9-6-6-7 C-8* (1993).

[32] Fermilab, *NS1Q1 quadrupole design* (1993), URL http://tdserver12.fnal.gov/search?SearchableText=331805.

[33] Fermilab, *B2 Dipole design* (1993), URL http://tdserver12.fnal.gov/search?SearchableText=351417.

[34] J. Kyle, *Private communication*.

[35] D. Cossairt, *Fermilab Radiological Control Manual Chapter 10 Section 3-6 A* (2010).

[36] S. Chouhan et al., IEEE TRANSACTIONS ON APPLIED SUPERCONDUCTIVITY, **21**, 1813 (2011).

[37] P. Wanderer, *Private communication*.

[38] T. Roberts, *G4beamline - A "Swiss Army Knife" for Geant4, optimized for simulating beamline* (2013), Version 2.12.

[39] V. Lebedev, *OptiM - Computer code for linear and non-linear optics calculations* (2007).

[40] S. Lee, *Accelerator Physics* (World Scientific, 2012), 3rd ed.

[41] A. Liu et al. (2013), iPAC proceedings, Shanghai.

[42] L. Søby, *nuSTORM Beam instrumentation* (2013), eDMS document number: 1284677, CERN.

[43] M. Gasior and R. Jones, *The principle and first results of betatron tune measurement by direct diode detection* (2005).

[44] T. Lackowski et al., *nuSTORM Conventional Facilities Project Definition Report* (2013), FESS/Engineering Project No. 6-13-1.